Year : 2022

Development and characterization of a subcortical stroke model in non-human primates

Brändli Aaron

Brändli Aaron, 2022, Development and characterization of a subcortical stroke model in non-human primates

Originally published at : Thesis, University of Lausanne

Posted at the University of Lausanne Open Archive http://serval.unil.ch
Document URN : urn:nbn:ch:serval-BIB_327B65C226D16

UNIL | Université de Lausanne
Faculté de biologie et de médecine

Département des neurosciences cliniques

Development and characterization of a subcortical stroke model in non-human primates

Thèse de doctorat en Neurosciences

présentée à la

Faculté de biologie et de médecine
de l'Université de Lausanne

par

Aaron Brändli

Master ETH Zürich

Jury

Prof. Micah Murray, Président
Prof. Jocelyne Bloch, Directrice de thèse
Prof. Grégoire Courtine, Co-directeur de thèse, EPFL, Lausanne
Prof. Francesco Lacquaniti, Expert
Prof. Friedhelm Hummel, Expert

Thèse n° 329

Lausanne
2022

Programme doctoral interuniversitaire en Neurosciences des Universités de Lausanne et Genève

LEMANIC NEURO SCIENCE DOCTORAL SCHOOL

UNIL | Université de Lausanne

UNIVERSITÉ DE GENÈVE

UNIL | Université de Lausanne

UNIVERSITÉ DE GENÈVE

Programme doctoral interuniversitaire en Neurosciences des Universités de Lausanne et Genève

Imprimatur

Vu le rapport présenté par le jury d'examen, composé de

Président·e	Monsieur	Prof.	Micah Murray
Directeur·trice de thèse	Madame	Prof.	Jocelyne Bloch
Co-directeur·trice de thèse	Monsieur	Prof.	Grégoire Courtine
Expert·e·s	Monsieur	Prof.	Friedhelm Hummel
	Monsieur	Prof.	Francesco Lacquaniti

le Conseil de Faculté autorise l'impression de la thèse de

Monsieur Aaron Brändli

Master's Degree In Biology With A Major In Neurosciences ETHZ, Zürich

intitulée

Development and characterization of a subcortical stroke model in non-human primates

Lausanne, le 16 mai 2022

pour Le Doyen
de la Faculté de Biologie et de Médecine

Prof. Micah Murray

We are stuck with technology
when what we really want is just stuff that works.

- Douglas Adams

Acknowledgements

I would like to express my deepest gratitude to Professor Jocelyne Bloch and Professor Grégoire Courtine, for offering me the opportunity to pursue my PhD thesis as a part of the .NeuroRestore family, for their guidance and support throughout the challenging periods of this project, as well as the most exciting meals Beijing can offer. I would further like to sincerely thank Professor Elvira Pirondini for her inspiring mentorship, harsh spoken truths, and the endless hours spent looking at monkeys.

A special thanks goes out to the rest of the Stroke-team: Diana Muscalu, Fanny Demon, and Dr. Shiqi Sun. They made this project awesome!

Of course, the rest of the Fribourg family deserves a special kind of recognition as well. They made this place an oasis of scientific knowledge and, most importantly, fun. I therefore extend my thanks to: Dr. Simon Borgognon, Alexandra Hickey, Dr. Marion Badi, Nicolò Macellari, Ilaria Scarpato, Dr. Sara Conti, Dr. Beatrice Barra, Prof. Ismael Seàñez, and Prof. Marco Capogrosso.

I further want to thank the numerous people I had the pleasure of collaborating with in Geneva and Beijing.

I would especially like to thank my family, for their unconditional love, their infinite wisdom and support during the best and worst times, as well as all the idyllic times we got to spend together.

I am grateful for all the time I had with my diverse bunch of friends: Karl & Selina, Toni & Joe, Nici & Eva, Pius & Kerrin, Ruben & Anna, Dave, and Eva.

In the end I would like to thank my fiancée, my love, my best friend, my fiercest supporter, Anni. I thank you for all you have done for me, the time we had together, and the time we will have. I'm so looking forward to see what the future has in store for us.

Fribourg, 21. Februar 2022

Abstract

Each year, millions of people suffer from stroke. The majority of the survivors will suffer form a profound motor deficit, severely debilitating their quality of life. Despite extensive rehabilitative training, these impairments persist for the rest of their lives. There have been advances in the understanding of the fundamental processes underlying the recovery mechanisms. However, a great uncertainty regarding the causes behind the large inter-individual variability seen in the recovery process still remains. Knowledge on these processes might prove pivotal in advancing personalized treatment and precision medicine, in the treatment of stroke patients.

In this work, in order to inform the development of future treatment options, an MRI guided model of sub-cortical stroke in non-human primates (NHP) was developed. A unilateral thermo-coagulation lesion targeting the descending motor fibers at the level of the internal capsule was devised to specifically impair the upper limb. The resulting behavioral impairment was described using a large assortment of reach- and grasp-tasks before and after lesion, and was put into contrast with the loss of fiber density in the cortico-spinal tracts (CST) of the primary motor cortex (M1), as well as the ventral (PMv) and dorsal (PMd) pre-motor cortices.

The lesion model proved to be reproducible and controllable, and aligned with the clinical symptoms seen in stroke patients. Animals with mild impairment showed a functional recovery within the first month, regaining dexterous movement control. Animals with a moderate impairment regained general grasping control, but the ability of dexterous grasping never returned. However, in both cases the underlying grasping strategies were found to be significantly altered. Severely impaired animals never regained the control necessary to perform reaching movements, but interestingly, the emergence of aberrant flexor-synergy, typical of severe stroke patients, was observed. The emergence of flexor synergy symptoms has not previously been reported in NHP models.

In order to quantify inter-individual variances in lesion location and CST composition, the resulting histological preparations were registered into the standard MNI MRI atlas for *M. fascicularis*, providing a robust platform for further multimodal analysis in a unified space. A histological analysis of the underlying loss in fiber density in the CST and spinal terminations

confirmed the importance of M1 in determining the chronic impairment severity, with PMv and PMd playing a reduced but important role in recovery.

From this study, the dominant role of the CST and, in particular M1 projections, becomes evident. With the novel model of sub-cortical stroke in NHPs, a platform for the investigation of the mechanistic interactions of the remaining tracts was proposed, laying solid groundwork to aid in the development of effective therapies supporting stroke patients in the recovery of their independence.

Résumé

Chaque année, des millions de personnes sont victimes d'un accident vasculaire cérébral. Dans de nombreux cas, les personnes touchées souffrent d'un profond déficit moteur, ce qui nuit gravement à leur qualité de vie. Malgré une rééducation intensive, ces déficiences persistent pour le reste de leur vie. Des progrès ont été réalisés dans la compréhension des processus fondamentaux qui sous-tendent les mécanismes de récupération, mais une grande incertitude persiste quant aux causes de la grande variabilité interindividuelle observée dans la qualité de la récupération des personnes atteintes. La connaissance de ces processus pourrait s'avérer essentielle pour faire progresser le traitement personnalisé et l'évolution vers une médecine de précision, dans le traitement des patients victimes d'un AVC.

Afin d'éclairer le développement de futures options thérapeutiques, un modèle d'AVC sous-cortical guidé par IRM a été développé chez des primates non humains (PNH). Une lésion unilatérale par thermo-coagulation ciblant les fibres motrices descendantes au niveau de la capsule interne a été conçue, afin d'altérer spécifiquement le membre supérieur. L'altération comportementale qui en résulte a été décrite à l'aide d'une large batterie de tâches d'atteinte et de saisie avant et après la lésion, et a été mise en contraste avec la perte de densité des fibres dans les tractus cortico-spinales (TCS) du cortex moteur primaire (M1), ainsi que dans les cortex pré-moteurs ventral (PMv) et dorsal (PMd).

Le modèle de lésion s'est avéré reproductible et contrôlable, et correspond aux symptômes cliniques observés chez les patients victimes d'un AVC. Les animaux présentant une déficience légère ont montré une récupération fonctionnelle au cours du premier mois, retrouvant le contrôle des mouvements dextres. Les animaux souffrant d'une déficience modérée ont retrouvé un contrôle général de la préhension. Cependant, les déficits de la dextéritié manuelle fine persistent. Les stratégies de préhension sous-jacentes se sont avérées considérablement modifiées. Les animaux gravement atteints n'ont jamais retrouvé le contrôle des mouvements d'éxtension, mais il est intéressant de noter l'émergence de schémas de mouvements semblables à ceux de la synergie des fléchisseurs, ce qui n'avait pas été signalé auparavant dans les modèles de PNH.

Afin de quantifier les variances interindividuelles dans la localisation des

lésions et la composition du TCS, les préparations histologiques résultantes ont été enregistrées dans l'atlas IRM standard MNI pour *M. fascicularis*, fournissant une plateforme robuste pour une analyse multimodale ultérieure dans un espace unifié. Une analyse histologique de la perte de densité des fibres dans le TCS et les terminaisons spinales confirme l'importance de M1 dans la détermination de la gravité de la déficience chronique, les PMv et PMd jouant un rôle réduit mais important dans la récupération.

Cette étude met en évidence le rôle dominant du TCS, et en particulier des projections de M1. Grâce à ce nouveau modèle d'accident vasculaire cérébral sous-cortical chez le PNH, des mécanismes neuronaux sous-jacents à la récupération fonctionelle ont été proposés; posant ainsides bases solides pour aider au développement de thérapies efficaces permettant aux patients victimes d'un accident vasculaire cérébral de retrouver leur indépendance.

Contents

List of Figures

List of Tables

Chapter 1

Introduction

Every other second another person suffers from a stroke, throwing their and the lives of those closest to them into disarray. While many stroke victims will unfortunately no longer be able to perform simple tasks in their daily schedules, a third will not survive the first year following the incident (Johnson et al., 2019; Wafa et al., 2020). For those who do survive, often a life long battle with the diverse range of symptoms begins, taking a huge toll on them and their family.

Many stroke patients will suffer from paresis or paralysis, and will enter rehabilitative treatment to restore motor function, as soon as possible, after the stroke in an effort to exploit the phase of plasticity (Burton, 2000; Hankey et al., 2007). After an insult to the central nervous system, the otherwise very change-averse neural tissue is thought to be more pliable and thus more receptive to changes induced by rehabilitative learning and restoration tasks. This phase lasts for only a few weeks after the insult; the largest recovery in motor function can be achieved during this time period (Burton, 2000; Hankey et al., 2007; Krakauer and Carmichael, 2017). Despite great efforts made to restore as much function as possible during this time, often only a meager restoration of the patients' motor abilities is seen. Furthermore, the retention of trained techniques and their application to the activities of daily life is largely absent (Schaefer et al., 2013; Winstein and Kay, 2015). It has been proposed that this lack of success

in devising adequate recovery paradigms stems primarily from two causes: a fundamental lack of understanding of the underlying processes governing loss of function and, especially, its restoration, as well as insufficient measuring and quantification tools to quantify the progress and success of rehabilitative interventions (Winstein and Kay, 2015; Santisteban et al., 2016; Krakauer and Carmichael, 2017).

In recent years, progress has been made in the dissection of true recovery processes and their masking by compensatory mechanisms. However, these findings are only just being slowly absorbed into the clinical realm of rehabilitative practice (Santisteban et al., 2016; Krakauer and Carmichael, 2017). On the other hand, insights into the mechanistic processes governing the ability of patients to permanently and efficiently re-attain adequate motor control have been made in recent years (Kaeser et al., 2011; Nishimura et al., 2013; Wahl et al., 2014; Wahl and Schwab, 2014; Li et al., 2015). Nevertheless there remains a clear gap between this fundamental research and clinical application. As non-human primates share advanced sensorimotor attributes with humans, they can provide the platform for clinically relevant investigations (Badi et al., 2021). Thus, research in non-human primate models might lead to crucial insight on the mechanisms underlying recovery of stroke, and would possibly open the door for interventions prolonging or even re-initiating the sensitive period of recovery using pharmacologic or prosthetic interventions. However, to achieve this goal, a robust base for such research must be established. Animal models that produce clinically relevant and translatable deficits, which are also repeatable and provide the ability to be tailored to the research question at hand must be devised (Cook and Tymianski, 2012; Grefkes and Ward, 2014; Higo, 2021).

1.1 The motor system of upper-limb control

Life is centrally defined by its ability to move and interfere with its surroundings. For human beings, muscular movement is the main method in which we interact and communicate with the world, be this via walking, using a computer, or simply talking with a friend. All voluntary control of these actions is ultimately directed by our central computing unit, the central nervous system: the brain and spinal cord. A general understanding of the function and dysfunction of this system is therefore instrumental for the development of future interventions. The following paragraphs will thus give a brief overview of the brain regions and their mode of action, eventually focusing on upper-limb control.

1.1.1 Brain

Motor cortices

The first description of a motor area, inducing movement after being stimulated was put forth by Fritsch and Hitzig (1870, 2009) after they electrically stimulated the cerebral cortex with an insulated electrode. They noted that only very limited amounts of electricity could evoke strong motor responses, previously believed to be impossible. Jackson (1873), observed the cortical control of limbs to be orchestrated by cerebral regions contralateral to the controlled muscles by analysis of epileptic patients, which was confirmed shortly after in non-human primates (NHPs) by Ferrier and Burdon-Sanderson (1874). Only 30 years later, a somatotopic map of the area, today known as the motor cortex, was described by Grünbaum and Sherrington (1904). (For a recent in-depth review see: Bennett and Hacker (2002))

Elucidating the function and interaction of the areas collectively known as the premotor cortex took another century. He et al. (1993) found that the premotor cortex, previously thought of as a monolithic structure, had multiple anatomically and connectively distinct regions. This finding was further refined by Rizzolatti et al. (1998), defining seven independent motor areas: F1-F7. Whereas F1 corresponds to Brodmann area (BA) 4, the other 6 regions split Brodmann area 6 into conceptually distinct regions (Rizzolatti et al., 1998). The premotor areas were further distinguished into two types: fronto-dependant and parieto-dependant. The fronto-dependant regions, F6 and F7, receive abundant input from the frontal lobe and project to the rest of the motor cortex and brain stem. F2 to F5, on the other hand, are strongly innervated by sensory areas and primarily project to

F1 and the spinal cord. The motor areas of the NHP cortex are thus defined as the following regions:(1) M1/F1/BA4: the primary motor cortex (2) F2 and F7: the parieto- and fronto-dependent sections of the dorsal premotor cortex (PMd) (3) F3 and F6: the parieto- and fronto-dependent parts of the supplementary motor area (SMA), also known as pre-SMA and SMA-proper (4) F4 and F5: the caudal and rostral portions of the ventral premotor cortex (PMv) (Rizzolatti et al., 1998; Rizzolatti and Luppino, 2001a,b; Caminiti et al., 2017) (Figure 1.1)

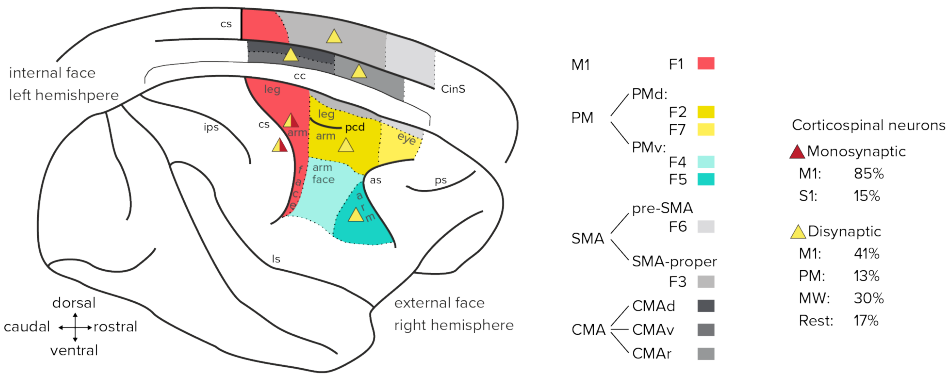

Figure 1.1: Motor cortex and corticospinal neurons in non-human primates The motor cortical structures in the macaque brain are located in between the central sulcus (cs) and arcuate sulcus (as). The traditional four motor areas are depicted in color: primary motor cortex (M1, red), premotor cortex (PMv, teal; PMd, yellow), supplementary motor area (SMA, light-gray), and cingulate motor area (CMA, dark-gray). These areas are then further subdivided into their functional constituents. The areas with a substantial monosynaptic (red) or disynaptic (yellow) contribution to the corticospinal tract are labeled with triangles, and their respective neuron density broken down to the right. The disynaptic contribution of SMA and CMA are summarized as the contribution of the medial wall (MW). Further sulci and structures are denoted as: cc - corpus callosum; CinS - cingulate sulcus; ips - intraparietal sulcus; ls - lateral sulcus; pcd - precentral dimple; ps - principal sulcus. Modified from (Rizzolatti et al., 1998; Strick et al., 2021; Borgognon, 2020)

Cortical Motor control

Primary motor cortex The primary motor cortex (M1) is seen as the center of motor control. It receives a vast amount of input from both adjacent and more distant cortical structures, with the pre-motor areas providing inputs regulating the planning and timing of adequate muscle contractions, and sensory areas providing input of the bodies' current position, as well as the state of its surrounding environment. As the large integrator of motor commands, it boasts a rich array of cortico-cortical and cortico-fugal tracts.

With its cortico-cortical connections M1 provides the basis of coordination of movements, posture control as well as the efference copy (Rizzolatti and Luppino, 2001a). On the other hand, the cortico-fugal projections allow the direct transmission of motor commands through the spinal cord (Kuypers, 2011). Recent studies have revealed that these corticospinal connections are made up of two types: di-synaptic as well as mono-synaptic or cortico-motorneuronal (CM) projections. Whereas, the di-synaptic projections are found in all vertebrates, their CM counterpart is only present in some dexterous primates, such as humans and macaques. This finding has prompted the division of M1 into the 'new M1' and 'old M1'. Being the nearly sole origin of CM connections, the new M1 is situated in the caudal area of M1, in the anterior bank of the central sulcus (Rathelot and Strick, 2009; Witham et al., 2016).

Due to the vast amount of large descending fibers originating from M1, as well as the ease of evoking muscle contractions by electrical stimulation, M1 has long been seen as the sole provider of the brain's motor output. In recent years, however, it has become clearer that M1 is not the sole origin of corticospinal connections. In fact, the projections of M1 make up only 40% of the descending projections, with the premotor cortex (10%), supplementary (20%) and cingulate (20%) motor areas providing the rest of the motor-spinal connections (Strick et al., 2021).

Dorsal premotor cortex The dorsal premotor cortex (PMd) is associated with the planning of general limb trajectories and integrating somatosensory and visual information from the parietal lobes. F2, especially, has rich connections to the primary motor cortex and directly connects to the spinal cord. Whereas the dorsal section informs lower limb trajectory, the ventral section is responsible for upper-limb movements (Rizzolatti and Luppino, 2001b; Caminiti et al., 2017; Gamberini et al., 2020).

Ventral premotor cortex The F4 and F5 regions are strongly associated with the planning and execution of goal directed actions of the upper-limb, especially the hand. The areas receive their input from the visual stream, the surrounding motor areas, as well as the pre-frontal cortices (Rizzolatti and Luppino, 2001b; Caminiti et al., 2017). The areas are further home to a mirror neuron population, associated with visual and somatosensory learning and interpretation (Linkovski et al., 2017). The PMv is thus thought to instruct M1 on how and when an object should be grasped, and directly interface with the spinal cord.

For an in-depth revision refer to: (Lawrence and Kuypers, 1968; Brinkman, 1981; Matelli et al., 1985; Wiesendanger et al., 1987; Dum and Strick, 1991; Luppino et al., 1993; Rizzolatti et al., 1998; Rizzolatti and Luppino, 2001a,b; Dum and Strick, 2002; Lemon, 2008; Linkovski et al., 2017; Caminiti et al., 2017)

Primary somatosensory cortex

Caudal to the central sulcus and the motor cortices, lies the primary somatosensory cortex (S1). In a 1970 elecrophysiological study, S1 was shown to respond to tactile stimuli of specific regions in NHPs, paving the way for today's understanding of the somatosensory organization (Whitsel et al., 1969). This and similar studies (in combination with cytoanatomical and tracing studies) eventually gave rise to the somatosensory homunculus. The homunculus describes the mapping of somatosensory receptors along the body surface to a deformed, but relatively consistent, image on the brain's surface, with multiple sensory modalities forming their own homunculus (Nelson et al., 1980; Pons et al., 1985; Krubitzer et al., 2004). S1 can thus be divided into four anatomically and connectively distinct regions described by Brodmann: 3a, 3b, area 1 and area 2.

In recent years, S1 has been found to not only receive and integrate sensory information and relay it to other cortical structures, but also to have monosynaptic connections to the spinal cord; the cortico-motorneuronal neurons found in area 3a are thought to be involved in direct motor control (Baldwin et al., 2018). These connections will be further discussed in subsequent sections.

1.1.2 Corticospinal tract and Cortico-motorneuronal projections

The corticospinal tract (CST) provides the most direct control of muscle activity. Neurons in the CST originate in cortical areas, and directly connect to their appropriate spinal cord levels. Before entering the spinal cord, neurons of the CST coalesce in the internal capsule, retaining some of their somatotopic organization but overlapping partially (Morecraft et al., 2002). The descending motor tracts of the motorcortices pass through the posterior arm of the internal capsule, with the pre-motor areas running closer to the internal capsule's genu (Figure 1.2). The descending tracts of the motor areas eventually fully overlap at the cerebral peduncle (Morecraft et al., 2007). At the spinal level, the CST descends through the lateral

white matter, with most of its projections projecting contra-lateral to their respective brain region (Figure 1.3). Upon reaching their destination, they largely form connections in the spinal lamina VII, as well as laminas VI and IX, to a lesser extent (Morecraft et al., 2013, 2002).

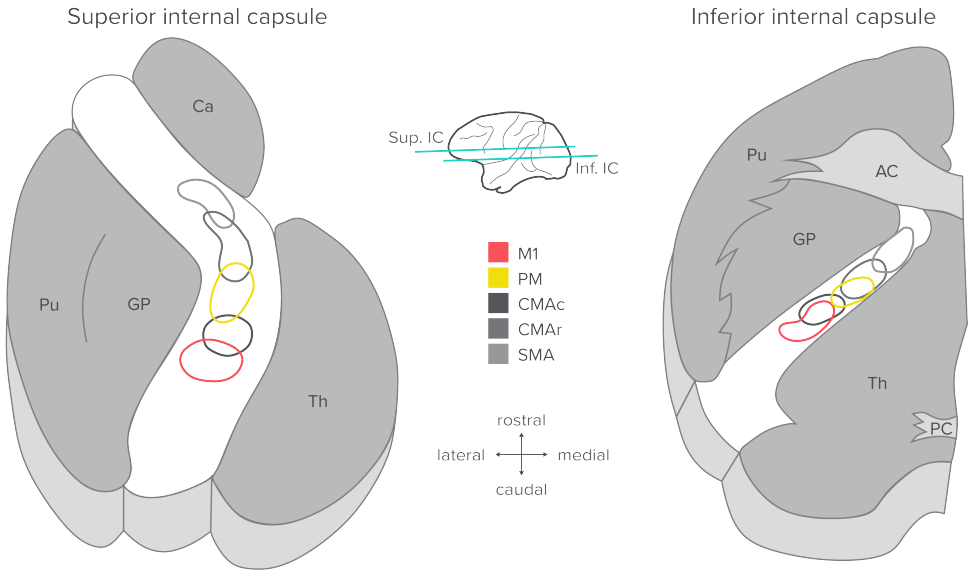

Figure 1.2: Corticospinal tract in the internal capsule The internal capsule (white) is depicted at two depths: superior (left) and inferior (right). The corticospinal tract origins from five motor areas are depicted with their extent and location encircled: primary motor cortex (M1, red), premotor cortex (PM, yellow), caudal cingulate motor area (CMAc, dark-gray), rostral cingulate motor area (CMAr, gray), and supplementary motor area (SMA, light-gray). The surrounding structures are denoted: AC - anterior commissure; PC - posterior commissure; Ca - Caudate; GP - globus pallidus; Pu - putamen; Th - thalamus. Modified from (Morecraft et al., 2002)

In dexterous primates, we can distinguish between two types of corticospinal projections: indirect and direct cortico-motorneural (CM) projections (Lemon, 2019). While the indirect pathway terminates in the interneuronal laminas, especially lamina VII (59%), CM projections directly innervate alpha motorneurons in lamina IX (18%) (Morecraft et al., 2013). CM neurons have been shown to almost exclusively originate from the 'new M1' and area 3a of S1 (Rathelot and Strick, 2006, 2009; Witham et al., 2016). The function of these projections is more thoroughly discussed in chapter 1.1.3

1.1.3 Manual Dexterity and upper-limb movement

Our hands are the most versatile instruments we possess to interact with our environment. They enable us to accomplish feats ranging from simply opening a door, to micro-surgical interventions, and everything in between. This dexterous prowess, seen also in new world primates, originates from the capacity for digit individuation and a generally enhanced level of control (Strick et al., 2021; Lemon, 2019). While we have a fairly good understanding of their mechanical function, we are sorely lacking insight into their neuronal control.

In new world primates, the areas controlling and sensing hand movement and positioning occupy an enormous amount of cortical surface area (Strick et al., 2021). However, the enlarged representation of the upper-limb in cortical area does not account for the vastly more articulated hand control. Two further mechanisms seem to help set primate dexterity apart from other species: (1) The cortico-motorneural (CM) system and (2) a majorly rearranged cortical connectivity and control mechanism.

The CM system provides a direct, mono-synaptic pathway from the cortex to motor neurons in the spinal cord. Such a system is absent in non-primate species, and has only been found in neonatal mice (Gu et al., 2017). It has thus been a major field of interest in understanding human and primate grasping. At a first glance, a mono-synaptic system would bring one major advantage: speed. One could therefore surmise that this pathway is used to specifically control precise movements of single muscles. However, the opposite seems to be the case. CM neurons show significant overlap in both somatotopic cortical organization, as well as in the muscles they activate. Single CM neurons tend to interface multiple muscles, forming synergistic patterns. CM fibers predominantly originate in the 'new M1' (Rathelot and Strick, 2009), with a smaller but substantial portion found in area 3a of S1. Somewhat atypical for the motor system in primates, CM somatotopy of the upper-limb shows large overlap, leading to some speculation that the main function of CM cells is one of fine-tuned pattern generation, bypassing the systems of the spinal cord (Figure 1.3).

While other species (e.g. rodents) tend to have large overlaps in somatotopic arrangement of their fore- and hind-limb projections, primates show very clearly distinct cortical regions. Additionally, they have expanded their motor control to 6 anatomically and connectively distinct regions, each with their own somatotopic map. All these areas have direct access to the spinal cord circuits, leading to a parallel control structure, as opposed to a mostly serial approach. How these descending tracts are divided with

regards to movement control is still largely unexplored, in part due to the large discrepancies in axonal diameters. The effects of electrical stimulation used in assessing these tracts, predominantly activated thick axons, mostly originating in M1, masking the stimulation effects on thinner fibers, making their investigation a challenge. The collaborative control in the intact state is still quite enigmatic. Even more so is the method via which the fibers of these regions interact and possibly redirect control to spared descending tracts in a lesioned state.

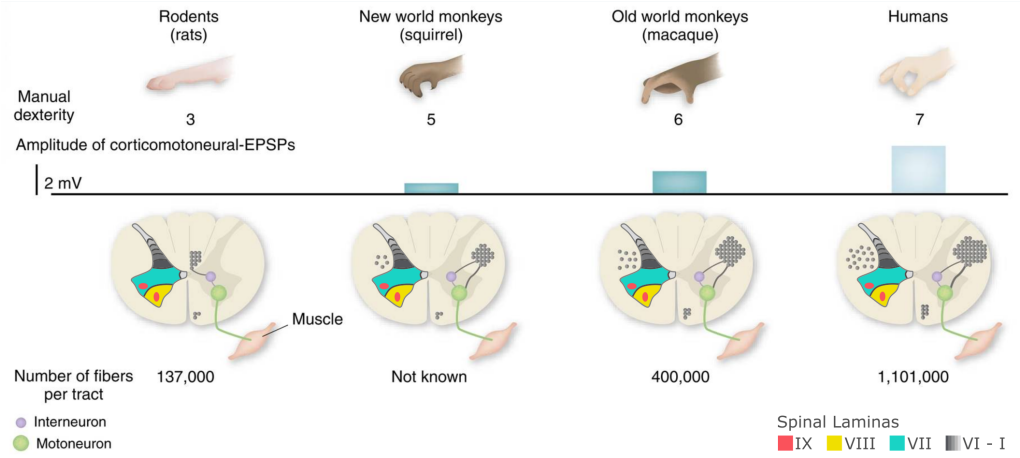

Figure 1.3: Emergence of manual dexterity across species Depiction of the manual dexterity across species and their connective correlates of the corticospinal tract. In the primate species, direct cortico-motorneuronal connections innervate the ventral horn (Lamina IX), a circuit that is absent in rodents and other species. The presence of mono-synaptic connections, as well as the vastly increased corticospinal tract density, allows primates to perform highly specific grasping motions, such as the finger-thumb opposition precision grip. Modified from (Courtine et al., 2007)

1.2 Stroke

Each year, stroke leaves millions of patients and their loved ones devastated. Globally, one quarter of adults will have a stroke during their life-time (Feigin et al., 2018). In the European Union alone, about ten million people are affected by stroke, with a yearly incidence rate of more than one million (Johnson et al., 2019; Wafa et al., 2020). As such, stroke is one of the leading causes of lasting disability and mortality in adults (Figure 1.4). Victims of stroke may suffer from a wide array of deficits in muscle control, speech production and perception, as well as mental health (Gresham et al., 1997; Williams et al., 2004). Even after therapeutic interventions, patients will often suffer from their symptoms for the rest of their lives.

1.2.1 Burden

Stroke victims suffer from diverse deficits, with motor (80-85%) and somatosensory (40-50%) deficits being the most prevalent. One in four patients shows deficits in language, vision, attention, and memory (Nys et al., 2007; Ringman et al., 2004; Appelros et al., 2002; Rathore et al., 2002; Buxbaum et al., 2004; Ramsey et al., 2017). Many patients suffer from multiple symptoms, depending on the location and size of the stroke lesion. Besides these primary deficits, a third suffer further from post-stroke depression, or other mental illnesses (Williams et al., 2004). The complexity of these syndromes requires treatment and support that is highly specific to the individual.

Besides the personal trauma stroke victims suffer, this disease poses an enormous burden on the global health care system. Direct costs of stroke treatment in Europe amount to over €27 billion yearly. Associated costs, such as a loss of productivity and informal care, are estimated to more than double the posed economic burden (Luengo-Fernandez et al., 2020; Olesen et al., 2012). As stroke mainly effects older patients, the world's aging population will further compound the care-giving and financial challenges. Over the coming 30 years, a 27% increase in stroke incidents is expected (Donnan et al., 2008; Wafa et al., 2020).

1.2.2 Emergence

A stroke is a cardiovascular incidence, leading to an acute reduction of blood flow. The lack of blood circulation leads to a steep drop in oxygen and glucose concentration causing the affected tissue to weaken and die off within mere minutes. There are two main categories of strokes: ischemic

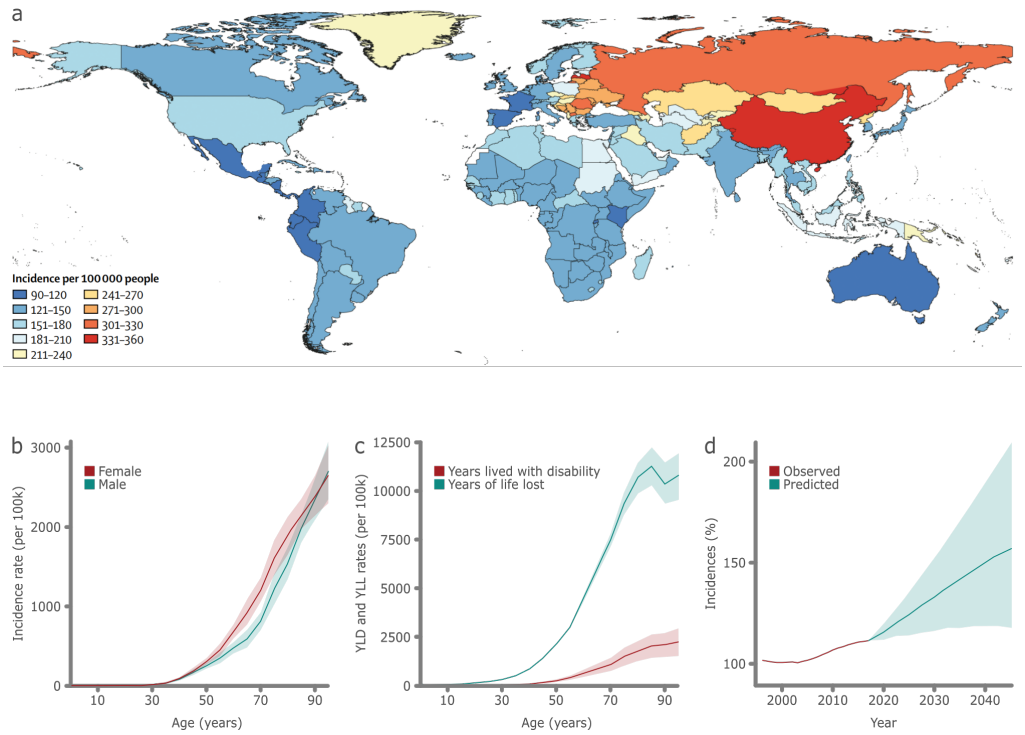

Figure 1.4: Burden of Stroke (a-c) Depiction of an overview of the stroke prevalence and impact on patients world wide in the year 2016. (a) World wide distribution of stroke incidences. (b) The incidence rate per 100000 people of stroke by age and sex. (c) Estimation of both years of life lost due to an early death (YLL), as well as the years lived with a disability (YLD) due to stroke. (d) Expected incidences of stroke in Europe, as compared to the baseline of the year 2000. The solid line depicts the expected incidences with no change in the incidence rate. The shading encompasses a change in incidence rate with $\Delta 1\%/year$. Figure adapted from Johnson et al. (2019) and Wafa et al. (2020).

and hemorrhagic stroke (Sudlow and Warlow, 1997; Meyer et al., 2009). The incidence rate of the two is starkly contrasted, with the likelihood of an ischemic stroke being five to ten times higher. On the other hand, hemorrhagic strokes are generally associated with a higher mortality and severity (Andersen et al., 2009).

Strokes of an ischemic nature are the result of an arterial or venous occlusion. Such occlusions stem either from locally accumulating plaques (thrombi) or stray particles in the blood flow (emboli) that gets wedged in the intracranial vasculature. Embolic strokes are of a more sudden nature. The dislodged particles often disrupt larger vessels causing the disruption of arterial blood flow in large areas. Thrombi on the other hand, mostly form in the low pressure environment of veins or smaller arteries. Initially not causing any overt symptoms, thrombi slowly occlude the circulation of

surrounding tissues, and are often the cause of subcortical strokes.

Hemorrhagic strokes occur when the intracranial vasculature ruptures, causing blood to rush into the extracellular space and severely deplete circulation volume in the region. Hemorrhagic strokes often cause very severe strokes and have a fourfold acute mortality rate, as compared to ischemic strokes. This discrepancy is due to a generally larger size of the infarct zone, as well as the absence of possible re-perfusion (Petty et al., 1999, 2000; Kolominsky-Rabas et al., 2001; Andersen et al., 2009).

The core of an acute ischemic stroke lesion is surrounded by tissue referred to as the penumbra (Rossini et al., 2003; Furlan et al., 1996). The penumbra consists of neuronal tissue that is severely weakened from the lack of blood flow, but is still alive. Besides live-maintaining care, maximizing the amount of rescued tissue is the highest priority in acute care of stroke patients.

Due to the heterogeneous nature of stroke, its risk factors are likewise varied and complex. There are four 'non-modifiable' risk factors: age, sex, ethnicity and genetics (Boehme et al., 2017). Stroke risk is primarily correlated with aging, with its incident rate doubling for every 20 years of age past age 40 (Virani et al., 2021). As for the modifiable risk-factors, the most impactful contributors to stroke are hypertension, diabetes mellitus, hyperlipidemia, smoking as well as metabolic syndrome (Boehme et al., 2017).

1.2.3 Current treatment

The most effective approach to stroke treatment is prevention. Many of the risk-factors of stroke can be reduced by leading a generally 'healthy' lifestyle, promoting a healthy diet, physical activity, cessation of smoking, and weight control (Boehme et al., 2017). Additional measures might involve administration of anti-hypertensives, anti-coagulants, and cholesterol-reducing drugs (Amarenco and Labreuche, 2009; Blackwell et al., 2009; Chen and Yang, 2013).

When a stroke occurs, the distinction between ischemic and hemorrhagic stroke is of the utmost importance, as, apart from life-sustaining treatments, they require opposing care regimes. While some clinical signs can help distinguish the two sub-types, neuroimaging (e.g. computer tomography) is needed for a definitive diagnosis (Yew and Cheng, 2015; Ojaghihaghighi et al., 2017). In the case of an ischemic stroke, reperfusion has absolute priority. The current gold standard treatment is an intra-venous administration of alteplase, a thrombolytic substance. In some cases, a mechanical

thrombectomy can be performed to restore blood-flow (Powers et al., 2019). In the case of a hemorrhagic stroke, treatment revolves around containing the extent of the hemorrhage and preventing secondary bleeding. In the case of patients taking blood thinners, their effect is reversed. Blood pressure management and possible surgical interventions to contain further bleeding are part of the recommended treatment (Hemphill et al., 2015). However, the best treatment approaches for hemorrhagic strokes are far less explored than its ischemic counterpart.

In both cases, starting rehabilitative care within the first few weeks after the incident has been shown to be beneficial to long-term recovery (Kwakkel et al., 2004; Buma et al., 2013; Winstein et al., 2016). This is corroborated by many animal models, showing that high dose rehabilitation during an early time window, yields the biggest improvement in functional motor tasks (Murphy and Corbett, 2009; Zeiler and Krakauer, 2013; Wahl and Schwab, 2014). To enlarge the rehabilitative effect, the patients' tasks should be challenging, goal-driven, and functional tasks, as opposed to earlier attempts of highly repetitive tasks (Plautz et al., 2000). (Figure 1.5)

Despite these rehabilitative measures improving the patients' motor function in clinical settings, they are often still not able to perform simple tasks during their daily activities (Di Pino et al., 2014; Krakauer and Carmichael, 2017). This can be partially attributed to ineffectiveness and inefficiency of the routinely applied rehabilitation measures, but is probably largely due to a lack of understanding of the underlying repair mechanisms (Krakauer and Carmichael, 2017).

1.2.4 Proposed recovery mechanisms for upper-limb function

After a stroke, 80% of patients suffer from a loss of muscle control (Gresham et al., 1997; Langhorne et al., 2009). In all but the most severe cases, motor function spontaneously recovers in a logarithmic fashion over the first 3 to 6 months (Kwakkel et al., 2006). In many cases, the control of the lower limbs returns to a level of daily usability during the initial recovery window. Unfortunately, the upper-limb often regenerates only marginally, forcing the patients to adopt compensation mechanisms, or seek help from peers to function in daily life (Kwakkel et al., 2006; Buma et al., 2013; Krakauer and Carmichael, 2017). Improvements of the upper-limb control are greatest in the first few weeks after the incident and are only marginal thereafter, hinting at a critical time window for recovery (Kwakkel et al., 2004; Murphy and Corbett, 2009; Zeiler and Krakauer, 2013). The extent of recovery

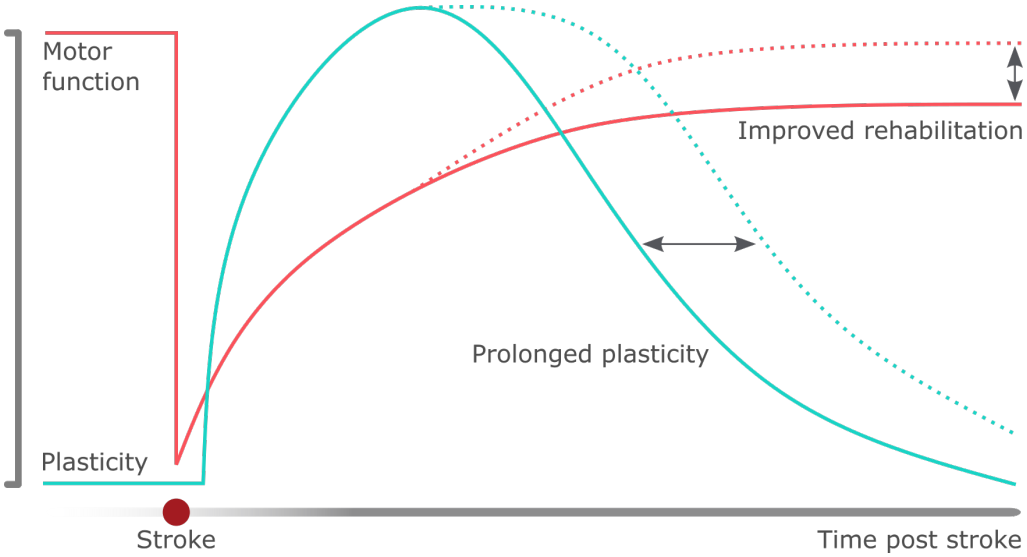

Figure 1.5: Enhancing functional recovery post stroke Stroke patients often suffer from an acute decline in motor function. In the weeks following the incident spontaneous recovery of the lost function takes place in a logarithmic fashion, often plateauing well below the original abilities (red line). This recovery is made possible by the steep incline of plasticity following CNS injury (cyan line). Rehabilitative therapies are focusing on exploiting intensive training during the plastic phase in order to increase the potential enhance motor outcomes (red dashes). Future interventions might achieve the prolongation or re-initiation of the sensitive phase of plasticity (cyan dashes), and thus ameliorate the patients ability to perform their daily activities. Figure adapted from Ward et al. (2015).

during the first few months has been shown to be somewhat predictable. Especially retention of residual finger movement has been shown to be a positive predictor of hand recovery (Nijland et al., 2010). Later studies have used neuroimaging techniques to further predict and understand the expected range of recovery outcomes(Stinear et al., 2012; Ramsey et al., 2017). However, the mechanisms of recovery remain elusive. Nevertheless, animal models might shed some light on the neuronal mechanisms underlying spontaneous and assisted recovery.

In smaller cortical lesions it has been shown that areas that are functionally and anatomically close to the lesioned tissue show an increased activity during the recovery phase. Functional mapping studies demonstrated a remapping of the lost connectivity to the surrounding spared tissue (Nudo and Milliken, 1996; Rouiller et al., 1998). Further stimulation of the penumbral area has been shown to promote functional recovery of upper-limb and grasping (Cheng et al., 2014). After focal M1 lesions, somatotopic 'map-expansions' have been reported in the ventral premotor cortex, as well as

in the supplementary motor area (Dancause et al., 2006; Eisner-Janowicz et al., 2008; Dancause and Nudo, 2011). In larger cortical strokes, where similarly functioning motor areas are damaged, the contra-lesional hemisphere seems to play a more pronounced role in the recovery process (Frost et al., 2003; Rehme et al., 2011). In the first weeks of recovery, both hemispheres have been shown to activate during movements with the paretic hand, reverting back to normal activation levels with time (Ward et al., 2003; Tombari et al., 2004). It remains controversial if the increased activation of the contra-lesional hemisphere is indeed promoting recovery or is simply a sign of maladaptive plasticity (Xerri et al., 2014). Nevertheless, as is the case with ipsilesional stimulation, focal stimulation of the contra-lesional M1 has been shown to promote upper-limb recovery (Carmel et al., 2014; Wahl et al., 2017).

The lesion size and location in the cortex largely determine the prospects of recovery in the affected patients. However, there remains a great deal of uncertainty. In the case of subcortical strokes especially, the cortical areas often remain relatively intact. It has been shown that the lesion load to the internal capsule, and therefore the CST, is highly predictive of the regained functional control (Binkofski et al., 1996; Zhu et al., 2010; Schulz et al., 2017b).

As the adult central nervous system is quite adverse to large scale anatomical changes, it has become abundantly clear that there is a narrow time window where neuroplastic recovery can occur (Kwakkel et al., 2004). Beyond this time window, rehabilitative effects stem primarily from compensatory mechanisms (Buma et al., 2013; Krakauer and Carmichael, 2017). This notion of an early plasticity phase has received strong support from various experiments in rodents, showing significantly better outcomes when rats were undergoing forelimb training in the first 28 days after stroke as opposed to later training regimes(Biernaskie, 2004). Further subdividing this early phase into a very early plasticity phase, where either neural growth supporting drugs or optogenetic stimulation was applied, followed by an intense training period further heightened this effect (Wahl et al., 2014, 2017).

Despite the many insights gained from human and animal studies, the best predictor for upper-limb recovery is still the initial severity of motor impairment (Coupar et al., 2012; Ward, 2017). Even with this predictor, there remain two groups in severe cases, one following a proportional recovery as predicted by the initial impairment, and a second group showing little to no recovery. These two groups are nearly equally large, but show no

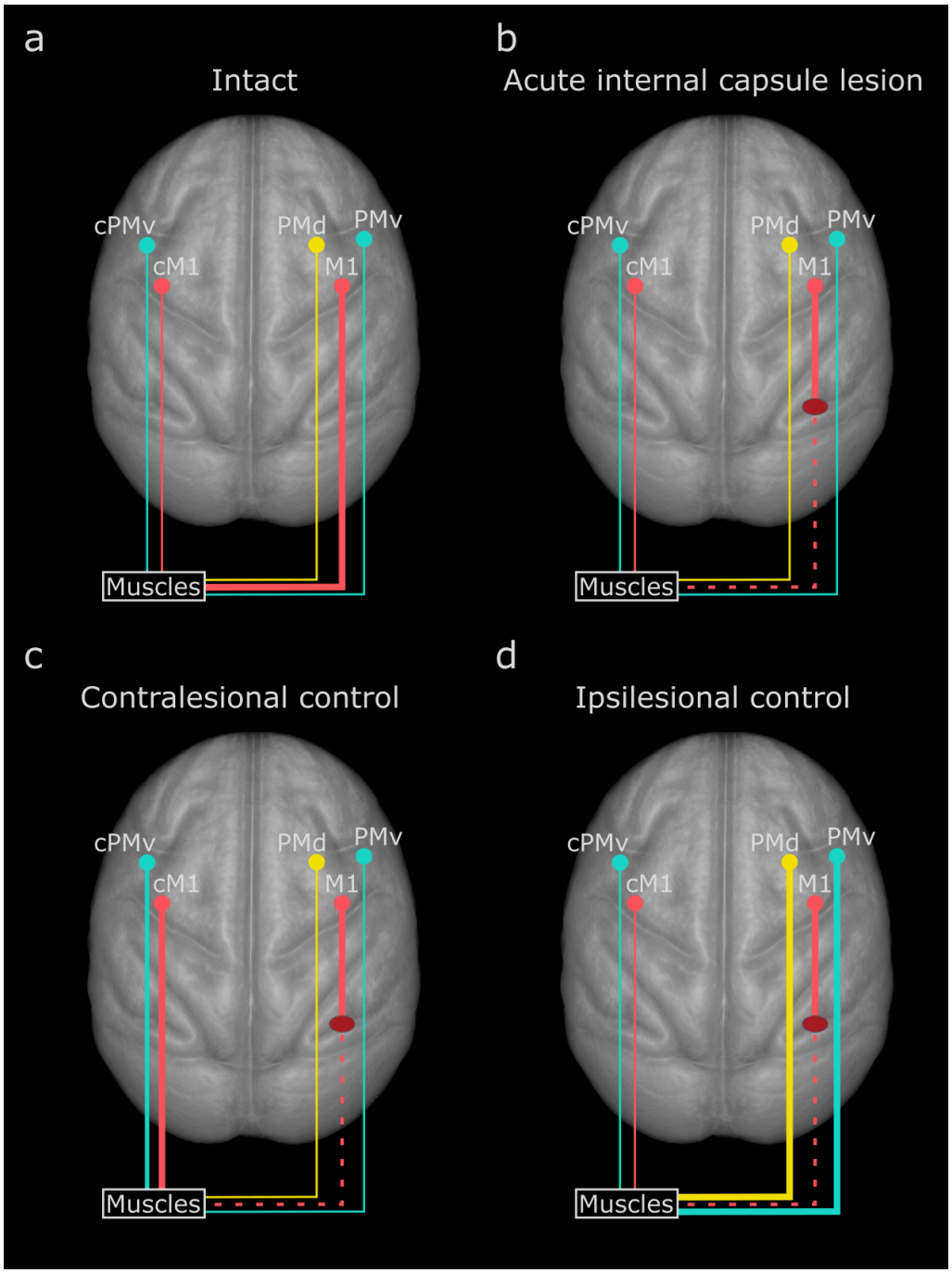

Figure 1.6: Proposed recovery mechanisms after stroke (a-d) Depictions of the main (thick lines) and supporting (thin lines) tracts in various states before and after a focal lesion in a non-human primate, especially focusing on the skeletal muscle control of the upper-limb. (c-d) Hypothesized compensatory control mechanisms to regain functional control. A combination of either approach is likely. (a) In a healthy human or non-human primate, M1 provides the main descending control of the skeletal muscles, with assisting direct control of the surrounding regions (PMv, PMd depicted) (b) Loss of direct control of the descending M1 tracts due to an acute internal capsule lesion, mainly affecting cortico-fugal M1 tracts. (c) The contra-lesional hemisphere regains control of the impaired muscles through non-midline crossing corticofugal connections. (d) Surrounding motor areas (PMv, PMd), reconfigure their connectivity, to regain the control lost control of the adjacent M1.

discernible difference in clinical measures (Prabhakaran et al., 2008). A more in depth understanding of the processes of stroke rehabilitation and its recovery mechanisms are clearly needed (Figure 1.6).

1.2.5 Subcortical stroke in animal models

Only a few animal studies have focused on subcortical stroke in their animal models, despite the relatively prevalent occurrence in humans (Bailey et al., 2009). While in recent years more projects have focused on subcortical stroke in rodents (Frost et al., 2006; Otero-Ortega et al., 2017; Nam et al., 2020), non-human primates models have been very sparse. To date only models for subcortical stroke in NHP have been published: Lacquaniti et al. (1987); Puentes et al. (2015); Murata and Higo (2016) and Kim et al. (2021).

The first focal subcortical lesion in a macaque was thus reported by Lacquaniti et al.. They used an electrical stimulation approach to determine the location of the descending CST, over multiple electrode insertions. They set five electrolytic lesion, in areas that created the greatest upper-limb responses. The monkey showed profound flaccid paresis in one arm. While the animal regained the ability to grasp and climb during the recovery period of three months, precision grasping never returned and the unaffected limb remained the preferred one.

Almost three decades later, Puentes et al. published a model in marmoset monkeys, relying on occlusion of the anterior choroidal artery, a vessel mainly supplying subcortical areas.The arterial occlusion produced motor deficits in 60% of the animals. The three affected animals were reported to have general behavioral deficits up to the 10 day post lesion assessment.

In a study from 2016, Murata and Higo implemented an endothelin-1 (ET-1) induced vasoconstriction model. Taking a personalized lesioning approach, they determined the stereotactic coordinates, by employing MRI guided planning with the animals secured in an MR-compatible frame. The stroke was then administered on-site by 15 stereotactic injections of ET-1 in 5 separate tracks. The lesion size and progression were monitored over the following weeks using structural MRI imaging (T2-weighted). The measured infarct volume peaked after the first week post injection (600-1200 mm^3) and showed a rapid regression to 10% of its initial size over the following 3 months. Grasping performance was monitored using a reach- and grasp-task, forcing index thumb opposition (precision grip). They reported a wide span of functional outcomes ranging from recovery after a few days, to permanent functional impairment.

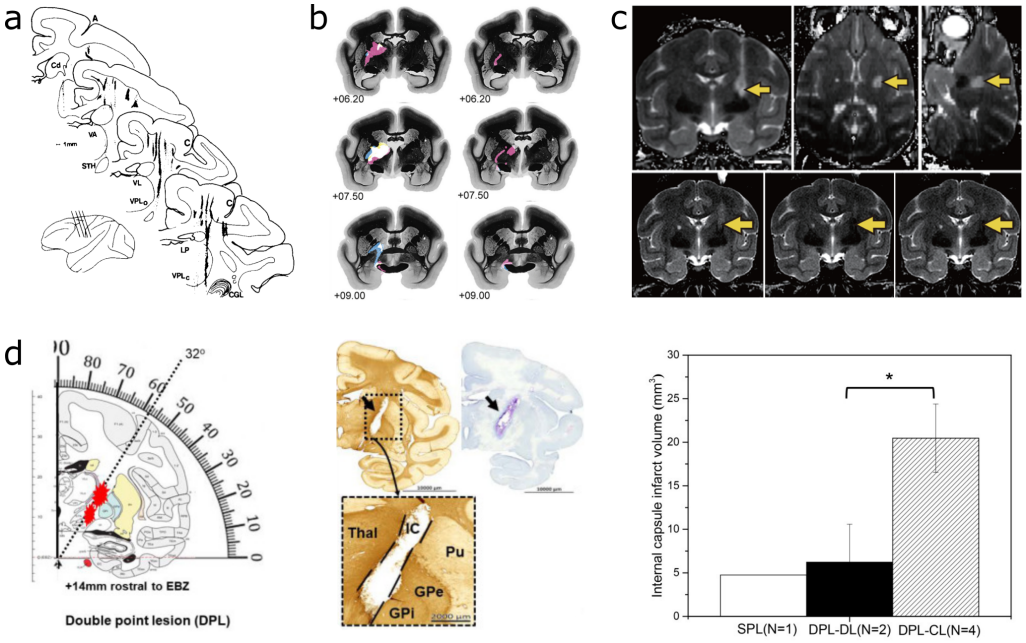

Figure 1.7: Previous subcortical stroke models in non-human primates (a-d) The reported location and extent of subcortical stroke lesions in non-human primates. (a) Depicts 5 electrolytic lesions placed, with guidance by electrical stimulation induced muscle evoked potentials in *M. fascicularis* (n=1). The lesion tracts are marked in black (Lacquaniti et al., 1987). (b) An anterior choroidal artery occlusion model in *C. jacchus*. Nissl stain preparations are depicted with the lesions marked in color with overlapping areas in white. The left column shows animals with a reported functional deficit (n=3), whereas the sections in the right column depict the lesions of animals without functional deficits (n=2) (Puentes et al., 2015). (c) An endothelin-1 induced internal capsule lesion model in *M. fuscata*. The lesion location and size were assessed by analysis of T2-weighted MRI images. The lesion location is marked by yellow arrows (n=1). The images depict example frames in a longitudinal sequence spanning 3 months post lesion: top - 1 day post lesion (l-r: coronal-transversal-sagittal); bottom - 1,2 and 3 months (l-r) post injection, showing a decline in the detectable lesion size by MRI imaging (Murata and Higo, 2016). (d) A photothrombotic lesion model, introduced by Kim et al. (2021). On the left the lesion plan for a double lesion is depicted (DPL-XX, n=6), the electrode is to be inserted at an angle of 32°14 mm rostral to the ear bars. In the middle, exemplary histological preparations of a correctly placed double lesion (DPL-CL, n=4) is depicted. On the right, the infarct volumes situated in the internal capsule are reported. The figures were adopted from Lacquaniti et al. (1987); Puentes et al. (2015); Murata and Higo (2016); Kim et al. (2021).

In the most recent study, Kim et al. (2021) proposed a lesion model inducing a large ablation of the internal capsule by employing photothrombotic lesioning. The technique was based on an *i.v.* injection of the chemical rose bengal, which releases reactive oxygen species when exposed to light, resulting in thrombus formation in the irradiated tissue. To achieve a local lesion, they stereotactically inserted an optical fiber cannula into the posterior limb of the internal capsule at an angle of 32°and $14mm$ rostral to the ear-bars, mirroring the angle of the descending tracts in the IC. Depending on the animal, they induced lesions at either a single site (n=1) or two sites (n=6). For 'correctly' placed double-lesions, they reported a lesion volume of $21 \pm 17.4mm^3$. The neurological assessment was conducted using a fine motor manual dexterity task, where animals with correctly placed lesions never achieved successful grasping in the 13 weeks of post-lesion testing.

While all three studies have their strengths, they all have clear deficiencies. In all cases, there is a lack of reproducibility and control of the lesion size and location, as well as the functional outcome they induce. While arterial occlusion produces a more 'natural' phenotype, differences in anatomy make standardized testing hard, especially in species where the number of involved animals should be kept low. In the case of ET-1 injections, the control of the lesion size is largely determined by diffusion of the injected reagent, producing highly variable lesion sizes even in highly controlled environments. A further drawback of the ET-1 injection is the extension of the lesioned tissue along the cannula tracts, caused by reflux during the retraction of the needle. In the most recent study of Kim et al. (2021), the induced lesion size, as well as the observed functional deficits remain unreliable. A clear need for a reliable NHP model for subcortical stroke therefore persists.

1.3 Study

1.3.1 Synopsis and Aim

In this thesis, we aim to understand the effects of a focal subcortical stroke on the upper-limb, especially in the hand in NHPs. We aimed to collect the fundamental knowledge on how such a lesion affects the corticofugal connections and the functional recovery progress thereafter. We hope that this might lay the groundwork to implement new rehabilitation paradigms, providing the basis for true motor function recovery after stroke.

We first needed to develop a model of subcortical stroke that would (1) be

precise and predictable in both location and size, (2) be translational, in the sense of impairment and recovery progress, and (3) spare the motor areas involved in the recovery. To achieve the required accuracy, we developed a maxillary retention mold and paired it with MRI-guided surgical planning. To monitor the evolution of behavioral changes before and after the lesion, we then had to develop and adapt a comprehensive battery of tasks that would be monitored by a multi-modal recording system, including 3D kinematics, intra-cortical recordings, electromyography and force output. After the animals were successfully trained in all tasks, and subsequently underwent the lesion-recovery paradigm, we traced three cortical areas of interest (M1, PMv and PMd) with viral and chemical anatomical tracers to assess the anatomical disruption of the stroke.

As the data collection was finished, we performed a detailed analysis the phenotype and anatomical correlates of our stroke model. We validated the robustness of the novel head retention system and quantified the lesion precision and their relative locations by registering the histological preparations to the Montreal Neurological Institute standard MRI space for *M. fascicularis*. We further quantified the amount spared CST from the traced motor cortical areas and analyzed their respective paths as they descend through the internal capsule, as well as their termination pattern in the spinal cord. The induced lesions were found to successfully interrupt the descending tracts of M1, while tangentially lesioning the more rostrally descending tracts of PMd and PMv. In the spinal cord, the M1 fibers were found to proportionally decrease with the fiber loss seen in the internal capsule. The kinematic phenotypes resulting from the described lesions were then analysed over a wider array of tasks, showing three distinct functional recovery groups: a mild group which regained prelesional level performances within the first month of recovery, a moderate group which showed slower functional recovery in most tasks, however they remained unable to perform any fine motor control tasks, and in the end a severe group which never regained the ability to reach nor grasp with the impaired arm. As an unexpected result, flexor-synergy like movement patterns could be observed in the severely impaired group. As part of a more in-depth analysis the underlying kinematic movement patterns in tasks were animals showed full functional recovery were quantified. Significantly altered movement strategies were observed despite the functional recovery, displaying a strong influence of compensatory adaptions in motor recovery.

1.3.2 Personal contribution

The work presented in this manuscript was performed in a highly collaborative environment with many key players contributing vital parts to the project. It is thus important to highlight my personal contributions in this study.

Chapter 1: (i) prepared the figures (ii) wrote the chapter

Chapter 2: (i) optimized and fabricated the maxillary retention molds (ii) assisted in MRI and CT acquisitions (iii) validated the maxillary retention precision (iv) optimized and assisted in surgical planning (v) assisted the surgeries in sterile condition (vi) performed the peri-surgical animal care (vii) performed the histological processing and imaging (viii) developed the registration pipelines (ix) quantified the lesion precision (x) prepared the figures (xi) wrote the chapter

Chapter 3: (i) trained the animals in Fribourg (ii) developed the adapted Box and Blocks test and the Drawer task (iii) assisted the surgeries in sterile condition (iv) performed the perisurgical animal care (v) performed the experiments (vi) analyzed behavioral tasks and co-developed the kinematic assessment pipelines (vii) prepared the figures (viii) wrote the chapter

Chapter 4: (i) performed the tracer injections (ii) performed the histological processing and imaging (iii) developed the fiber detection pipelines (iv) developed the CST quantification pipeline in the internal capsule (v) developed the registration pipeline (vi) prepared the figures (vii) wrote the chapter

Chatper 5: (i) prepared the figures (ii) wrote the chapter

Chapter 2

A novel model of subcortical stroke in non-human primates

One quarter of stroke patients suffer from a lesion situated in a subcortical region of the brain. In particular, infarcts affecting the internal capsule are known to produce severe and lasting motor deficits, often drastically decreasing the patients' ability to interact with the world through their hands. (Johnson et al., 2019) The exact mechanisms underlying the loss of control, and especially the subsequent recovery, remain enigmatic. While the study of subcortical stroke in patients can provide valuable insight on a phenomenological level, mechanistic studies using animal models are paramount to the development of new and effective treatment paradigms. In this chapter, a novel translational non-human primate model of internal capsular stroke targeting the corticospinal tract controlling the upper-limb is presented, providing a robust framework for translational research of subcortical stroke.

2.1 Radiofrequency thermocoagulation

Radio frequency thermocoagulation (RFTG) was first described by Réthi (1913). Today, it is a method routinely used in clinical settings. It has

been approved for various treatments, such as some cases of chronic pain, essential tremor or epilepsy (Chua et al., 2011; Narabayashi and Ohye, 1980; Guénot et al., 2011). The technology is based on irradiating tissue using radio waves, heating the neuronal tissue and thus temporarily disabling or permanently destroying it (Figure 2.1a).

The internal capsule is a relatively narrow structure. In *M. fascicularis* it only measures between 2 to 3 mm where the motor cortical CST descends. Specifically lesioning the internal capsule therefore requires a great degree of spatial control. In this project, a RFTG approach was chosen to meet these requirements. Specifically, the LG2 Lesion generator (Electrode: TCBA 011, inomed Medizintechnik, Germany) system was employed, as it allows for temperature regulated lesion production and has been shown to reliably produce lesions of a known size (Hauska et al., 2010). The lesion size can be regulated by two main parameters: temperature and irradiation time. The setup further allows for electrical stimulation at the electrode tip, enabling functional probing, during the surgery (Figure 2.1b).

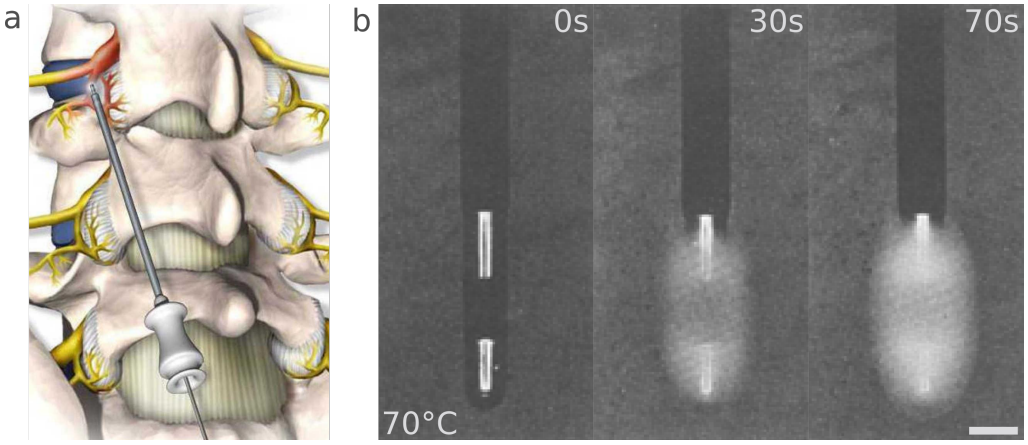

Figure 2.1: Radiofrequency thermocoagulation (a) Exemplary depiction of a surgical intervention targeting chronic pain in the spinal cord. (b) Time dependent lesion size introduced by a bipolar thermocoagulation electrode at 0s, 30s and 70s. The lesion generation was simulated in egg white. Scale bar: $1mm$. Figures adapted from Ariñez-Barahona et al. (2017) and Moringlane et al. (1989).

2.2 Methods

2.2.1 Animal Model

Four young adult (3.9 ± 0.5 years; Mk-Jy, Mk-Le, Mk-Pa, Mk-Re) female non-human primates (*Macaca fascicularis*) weighing $3.3 \pm 0.3kg$, and four adult males (4.3 ± 0.7 years; Mk-03, Mk-05, Mk-06, Mk-11) weighing $5.3 \pm 0.5kg$ were involved in this assessment. The four female monkeys were housed in an animal facility at the University of Fribourg (Switzerland). They were situated in an enriched housing environment of $45m^3$ in groups of 2 to 5 animals, as mandated by the federal animal protection rights. Additionally, they had access to an outdoor space of $30m^3$. The group had *ad libitum* access to water and were fed without food deprivation. All monkeys were subjected to a subcortical stroke-like lesioning procedure. They were implanted with six cortical micro-electrode arrays (UTAH array, Blackrock microsystems, USA). In two monkeys, these implants were combined with fully implantable EMG systems (Ripple neuro, USA). All experimental procedures were approved by the Swiss Federal and cantonal authorities under the license number: 2017_22_FR. The six males were held in an AAALAC accredited animal facility in Beijing (Motac Neuroscience, China). The animals were housed in cages, designed in accordance with the European guidelines (2m x 1.6m x 1.26m). The animals received enrichment such as toys, puzzles and music. All experimental procedures were approved by the Institutional Animal Care and Use Committee of Bordeaux (CE50, France) and performed in accordance with European Union animal protection regulations. The animals had *ad libitum* access to water and were fed twice daily.

2.2.2 Surgeries

Perioperative care

Before and after surgeries, and in the case of chronic complications, the animal's health status and weight were monitored and recorded daily. All incidental interventions were discussed and planned with the local veterinary advisors.

Pre-operative care One day prior to the surgery, the animal was sedated with an intramuscular (*i.m.*) injection of ketamine (Ketasol-100®, 10 mg/kg) and midazolam (Dormicum®, 0.1 mg/kg). The head was shaved and washed with antiseptic soap (Hibiscrub, Cito Pharma, Switzerland).

The animal was then injected subcutaneously (*s.c.*) with broad-spectrum antibiotics (i.e., Noroclav®, 30 mg/kg) or otherwise appropriate antibiotics, according to antibiotic resistances.

Post-operative care After the surgical intervention, the animal's wounds were antiseptically treated using Betadine solution (Mundipharma, Switzerland). They received injections of broad-spectrum antibiotics (i.e., Noroclav®, 30mg/kg, *s.c.*) or other appropriate antibiotics, according to their antibiotic resistances. Additionally, they received analgesic carprofen (Rimadyl, 4mg/kg, *s.c.*). The anesthesia was stopped, and the monkeys were kept warm and received oxygen until they regained consciousness. They were then transferred to a small cage and monitored until they had completely recovered from the effects of the anesthesia. The monkeys were then fed and hydrated, before they were, again, transferred into a large cage in their housing room to prevent in-group fighting due to the subjects' weakened state. In the cage, they had access to food and *ad libitum* water.

Over the 10 days following the surgical intervention, the animals received subcutaneous injections of antibiotics (i.e., Noroclav®, 30 mg/kg) and carprofen (Rimadyl, 4 mg/kg). Their sutures were evaluated daily and, if needed, washed with Betadine solution or Hibiscrub®(Cito Pharma, Switzerland) and Prontosan®(B. Braun, Switzerland).

Chronic wound care Some animals suffered from chronic wound complications, such as skin retraction or general inflammation around the implants. Indications of this included reddening of the skin and pus. In the presence of pus, an antibiotic sensitivity test was administered in order to determine whether any antibiotic resistant strains of bacteria were present. Guided by this test, an antibiotic regime was devised and administered accordingly, under veterinary supervision. Where appropriate, a routine of wound-cleaning with Betadine solution (Mundipharma, Switzerland) and a combination of Hibiscrub®(Cito Pharma, Switzerland) and Prontosan®(B. Braun, Switzerland) was added.

Anesthesia

Surgical intervention The day of the surgery, sedation of the animal was induced with an *i.m.* injection of ketamine (Ketasol-100®, 10 mg/kg), midazolam (Dormicum®, 0.1 mg/kg), and methadone (Methadone®, 0.2 mg/kg). It was transported to the surgical theater, where an intravenous access was placed. Sedation and analgesia was controlled via a combination of con-

tinuous propofol 1% and ringer-lactate (dilution 1:1) infusion, combined with fentanyl (1:1 in 0.9% saline). General hydration was provided through this continuous warmed infusion of ringer-lactate, via the *i.v.* access. The animal's heart rate (ECG), core temperature (rectal probe), oxygenation (SO_2), and breathing rate were continuously monitored and recorded every five minutes. Depending on the procedure, the animal was placed onto the surgical table in either a prone position or fixed in a stereotactic frame. In the case of the stereotactic frame, the ear-bars were covered with lidocaine-cream (2%). The animal's head was fixed by 5 contact points: ear-bars, ocular-bars and a mouthpiece or custom dental mold (Chapter 2.2.5). The animals body temperature was kept stable with the help of a heating pad, as well as drapes and latex gloves filled with warm water. Additional oxygen (3 L/min) was provided through a tube placed in front of the nose. A sterile field was established with sterile drapes that left the monkey's head exposed and able to be antiseptically prepared with Betadine solution (Mundipharma, Switzerland).

Off-site imaging The computer tomography (CT) and magnetic resonance imaging (MRI) scans were performed at the cantonal hospital of Fribourg (HFR). At the animal facility, the monkey was lightly sedated with an intramuscular (*i.m.*) injection of ketamine (Ketasol-100®, 10 mg/kg) and midazolam (Dormicum, 0.1 mg/kg) and transported to the imaging facility. On site they received a second *i.m.* injection of ketamine (Ketasol-100®, 4 mg/kg) and medetomidine (Dorbene®, 0.04 mg/kg). After the completion of the imaging session, the animal received an *i.m.* dose of atipamezole (Alzane, 0.2 mg/kg), counteracting the medetomidine, before being transported back to the animal facility. There, the monkey was monitored and kept in a separate cage until fully awake and past post-anesthesia effects. The animal was then fed, hydrated and released back into the home cage.

2.2.3 Structural MRI

The MRI scans were performed at the cantonal hospital of Fribourg (HFR).The animals were sedated and transported to the imaging facility as described in chapters 2.2.2 and 2.2.2. They were placed in a prone position into an MRI-compatible stereotactic frame (9-YSTI-22-P, Crist Instruments, USA), fixing the head with the personalized dental mold (chapter 2.2.5), eye-bars, and ear-bars (covered in lidocaine cream, 2%). A positional calibration frame, with parallel and perpendicular vitamin-A filled rods, was attached to the stereotactic frame in order to control its position within the MRI. During the procedure, the animals' vitals were monitored using ECG and

pulse oximetry. The monkey received additional oxygen (3L/min) via a tube placed in front of its nose. The body temperature was kept stable using gloves filled with warm water and preheated cloth sheets. For the surgical planning, both T1 and T2 structural MRIs were acquired. The T1 MRI data were acquired using the 3D BRAVO sequence (General Electric, USA). The protocol consisted of 256 sagittal images, with a voxel size = $0.7mm^3$, and a spatial resolution = $0.625x0.625x0.7mm^3$ The animals were then cared for and transported back to the facility, as described in chapter 2.2.2.

2.2.4 CT scan

The animals were sedated and transported to the imaging facility, as described in chapters 2.2.2 and 2.2.2. The subjects were put into a prone position, and set down on the acquisition bed. Bubble wrap and warm water filled gloves were used to keep the core temperature from dropping. The CT scan of the monkeys head was acquired by employing a $0.6mm$ helicoidal low dose protocol (Ingenuity TF, Philips, Netherlands). The animals were then cared for and transported back to the facility as described in chapter 2.2.2.

2.2.5 Maxillary retention system

The animal was sedated with an *i.m.* injection of ketamine (Ketasol-100®, 4 mg/kg) and medetomidine (Dorbene®, 0.04 mg/kg). Multiple maxillary imprints were taken using a mixture of alginate (Blueprint X-creme, Dentsply Sirona, Germany) and water applied onto a cut down maxillary impression tray. The hardened alginate imprints were stored in a covered plastic box with some water, to avoid deformation. Positive maxillary models were formed with casting ceramic (Suter Kunststoffe, Switzerland) mixed with water. Before the ceramic had fully hardened, a pipette tip was inserted into the ceramic to allow easier handling (Figure 2.2a). The personalized, stereotactic frame (Crist Instruments, USA) compatible, dental molds were cast with acrylic (SCS-Beracryl D28, Suter Kunststoffe, Switzerland). A clay basin was used as an outer casting shell, with a stereotactic adapter rod incorporated into it. The ceramic positive was lowered into the basin and attached to a third hand by the pipette tip. The basin was then filled with acrylic until it reached the upper edges of the maxillary print. After hardening, the acrylic mold was extracted, and the ceramic carved out and discarded. The acrylic was cut and sanded down as much as possible to retain stability while minimally obstructing the animals' mouths and air-

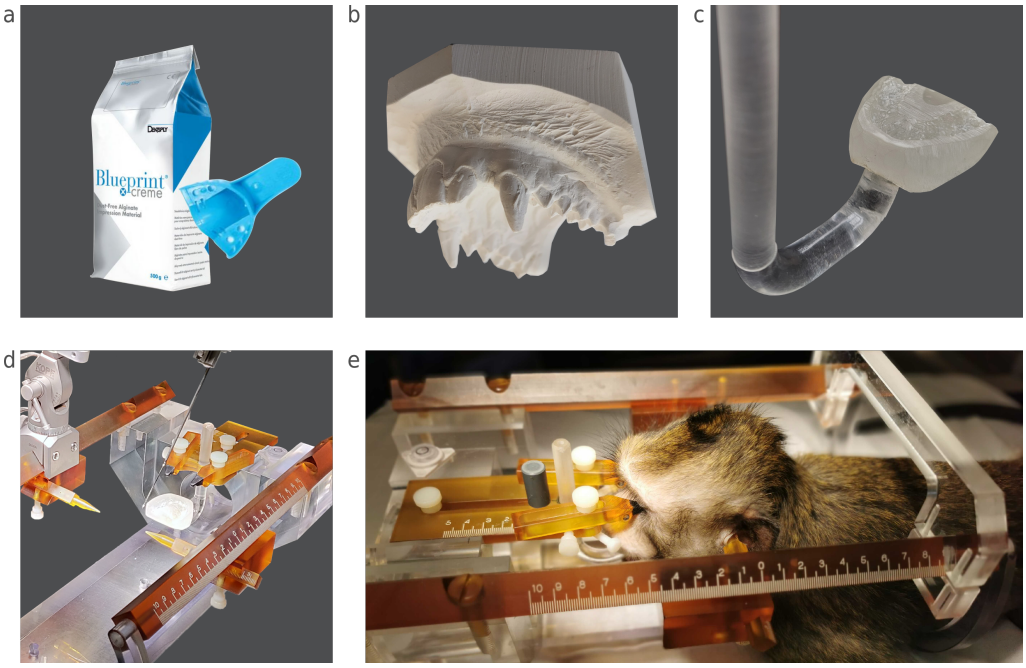

Figure 2.2: MRI compatible maxillary mold head-retention system (a-e) Depiction of the maxillary mold fabrication steps and its integration into the MRI compatible frame. (a) Material utilized to take maxillary impressions from subjects (b) Ceramic positive of a maxillary imprint taken from one of the subjects. (c) The acrylic maxillary mold fused with the retention rod. (d) The MRI compatible stereotactic frame with the ear-bars and the maxillary mold in position, simulating a lesion induction surgery. (e) A monkey sedated and restrained with the stereotactic frame.

ways. As a final step, the adapter rod was heated with a heat gun, and the dental mold was leveled to obtain optimally level head positioning during further procedures (Figure 2.2b). The maxillary mold was then ready to be inserted into the mouth retention mechanism of the MRI-compatible stereotactic frame. To fix the retention mold in a stable position, the respective subject was sedated and fastened in the stereotactic frame (Figure 2.2e). The mold was then blocked in the optimal position, and a position retention piece was secured to the retention rod with plastic screws. The screw positioning was then further secured by drilling small divots into the retention rod, where the screws meet the rod, ensuring the exact same positioning of the dental mold, even after accidental disassembly.

2.2.6 Validation of the maxillary retention system

In order to validate the precision of the placement and head-retention over multiple interventions, multiple MRIs with the animals' heads retained us-

ing the maxillary retention system, were acquired. The sessions were spaced between 1 week and 6 months apart to simulate a suitable delay between the imaging session and the lesion administration. T1 weighted images were acquired, as described in chapter 2.2.3.

The acquired image series were then analyzed with the Slicer3D software package (Fedorov et al., 2012). A landmark based rigid registration (DOF:6) was performed using the tips of the vitamin-A filled orientation rods (Methods 2.2.3) as landmarks in both series. In the aligned volumes, 6 manually identified landmarks were selected: the mid points of (1) the right eye, and (2) the left eye, (3) the anterior commissure, (4) the most posterior apex of the 4th ventricle, (5) the most anterior aspect of the genu, and (6) the most posterior apex of the corpus callosum (Frey et al., 2011). The variance of placement between homologous structures, acquired with the same maxillary mold, were calculated.

2.2.7 Lesion planning

To optimally target the internal capsule during the lesioning intervention we employed the StealthStation system (Medtronic, Dublin, Ireland). This system allowed us to determine the optimal access route and target from the structural MRI acquisition, using the MRI compatible frame as a reference coordinate system. The planning target was set at the depth of the anterior and posterior commissure (AC/PC), and around 8 mm lateral to the midline. To primarily target the descending M1 projections the target was set around the midpoint between AC and PC, and situated in the posterior IC genu. The resulting planning was subsequently simulated in the surgical environment using 3D printed models of both the skull and brain of each animal. The data for the 3D printing was extracted from the CT scan and the structural MRI for the skull and brain respectively (Figure 2.3).

2.2.8 Thermolesioning

The animals were prepared for surgery and sedated as described in chapters 2.2.2 and 2.2.2.

The animal was positioned in a prone position and its head fixed in a stereotactic frame (Crist Instruments, USA) with the custom dental mold (Chapter 2.2.5). The stereotactic tower (Kopf Instruments, USA) with the lesioning electrode (TCBA 011, inomed Medizintechnik, Germany), with its angles set according to the virtual lesion planning (Chapter 2.2.7), was

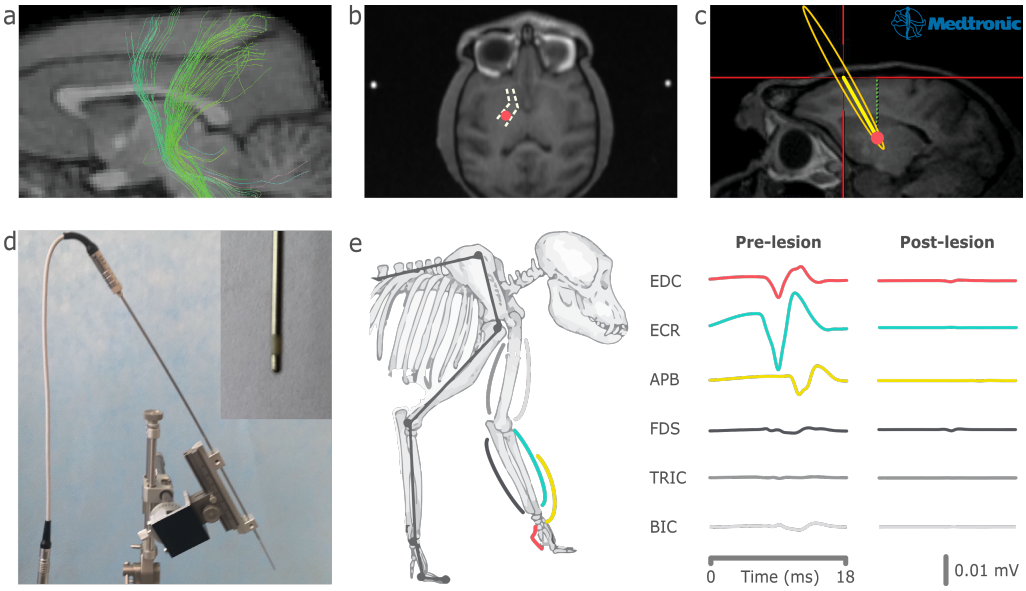

Figure 2.3: Lesion in the internal capsule (a-e) Depiction of the internal capsule lesion planning and execution. The planning was done according to the location of the descending tracts of the motor cortices through the internal capsule. The planning was conducted on a structural MRI of the subjects using the Stealthstation (Medtronic, Ireland). During the surgery, the optimal positioning of the electrode was further verified with motor evoked potentials induced by the lesioning electrode. (a) Diffusion tensor Imaging data, showing corticospinal tracts of the primary motor cortex through the internal capsule. (b) An axial slice at the level of the anterior and posterior commissures, with the optimal target for the lesion depicted in the structural MRI (red), with the outlines of the internal capsule depicted in white. (c) The optimal trajectory for the lesion induction planned with the Stealthstation. The chose trajectory avoids all motor areas and is set at a $60°$ angle from the axial plane. (d) The thermolesioning electrode mount with lesion electrode and high precision stereotactic inserter. The electrode tip is magnified in the top right image. (e) Exemplary electromyography (EMG) measurements before and after thermolesion induction of the muscle evoked potentials (MEP) generated by the lesioning electrode at the lowest point of lesion induction. Pre-lesion a distinct activation was measured in the distal musculature: extensor digitorum communis (EDC), extensor carpi radialis (ECR), abductor pollicis brevis (APB), and flexor digitorum superficialis (FDS). MEPs were absent in the proximal muscles: biceps (BIC) and triceps (TRIC). Post-lesional measurements showed only residual activation of the distal muscles, confirming the disruption of the electrode surrounding tract. MEPs were evoked with $2Hz$ stimulation at $1mA$.

put into place, and the exact incision location was determined. The tower was removed, and a small incision and subsequent craniotomy, were conducted at the entry point on the skull. The dura mater below was then minimally incised. With the stereotactic arm re-positioned, the electrode was slowly and precisely lowered into the brain. To determine the optimal lesion site *in vivo*, electrical stimulation trains (2 Hz and 50 Hz) visually monitored muscle responses in both the hand and arm. At incrementing electrode depths, the threshold and predominantly activated muscles were recorded. Electrically evoked muscle responses were recorded ranging from 5 mm above, to 3 mm below target. Lesions were induced at the depths most specific to hand movements and with the lowest thresholds. Mk-Re and Mk-Pa received lesions at one specific depth each, whereas Mk-Le and Mk-Jy received two lesions placed 2 mm apart (Table 2.1). The lesions were induced by radio frequency wave emissions around the tip of the inserted lesioning electrode. These emissions of the electrode were specifically tuned to heat surrounding tissue in a 1.5 mm radius (Moringlane et al., 1989). The tissue surrounding the electrode was heated to 90°C for 60 seconds. The electrode was then kept in place for another minute before it was moved up to the next lesion spot, or extracted from the brain. After each heating step, the electrical stimulation protocol was repeated and the threshold and muscular response quality was recorded. After extraction of the electrode, the skin was sutured and antiseptically treated.

Post operative care was administered as described in chapter 2.2.2.

2.2.9 Perfusion and Tissue extraction

The animal was sedated with a mixture of ketamine (Ketasol-100®, 10 mg/kg), midazolam (Dormicum®, 0.1 mg/kg) and methadone (Methadon®, 0.2 mg/kg). The animal was transported into the surgical theater where it received an intravenous injection of pentobarbital (60 mg/kg, diluted in 0.9% saline solution). Post-injection, the animal's vitals were continuously measured using ECG and SO2 monitoring. When the animal stopped responding to physical stimuli (eye-lid reflex and pinching of the hand) it was transferred to the perfusion area. The heart was exposed by opening the thorax. The left ventricle was then injected with 1ml of heparin, before it was incised, a cannula inserted, and transcardial perfusion (0.1M PBS) was initiated. The perfusion medium was switched to 4% paraformaldehyde in 0.1 M PBS. After perfusion, the brain and spinal cord were extracted and fixated over night in 4% paraformaldehyde, before being transferred in 0.1M PBS azide (0.03%) solution.

	Mk-Re		Mk-Pa		Mk-Jy		Mk-Le	
Δ Target [mm]	Threshold [mA]	Muscles	Threshold [mA]	Muscles	Threshold [mA]	Muscles	Threshold [mA]	Muscles
-5	7	DEL						
-4			3	FPB	4.5	FPB & FDC	2.5	FPB
-3								
-2	4	FPB	2	FPB	2	FPB & FDC	2	FPB
-1			1.1	FPB & FDP				
0	1.2	FPB & EDC	1.5	FPB & FDP	1	FPB & FDS	1.3	FPB & FDP
1							0.9	FPB & FDP
2	4	FPB & SCA			1.2	FPB & FDS	0.8	FPB & FDP
3							0.8	FPB & FDP

	Mk-03		Mk-05		Mk-06		Mk-11	
Δ Target [mm]	Threshold [mA]	Muscles	Threshold [mA]	Muscles	Threshold [mA]	Muscles	Threshold [mA]	Muscles
-5	3	FCR						
-4	3	FCR	3	FCR				
-3	4	FCR						
-2	4	FDS	3	FCR & FDS	5	FPB & FDS		
-1	3	FDS & FCR						
0	4	FDS	1	FPB	3	FPB & FDS	3	BIC
1							4	FDC
2							1.3	FCR, FDS, BIC
3							1	FCR & FDS

Table 2.1: Internal capsule lesion surgery and muscle responses The muscle responses and the corresponding stimulation threshold at $2Hz$ stimulation frequency are reported for various depths (Δ Target) along the electrode insertion path. The insertion depth according to the MRI planning in Mks-Re, Pa, Jy and Le is denoted as 0 depth. The targeting in Mks-03, 05, 06 and 11 were based on a generalized lesion plan. The positions of lesioning are denoted in red. Muscles are abreviated as: BIC - Biceps ; DEL - Deltoid; EDC - Extensor digitori communis; FCR - Flexor carpi radialis; FDP - Flexor digitorum profundus; FDS - Flexor digitorum superficialis; FPB - Flexor pollices brevis; SCA - Scalene

2.2.10 Post-mortem DTI

The post-mortem MRI scans were acquired with a 9.4T MRI scanner (Varian, Resonance Research, USA), in collaboration with the Center for Biomedical Imaging (CIBM, EPFL, Switzerland).

The brain was removed from the storage container, dried, and placed in a custom made tubular acrylic glass container (100 mm x ∅60 mm (OD), ∅55mm (ID)). The inner diameter of this tube allowed the brains to snugly fit into the tube, without compression. To accommodate differently sized brains, an additional acrylic glass insert could be fixed in the tube, reducing the effective inner diameter and thus keeping smaller brains stable during acquisition. After insertion of the brain, the container was filled with Fomblin®Y (discontinued, Merck 317942, Germany). The container was then closed with a pressure fitted lid with a $\varnothing 1mm$ air hole. The sample was degassed at $\sim 60mbar$ for one hour, before it was sealed with Parafilm™(Bemis Company, USA) to prevent leakage. A post mortem DTI scan was then acquired over the next 48 hours. The diffusion MRI data were acquired using a pulsed-gradient spin echo (PGSE) sequence. The protocol consisted of 164 images: 4 $b = 0$ (non diffusion-weighted), 30 directions at $b = 1.8ms/\mu m2$, 30 directions at $b = 3.5$, and 100 directions at $b = 5.3$.

Other sequence parameters included: gradient duration = $6ms$, gradient separation = $37ms$, echo time $49.5ms$, repetition time = $11s$, and spatial resolution: $0.55x0.6x0.6mm^3$. After the scan sequence, the brain was extracted, cleaned, and transferred into 0.1 M PBS-azide (0.03%) for further histological processing.

2.2.11 Histological tissue preparation

The extracted brains were dissected into 7 pieces (anterior, medial and posterior pieces of each hemisphere and hind brain/cerebellum). They were then transferred into a sucrose-PBS solution: 20% sucrose in 0.1M PBS for one week, followed by 30% sucrose in 0.1M PBS for another one to two weeks. The tissue was then frozen by submerging it in iso-pentane for 10 minutes at -65°C (SnapFrost®80, Alphelys, France). The tissue was then transferred into a -80°C freezer. The tissue blocks were then cut into 50μm sections with a cryostate. The sections were stored in 0.1 M PBS azide (0.03%) for further processing.

2.2.12 Stroke size and location

All images were processed with QuPath (Bankhead et al., 2017) for primary image processing and Python for secondary analysis.

The lesion and surrounding structures (putamen, external and internal globulus pallidus, caudate, thalamus and substantia nigra) were traced visually. Lesion size and precision, represented by the overlap with the internal capsule and other structures, was calculated. To obtain a generalized localization of the stroke's location and impact, the histological slices were then registered to the MNI *M. fascicularis* atlas (Frey et al., 2011) (Chapter 2.2.13). The obtained spatial transforms were then applied to the lesion annotations for group wise analysis in the atlas space.

2.2.13 Registration

Due to size restrictions of the histological slide scanner (VS120, Olympus, Japan), which only allowed for single hemisphere slices, the hemispheres had to be registered to the MNI atlas space(Frey et al., 2011) individually. To achieve this, each sections DAPI channel and various annotations and segmentation results (labeled fibers) were exported (64x down-scaling) with QuPath (Bankhead et al., 2017). Artifacts, such as grease-pen marks, were manually marked and removed. The images were then blurred using a gaussian blur (radius: $2\mu m$) before the images were scaled down by a factor of

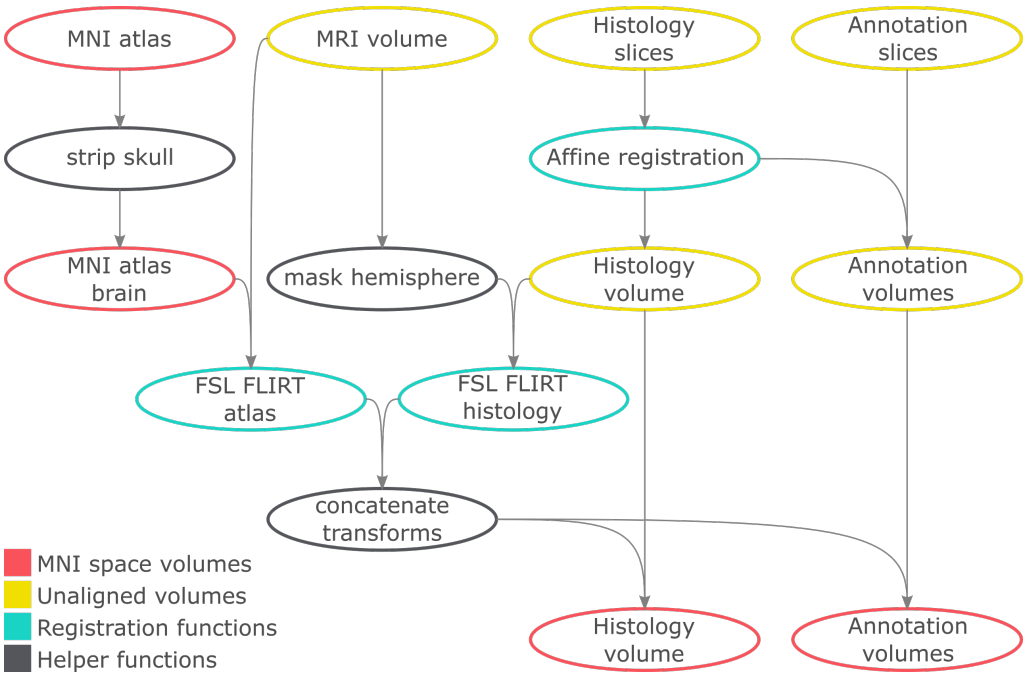

Figure 2.4: Registration of histological slices to MRI atlas A flow chart depiction of the pipeline employed to register the histological slices to a common MRI atlas space (MNI atlas of *M. fascicularis*, (Frey et al., 2011)). There were four inputs to the registration pipeline (top-row): (1) the MNI atlas, functioning as a reference space for the final transforms; (2) the MRI volume, the individual b0 volumes obtained during the post-mortem MRI; (3) the Histology slices, a series of histological sections (1 hemisphere, thickness: $50\mu m$, inter-section distance: $250\mu m$) encompassing the medial section of the brain; and (4) the Annotation slices, multiple series of histological annotations (e.g. lesion, M1 tract) corresponding to the histological sections. Within the pipeline, these parts get sequentially registered to their counterpart by three functions: (1) Affine registration, which builds an aligned volume from the histology slices [DoF 12]; (2) FSL FLIRT atlas, which aligns the post-mortem MRI to the skull stripped MNI atlas [DoF:12]; and (3) FSL FLIRT histology, which registers the histological volume to the corresponding hemisphere of the post-mortem MRI. The three helper functions: (1) strip skull: removes the skull pixels from the MNI atlas employing FSLs BET algorithm; (2) mask hemisphere: masks the un-used hemisphere of the post-mortem MRI to facilitate registration; and (3) concatenate transforms: concatenates the obtained transformation matrices from the FLIRT algorithms and then applies the resulting transform to the histology derived volumes.

64. The resulting sections were then sequentially aligned, using a manually selected middling section as a seed. This section was selected for a maximally straight mounting angle, minimal deformation, and maximally intact structures. A rigid, pairwise registration algorithm (cost function=mutual information, DoF:6; (Lowekamp et al., 2013)) was used for registration, resulting in a volume (H-volume) representing the medial part of one hemisphere. The set of transformation matrix was then applied to the exported annotations, resulting in individual volumes corresponding to the H-volume space. To ensure the compatibility with the subsequent pipeline, the volumes were saved in the NIFTI file format, and the corresponding header was created.

As a primary reference for the registration to MRI space, the structural volume (b0) of the individual post-mortem DTI scans were used (Chapter 2.2.10). Before any further processing, both the H-volume's and the b0's dimensions were adjusted to match the MNI space's dimensions. The hemisphere corresponding to the H-volume was then masked in the individual volume. The H-volume was registered to the masked volume using FSLs FLIRT algorithm (cost function: mutualinfo, DoF: 9, (Woolrich et al., 2009)).The unmasked b0 was then further registered to the skull stripped (FSL BET, (Woolrich et al., 2009)) MNI atlas, using affine FLIRTs affine registration method (FSL, cost function: mutualinfo, DoF:12, (Woolrich et al., 2009)). The obtained transformation matrix was applied to the once transformed H-volume, resulting in MNI atlas aligned histological slices. The transformation matrices of the primary and secondary alignment were then sequentially applied to the annotation volumes, allowing fully standardized analysis of the histological results in the MNI space (Figure 2.4).

2.3 Results

2.3.1 Maxillary retention system validation

To assess repeatability and precision of the maxillary retention system, multiple planning MRIs per maxillary mold and animal were acquired from Mk-Jy, Mk-Pa and Mk-Le. The acquisitions spaced 2 weeks to 6 months apart were rigidly registered using the stereotactic frames' alignment bars (Methods 2.2.6 and 2.2.3). A qualitative measure of the overlap quality was achieved via a multi color blending assay (Figure 2.5), showing a well-aligned skull and brain, with larger deviations in the jaw and neck area. To quantify the shift in brain position between the imaging sessions homologous landmarks were marked in all MRIs, and their distance post registration

was calculated, yielding an average displacement of $0.37 \pm 0.28mm$ between sessions and landmarks(Figure 2.5d)

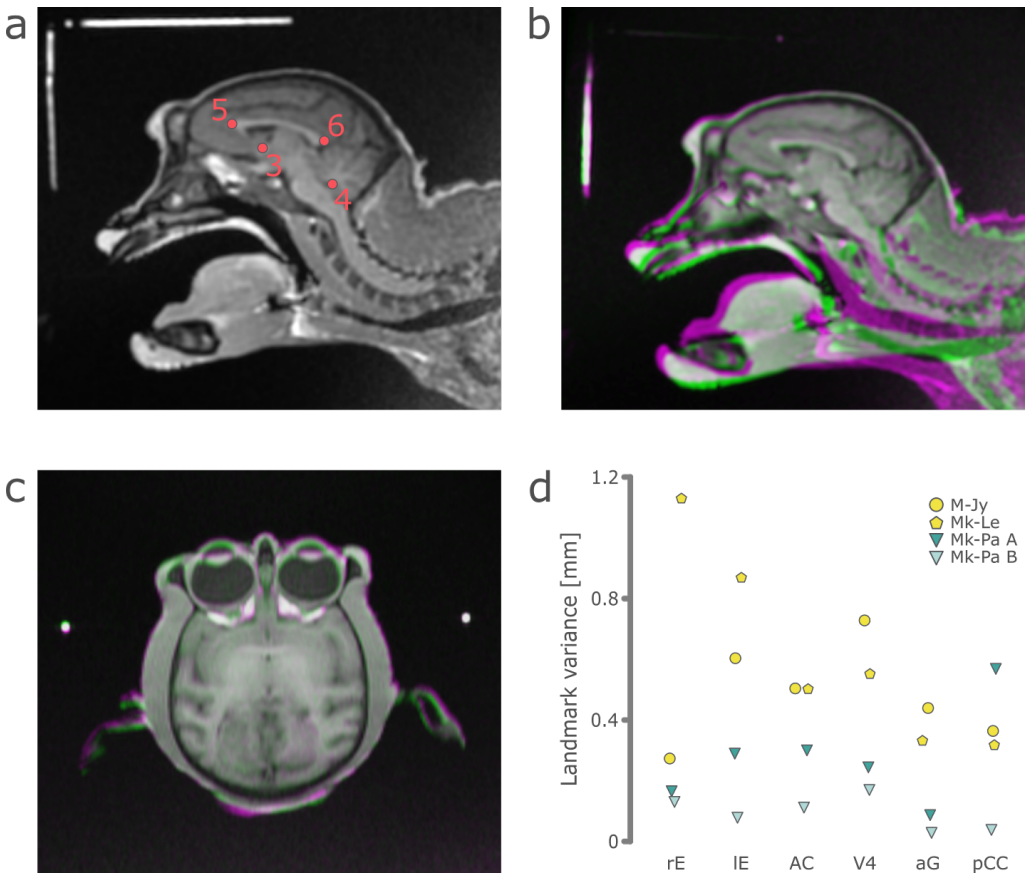

Figure 2.5: Maxillary retention system validation The maxillary mold retention precision was validated by rigid landmark registration of multiple MRIs taken weeks to months apart. The landmarks were placed on the vitamin-A calibration bars (Methods 2.2.3). (a) Example MRI of Mk-Jy with head restrained in the MRI compatible stereotactic frame, with a part of the calibration bars visible (top-left) and the visible landmarks are depicted (b,c) Overlap of two aligned MRIs taken 1 month apart. Sections in gray are well aligned, colorful sections depict miss-matching sections (Mk-Jy; 12.12.2018-purple, 11.01.2019-green) (d) The variance of 6 manually marked homologous structures, over multiple MRI acquisitions (n=10). The variances were calculated for the stereotaxic placement using the same maxiallary mold. A second maxillary mold was used for Mk-Pa after dental changes due to injury, resulting in molds A and B. The depicted landmarks are: (1) rE - mid point of the right eye, (2) lE - mid point of the left eye, (3) AC - Anterior commissure, (4) V4 - posterior apex of the 4th ventricle, (5) aG - anterior aspect of the genu, and (6) pCC - posterior aspect of the corpus callosum.

2.3.2 Lesion precision

One of the studies' aims was to produce a wide range of lesion sizes, producing phenotypes showing full (mild), partial (moderate) and absent (severe) recovery. The induced lesion sizes were thus chosen to fit two different size ranges: small ($\sim 10mm^3$) and large ($> 30mm^3$). The smaller lesions were used to induce mild to moderate phenotypes, whereas the larger lesion were chosen for the severe group. The group severity was determined using the kinematic recovery patterns, discussed in chapter 3. The extent of the induced lesion was determined histologically after completion of the functional experiments. This was achieved by marking the lesion on equidistant coronal sections ($50\mu m$ thick slices taken at $300\mu m$ intervals) of each lesioned animal ($n = 8$). The induced lesion sizes ranged from $6.8mm^3$ (Mk-JY) to $93.1mm^3$ (Mk-06) with group-wise lesion sizes of $11.0 \pm 0.6mm^3$ in the mild, $10.2 \pm 3.4mm^3$ in the moderate, and $51.5 \pm 24.7mm^3$ in the severe group (Figure 2.6). To determine the lesion location and precision the internal capsule and the surrounding structures (caudate, thalamus, pallidum, and striatum) were manually marked, and the volume of the lesion in each of the marked structures determined. The sub-volumes were then normalized by the total volumes of each animal to determine the fractional distribution in each structure. Over all animals, $73.5 \pm 7.9\%$ of the lesion volume was located in the internal capsule, with smaller portions found in the thalamus $12.9 \pm 9.5\%$, pallidum $10.2 \pm 9.5\%$, and striatum $3.4 \pm 4.9\%$ (Figure 2.6).

2.3.3 Lesion registration

Due to individual differences in brain size and structures as well as variances in histological tissue processing, such as the cutting angle, quantitative assessments of the relative lesion positions subject to high variability. To solve this, the histological slices were registered to an MRI atlas (MNI *M. fascicularis* atlas (Frey et al., 2011), Figure 2.7)) to overcome inter-individual variance. In the common atlas space the lesion distribution becomes quantifiable. Differences can be seen especially in the dorso-ventral distribution. The lesions producing a mild phenotype are generally situated in the superior IC above the axial AC-PC plane. Moderate outcomes are seen with lesions situated in the inferior IC, especially centered around the AC-PC plane. With their vastly larger size, the severe lesions span from the superior to the inferior IC (Figures 2.7 and 2.8). A further distinguishing difference can be found in the anterior-posterior direction, with the severe group showing a general caudal shift.

The precision of the lesion planning was then assessed by measuring the

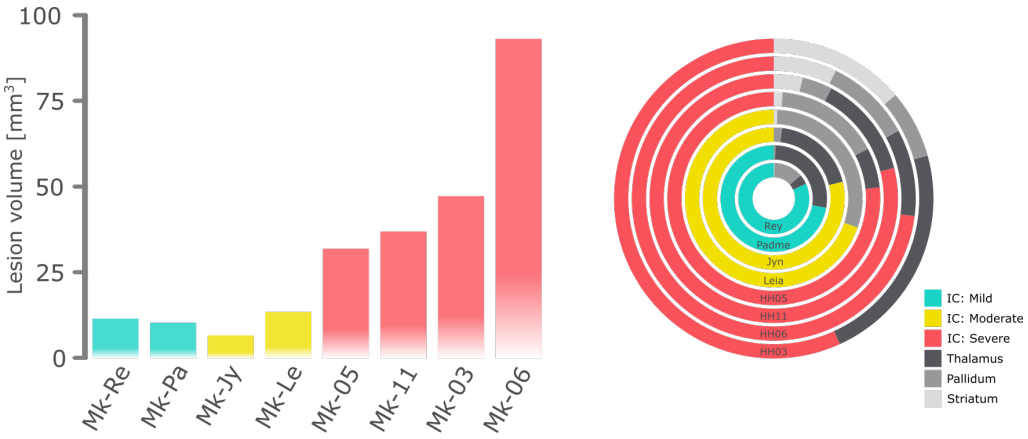

Figure 2.6: Internal capsule lesion size and precision (A) Total lesion volumes per subject, with group lesion sizes of: mild - $11.0 \pm 0.6mm^3$; moderate - $10.2 \pm 3.4mm^3$; severe - $51.5 \pm 24.7mm^3$ (B) Total volume distribution of lesions in the internal capsule (IC) (depicted in severity group colors) and the surrounding structures. The internal capsule was targeted with an accuracy of $73.5 \pm 7.9\%$ (A,B) The measurements were marked and summed on a histological series of $50\mu m$ thick slices taken at $300\mu m$ intervals. The severity groups were determined by the functional recovery, discussed in chapter 3

distance of the original lesion planning on the in-vivo structural MRIs to the induced lesion. Here it may be worth noting again that the lesion planning could only be conducted in the animals that were situated in Fribourg, due to a lack of access to an imaging facility in Beijing. For this analysis, the planned electrode entry points and targets were registered to the MRI atlas, using the in-vivo MRIs. The targets were adjusted for the chosen burning depth during surgery, and shifted along the electrode trajectory accordingly (Chapter 2.2.7). The distance between the lesion centroid and the adjusted target was then measured in atlas space. In 75% of animals the error of the lesion plan could be kept under $2mm$, whereas in Mk-LE the lesion error was $3.25mm$. On average the lesion plan accuracy was determined to be $2.3 \pm 0.6mm$. The error of the access trajectory angle was estimated as to be the angle between the adjusted target and the lesion centroid, and the adjusted target, respectively. A shift in the medio-lateral angle was close to nonexistent ($0.3° \pm 0.2°$). In the dorso-ventral plane, the average tract deviation was $4.2° \pm 1.9°$, with the three accurate subjects showing a deviation of $3.2° \pm 0.2°$ and the outlier Mk-LE being off by $7.1°$ (Figure 2.8).

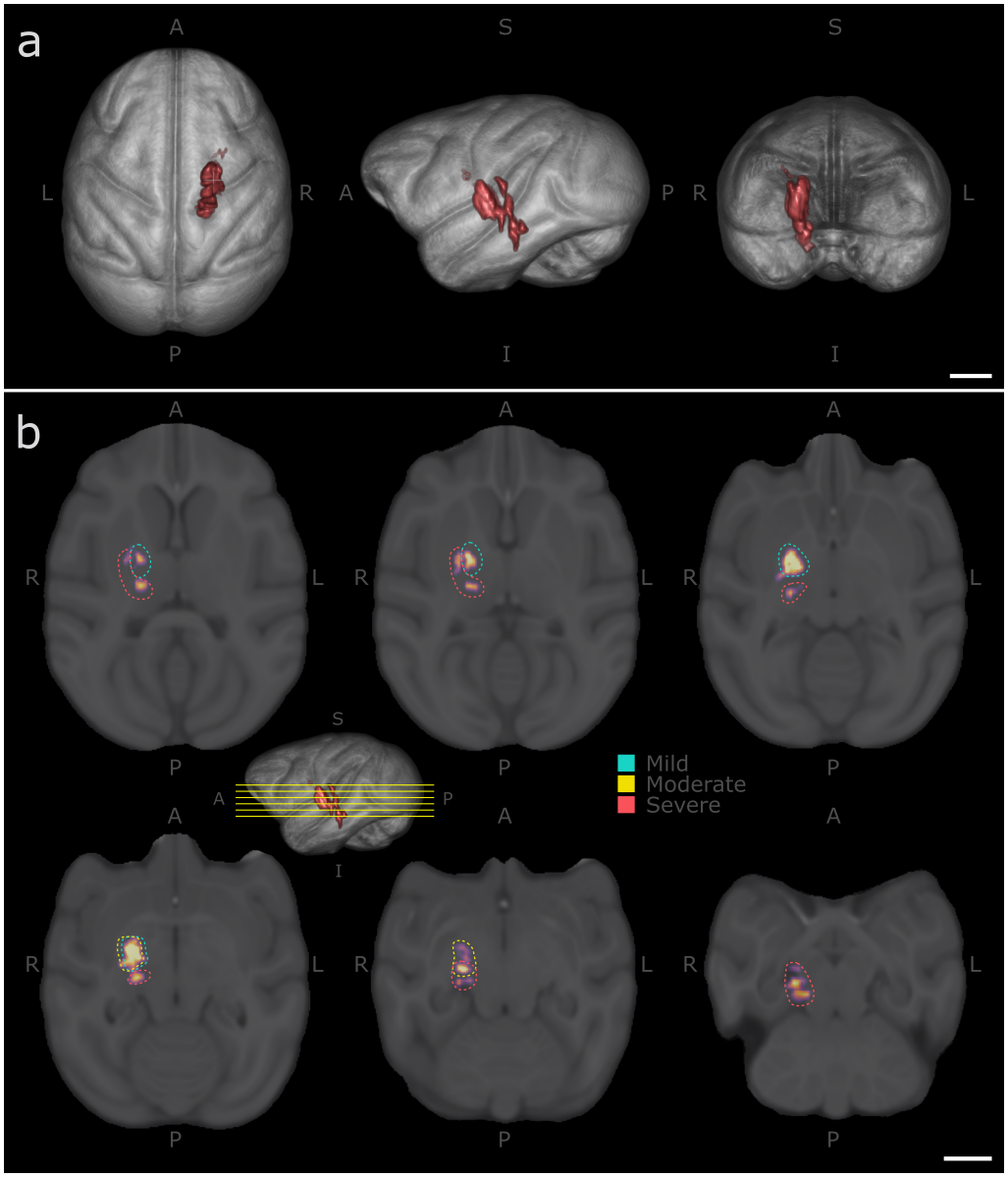

Figure 2.7: Lesion registration to MNI *M. fascicularis* atlas (a,b) Internal capsule lesions have been traced on histological slices before being aligned to the MRI atlas (chapter 2.2.13, MNI *M. fascicularis* atlas (Frey et al., 2011)). (a) 3D views of aligned lesions (n=6) of the mild, moderate, and severe groups (n=2 each) (axial-sagittal-coronal) (b) Equally spaced axial sections of the internal capsule lesions. The lesions are outlined by their corresponding group color.

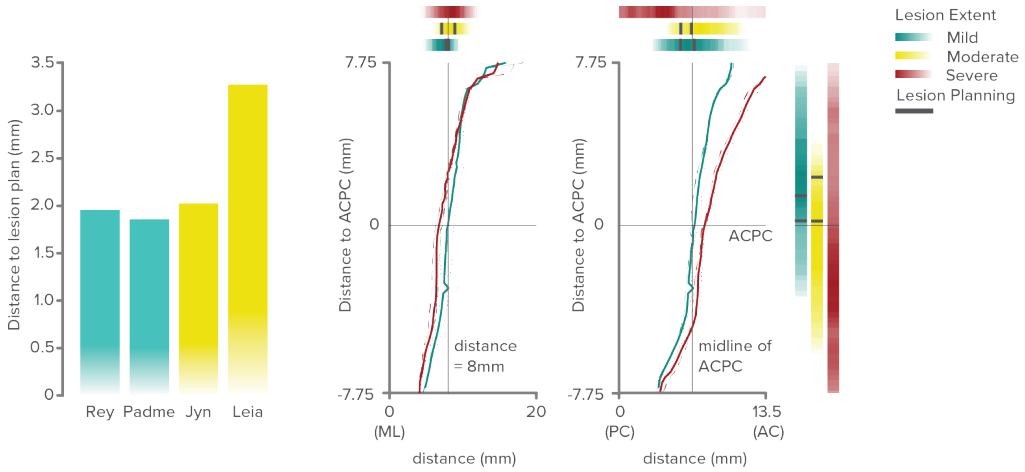

Figure 2.8: Normalized lesion position (A,B) The histologically estimated lesions, MRI lesion planning and the traced tracts in healthy animals ($n = 2$, M1 and PMv) were registered to an atlas space (chapter 2.2.13, MNI *M. fascicularis* atlas (Frey et al., 2011)), MRI planning was only performed in the mild and moderate groups (A) Distances between the MRI planning and the centroid of the administered lesions in each respective animal. A mean accuracy from planning to execution of $2.3 \pm 0.6mm$ (B) Depiction of the corticospinal mean and standard deviation traces of M1 (green) and PMv (red) through the internal capsule on the coronal and sagittal projections in atlas space. The derived optimized lesion location is depicted by the gray cross. The lesion extents by group are depicted by the adjacent color gradients with the lesion planning depicted in gray.

2.4 Discussion

In this chapter a novel approach of producing a focal infarct targeting the internal capsule was described. The approach enables the precise targeting of specific neuronal tracts in the internal capsule, while sparing critical cortical areas. Following, the validation of the lesion planning and the resulting lesion precision, are discussed.

2.4.1 Stereotactic approach and planning

The size and shape of a monkeys' brains can vary quite extensively, especially when compared to other animal models such as rodents. The targeting of brain structures, especially of deeper structures, can pose a great challenge, as the reliance on stereotactic coordinates stemming from previous experiments leads to highly variable results. In order to precisely target these structures, researchers have thus relied heavily on muscle or neuronal feedback to guide their intervention during the surgery (Bootin, 2006; Miocinovic et al., 2007; Emborg et al., 2010; Nikolov et al., 2022). In recent years, MRI and X-ray guided approaches have improved on these circumstances, paving the way to more personalized guidance during surgery (Miocinovic et al., 2007; Emborg et al., 2010). However, many of these approaches require either the presence of these acquisition techniques in the surgical theater, or the ability to adapt the interventions to be compatible with the acquisition facility, such as the exclusive usage of MRI compatible material, in the case of MRI guided surgeries. To solve some of these issues a personalized, MRI guided surgical approach was proposed, splitting the MRI acquisition and the surgical intervention into two episodes, while ensuring a highly reproducible position of the subject during both procedures.

Traditionally, during surgical interventions in NHPs, the head is positioned by a combination of mouth-, ear- and orbital-bars; however, the positioning, especially of the pith, can produce inconsistencies (Miocinovic et al., 2007; Ose et al., 2022). To allow the structural MRI used to plan the focal lesion in the internal capsule and the surgical intervention to take place in different locations and on separate days, a head retention approach based on a novel maxillary mold, in combination with a MRI compatible stereotactic frame, was chosen. The maxillary mold was fabricated from each animals' imprint and fixed for each individual before the acquisition of the MRI used for surgical planning, precisely fixating the animals' head position in all 3 axis. Each animals' variation of landmarks between multiple MRI acquisitions

was measured and found to be below $0.5mm$ on average, which was not the case in the same type of acquisition with the traditional mouth-bar or a recently introduced head-mount based system, noting errors above $1mm$ between stereotactic placements (Emborg et al., 2010; Ose et al., 2022). The use of a maxillary mold, therefore, seems to be a very viable option to ensure constant positioning of the subjects between surgeries, especially in the case of multiple, spaced interventions.

For recovery studies, it is of the utmost importance that areas, which are believed to have a major involvement in the recovery process be kept intact. However, stereotactic interventions are traditionally performed with a strictly dorso-ventral trajectory, as this reduces angular uncertainty and user error. In the case of an internal capsule lesion, this approach would pass straight through the ipsi-lesional motor area. This would have posed a two-fold problem: 1) the motor areas this this study intends to investigate would be majorly affected, and 2) inter-cortical neuronal measurements would be jeopardized, as the descending lesioning electrode would pass close by, potentially dislodging or damaging these devices. In order to remedy this, a personalized electrode insertion path was planned using the acquired structural MRIs, evading the motor cortices all together at an insertion angle of around 60° from the axial plane.

Together, the improved head retention system and personalized lesion planning system form a stable base for precise and repeatable experiments, while further providing a flexibility in the timeline between acquisition of the planning data and the actual intervention. It also allows the placement of complex, non-MRI-compatible recording systems, such as intracortical arrays or EMG systems, to record baseline data in between acquisitions, without sacrificing surgical precision.

2.4.2 Lesion precision

The internal capsule is a comparatively narrow structure, situated deep in the brain. Targeting it specifically requires tools that induce narrow and precise lesions. The technique of radiofrequency thermocoagulation proved to provide these qualities, resulting in highly stable lesion sizes with the ability to enlarge the impact as needed by tuning the lesion induction parameters (Figure 2.6), while still staying within the confines of the internal capsule, minimizing the insult to surrounding structures to less than 25% of the total lesion volume. Previous studies applied various approaches to selectively lesion this structure (Lacquaniti et al., 1987; Puentes et al., 2015; Murata and Higo, 2016; Kim et al., 2021). However, in most cases

the induced lesion either substantially damaged the surrounding tissue, or proved to be relatively variable in their location and extent. One notable difference is the very recent publication of Kim et al. (2021)), describing internal capsule specific lesions in 70% of their cohort. However, due to the employed lesioning technique (Chapter 1.2.5) an approach passing straight through the motor cortex itself was required to achieve this.

2.4.3 Histological registration and relative lesion location

While the histological analysis of the lesion and the surrounding structures provides some insight into the individual animal's lesion location, the comparison to the original MRI planning is difficult. Furthermore, quantifying the relative positions of the lesions in the brain poses a challenge. To bridge the gap between histological precision and the comparability of MRI scans, a unified atlas with histological data registered to MRI space has been published in rodents and squirrel monkeys (Meyer et al., 2006; Xiong et al., 2018; Schilling et al., 2019). However, no applicable framework for macaque monkeys could be found. Thus, during this study, a pipeline to register partial histological slices to a *M. fascicularis* atlas was developed. The goal of this procedure was the alignment of the histological slices to a unified atlas space. As the anatomical differences in NHPs can be substantial, this was achieved by first aligning the histological slices to the individual in-vivo and post-mortem MRI scans, before they were then registered to the MNI atlas space (Frey et al., 2011). The developed pipeline allows for the automatic construction of a histological volume, and the subsequent registration to the mentioned MRI spaces, with the ability for the user to tweak some quality control and optimization factors. This technique allows the migration of histological markers and stainings (Chapter 4.3.3) to MRI space. This can be achieved with partial and damaged (lesion etc.) histological slices, making it a versatile tool for NHP research.

The registered volumes allowed for the unified quantification of the lesion location and the precision of its administration. In the four animals where an MRI planning was undertaken (Mks Pa, Re, Jy, Le) a relatively low error could be reported (Figure 2.8, which is substantially smaller than the estimated lesion variance in comparable models (Murata and Higo, 2016; Kim et al., 2021). Nevertheless, an error of around $2mm$ on average remains, even after the improvements to head stability and MRI planning. There are two main culprits that may be responsible: the insertion angle and the electrode stability. The estimated error in insertion angle (Chapter 2.3.3) was around $3°$, which may stem from multiple sources or a combina-

tion thereof: user error in setting the right angle on the stereotactic frame, the frame's stability, an angle deviation of the stereotactic tower, a miss-alignment of the animals position, or a registration error. As the deviation seemed to be a systematic one, subject specific or user errors seem to play a less important role. Unfortunately, an error of a few degrees, caused by frame or tower deviations, is hard to determine and fix by eye. A solution could be a system in the surgical theater that monitors the electrodes' position (Discussed in chapter 2.5). A possible error due to electrode instability might be harder to combat. As the path of approach to the lesion target is oblique and possibly close to internal sulci, this could have induced bending of the electrode while descending to the deeper structures. Such an error would be only detectable with secondary non-invasive imaging, such as an X-ray acquisition during the surgical intervention.

The alignment with the reference MRI further paved the way for a comparison between descending tracts to the functional outcomes (Figure 2.8, Chapters 4.3.3 and 3). The lesions with a lower functional impact tended to be more superior to other lesions, interrupting the CST at a more dorsal location, where the CST is still further spread, and thus potentially interrupting a smaller percentage of the descending tract, despite having the same lesion volume. This provides evidence, that the location of the lesion in the internal capsule plays a major role of post-lesional outcomes, in comparison with lesion volume alone, further outlining the need for the analysis on the basis of a unified atlas.

2.5 Limitations

While the maxillary mold fixation system provides the flexibility of delaying the lesion induction by several months after acquisition of the MRI for surgery planning, it still poses constraints on the experimental planning: a limited time between planning and lesion induction, as well as well as the limitation on implants before the planning session.

The maxillary mold seems to have a limited lifetime, especially in the case of young animals. As in one of the subjects (Mk-Pa) a change in teeth alignment was observed, rendering the previously fabricated maxillary mold unusable. It is thus advisable to perform the mold acquisition and planning, as close to the lesion intervention as the experimental protocol allows.

A further limiting factor for the experimental planning, is the reliance on an MRI acquisition for the surgical planning. This severely limits the recording or restraining devices that can be implanted before the planning session,

as they must be MRI compatible. Even with MRI certified devices, possible artifacts produced by such implants might distort the MRI, creating imaging artifacts and thus reducing the accuracy of further experiments.

2.6 Future perspectives

2.6.1 Maxillary retention system

While relatively small, the measured error of the lesion administration could still be further improved (Chapter 2.4.3). While not yet in use during the presented study, the group has been experimenting with real-time positional tracking of the position of the subjects and tools in the surgical theater, provided by Brainsight (Cephalon, Denmark). Preliminary results show that it is possible to have sub-millimeter resolution in tracking of markers within the surgical theater. If implemented correctly, this could provide angular and positional measurements, possibly detecting and minimizing errors in electrode positioning and systematic deviations stemming from the stereotactic frame or the tower. It could further provide pivotal visual feedback to the surgeons, in case of ad hoc changes to interventions.

2.6.2 Standardized surgical planning

As part of this study, the surgical planning was done by referencing the planning MRI alone, with an expert determining the optimal lesion position according to literature and empirical knowledge from previous experiments (Morecraft et al., 2002). However, with the developed registration pipeline it is possible to define an optimal lesion location in the atlas space and register this to the individual animals MRI instead, standardizing the surgical planning. In a further step, a program calculating the expected fiber loss according to the control animals descending tract locations would allow the prediction of the expected loss of fibers from each descending tract (M1, PMv, PMd etc.). Combining this with the standardized lesion planning, this could lead to even more specificity in the induction of deficits stemming from a known loss of fibers.

2.6.3 Applicability of lesion framework to other NHP models

Precise access to deep brain structures is pivotal in many research fields. It is necessary for implanting a deep brain stimulation lead, inserting an

electrode array for neuronal recording, or, as in the case of this study, the induction of a lesion. In cases when surgical guidance methods are limited by pre-existing implants or other conditions prohibiting the use of intraoperative imaging techniques, stereotactic approaches are paramount. During these procedures the precise positioning of the subject provides the basis for a successful intervention. The flexibility gained by MRI guided planning, in combination with the repeatability of placement provided by the maxillary retention system makes this combination a promising candidate for such applications. The system introduces the potential of combining complex systems, such as those used for permanent intracortical or muscular recordings, while providing a time window for such interrogations between surgical planning and a subsequent, high-precision intervention.

2.7 Conclusion

In summary, the described lesion induction framework provides a highly reliable platform to study the effects of subcortical stroke, allowing for the implementation of complex, longitudinal studies, owing to the implementation of a robust head-restriction mechanism and the avoidance of all motor areas during the surgical approach. Besides the study of the present paradigm, the technique is readily adaptable to study various effects of lesions situated in the deep brain in non-human primates, paving the way for a variety of basic and applied investigations of sensorimotor processes.

Chapter 3

Strategic changes in motor tasks following subcortical stroke

3.1 Introduction

Loss of control of the upper-limb is seen in 80% of people suffering from a stroke (Gresham et al., 1997; Langhorne et al., 2009). After such an incident, rehabilitative training is administered as soon as possible, in an attempt to harness the brains' plastic phase (Ward, 2017). Despite these efforts, 65% of patients remain impaired in their upper-limb function, often preventing them from performing independently in their daily lives (Buma et al., 2013; Winstein and Kay, 2015; Winstein et al., 2016). Today's rehabilitative paradigms focus on task specific training, hoping to improve the general function of the motor system in conjunction with the remaining cortical circuits (Zeiler and Krakauer, 2013). Even though improvements are made during the rehabilitative sessions, patients often have difficulties transferring these skills into everyday circumstances (Plautz et al., 2000; Winstein et al., 2016).

Facing these discrepancies between desired and achieved outcomes, a debate on 'real' recovery vs compensation has ensued (Nakayma et al., 1994; Roby-Brami et al., 2003; Levin et al., 2009; Darling et al., 2011; Krakauer and Carmichael, 2017). Proponents argue that current recovery assessment

tools, while quantifying the patient's ability to perform specific tasks, do not adequately measure the underlying kinematic changes. The reported improvements would thus be compensatory, learned strategies, coping with the residual motor control, rather than actual gains in the patient's kinematic ability. It thus remains unclear how much of the reported functional improvements are masked compensatory strategies (Levin et al., 2009).

In this study, the aim was the quantification of the functional and kinematic deficit seen after the induction of a clinically relevant subcortical stroke. Aided by 3D kinematic assessment during the performance of six motor tasks, in combination with the quantification of the functional success of the subjects, the recovery process after stroke was investigated. With tasks ranging from the assessment of residual functional strength to the analysis of fine-motor control of the hand, a solid platform for the evaluation of the discrepancy between functional recovery and the underlying kinematic ability recovered after a subcortical stroke was built.

3.2 Methods

3.2.1 Animal model

The animals included in this study as well as their housing situation are described in chapter 4.2.1.

3.2.2 Experimental timeline

In order to study the effects of a subcortical stroke on the functional and kinematic recovery in non-human primates (NHP), an experimental timeline was devised to include a behavioral investigation, as well as concurrent recording of cortical and muscular signals, and concluding with a histological investigation. Each animal underwent a similar experimental timeline: acclimatization and training of the behavioral tasks, implantation of cortical and muscular recording devices, intact baseline recordings, stroke administration, and eventually the recording of the behavioral performance during the recovery phase, lasting up to 6 months. After the conclusion of the experimental paradigm, the implanted cortical arrays were extracted before the tracer injection. After an adequate delay for tracer expression, the animals were euthanized and histologically processed (Chapters 3 and 2).

3.2.3 Recording setup

In order to monitor the animals' upper-limb grasping performance, both in the healthy condition as well as post-lesion, we needed a platform that allowed for 1) quick switching between tasks with the monkey present, 2) easy access to the animal and the measuring devices by the researcher and 3) precise and stable measurements in lightly restrained animals in both healthy and lesioned conditions.

During recording sessions, two researchers needed to be present. The first remained inside with the monkey, managing the task and connection to the system. The second, oversaw the recording, data quality, and synchronization.

Primate chair

The animals were restrained in a primate chair, centrally placed within the recording room. The chair was built to allow easy transfer from the mobile primate chair (Chapter 3.2.4), and provided restraints for the neck and the right (unused) wrist. These limited restraints left the animal free to move their left arm and head, while keeping the animal from turning or from completing the task with the untested, intact limb. To ensure that the animal was able to sit comfortably, the seat height, as well as the collar-size, were adjustable.

The chair included multiple and varied attachment positions to allow for a stable connection to multiple motor tasks: the modified Brinkman board (Rouiller et al., 1998), the Box and Blocks task, and the object presentation task (Chapter 3.2.4). The modular nature allows switching between tasks in less than a minute, with the monkey present and still connected to the various recording modalities.

Multimodal recording system

To monitor the animals' upper-limb motor function pre- and post-lesion, we employed multiple, synchronized data acquisition modalities: 3D pose-estimation, intra-cortical neuronal recordings, electromyography, and pull force.

3D pose-estimation The marker-based 3D pose estimation system (Vicon Motion Systems, UK), was installed on rails surrounding the primate chair. 12 infra-red cameras (Vero v2.2) as well as 2 visual cameras (Vue) were employed for recording. The system allowed sub-millimeter tracking

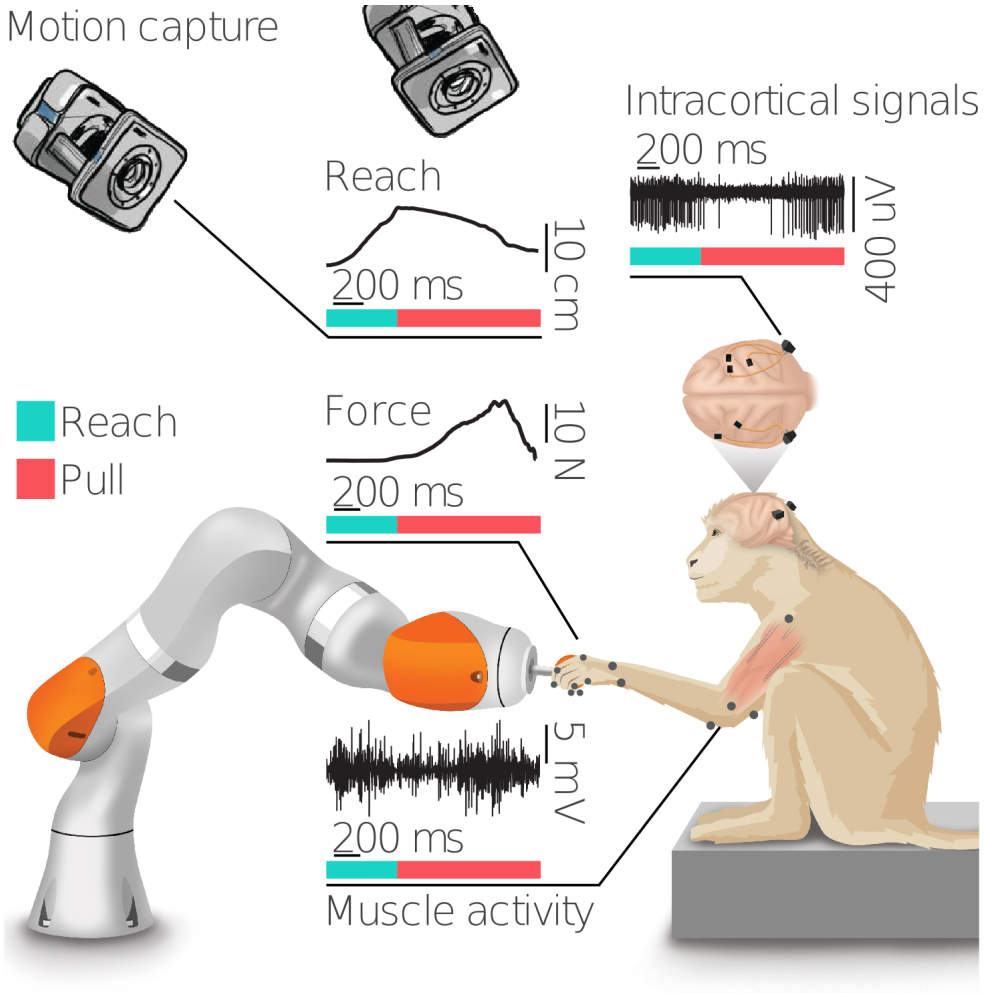

Figure 3.1: Recording set up A schematic depiction of the employed recording setup and its capabilities. The structure allows recording of 3D kinematic data with a marker based motion capture system, the capturing of multi-channel recording of the cortical activity during training sessions, as well as electromyographic recordings of the upper-limb. These readouts were used in combination of an array of tasks for the precise kinematic assessment of the remaining movement quality after subcortical stroke. Here the interaction of a subject with the robotic object presentation platform is shown, providing feedback of the applied forces. Figure adapted from (Barra et al., 2021).

of multiple reflective markers at a polling rate of 100Hz. To achieve the best tracking fidelity, the system was calibrated to the animals' torsos and left upper arms only. During recording sessions, up to 14 markers (∅4-8mm) were tracked and placed on the upper arm (3 markers: shoulder, middle of humerus, elbow) and a personalized primate glove (11 markers). The primate glove was fitted to the hand of each subject, and markers were fixed at the following positions: radioulnar and radiocarpal joints, metacarpophalangeal and (proximal-)interphalangeal joints, as well as the fingertips of the thumb, index, and pinkie. The marker positions were estimated using a subject specific model, calibrated with Vicon's Nexus software.

Intra-cortical recordings The animals' brain activity was monitored using intra-cortical recordings via micro-electrode arrays (UTAH array, Blackrock Neurotech, USA). Each animal was implanted with multiple arrays, totaling 256 concurrent recording channels. The signal was sampled at 30kHz, using Blackrock's Cereplex-E headstages. This neural signal was accessed over a wired system, suspended via rails above the subjects' heads, relieving tension from the monkeys' heads as well as the recording system itself.

Electromyographic recordings In Mk-Le and Mk-Pa, additional recordings of the muscle activity before and after the recovery were performed. A list of the implanted muscles can be found in the appendix table 6. The fully implantable electromyographic system (Ripple Neuro, USA) was accessed wirelessly, through a Grapevine receiver posed over the implanted signal processor, and transmitted to the Trellis software.

Pull force In the object-presentation task (Chapter 3.2.4), the force applied during the grasping and pulling phase of the animal was recorded by a robotic arm system (KUKA Robotics, Germany). The robot arm was placed in front of the animal. The system allowed the researcher to lower the robotic arm into the task space and provided a measurement of the applied forces in 3D space.

3.2.4 Tasks

General training

In order to achieve long-term, high-quality readouts, especially after implantation and lesioning, the monkeys must willingly participate in the tasks, with their stress level kept to an absolute minimum.

After arrival in the facility, the animals were left to acclimate to their new housing room for two weeks. Over the following days and weeks, a researcher entered the facility with some of their favorite food and spent time with them in order to slowly normalize the presence of humans. When the animals started to willingly approach the researcher, the second phase was initiated. Before training, the animals were herded into a large housing cage, and a small cage was attached to its door. With sufficient food and time, the monkeys slowly associated the small cage with food rewards, and would willingly enter it individually, without fear of the grate closing between the cages. At this stage, the primate chair was introduced. The chair is designed to accommodate a single animal, and restrain it around the neck, prohibiting retraction of the head as well as escape. The chair (open back, head closed) was connected to the small cage through a transfer-tunnel. As with the small cage, the animal was slowly introduced to the chair. With time, the portion for the head was opened enough to allow the monkeys to pass their head through. With plenty of food rewards, they were trained to keep their heads outside to receive food reward, and after some weeks the animals tolerated the closing of the neck-restraint. With the back of the primate chair closed as well, the animals could now be safely transported from the housing facility to the experimental room. They were then introduced to the experimental setup and were able to be easily handled for any necessary care-taking and inspections.

Modified Brinkman board

The modified Brinkman board task is a measure of fine manual dexterity (Rouiller et al., 1998). It consists of a board with oblong slots oriented both vertically and horizontally. The slots are sized to allow the animal to insert only two fingers in an opposed grip (7mm x 14mm). A single sucrose pellet (45mg, Dustless Precision Pellets®, Bio-Serv, USA) was placed in each slot before the board was fixed to the primate chair in front of the animal. During this task, the animal's ability to successfully grasp and feed the pellets to themselves was assessed. As the task was relatively straight forward, only very limited training was needed. The training mainly consisted of exposure to the task itself as well as keeping the animal from engaging with the task before the board was fixed into place. For this task no markers were placed on the subjects, as any attempts to do so would result in the markers being swiftly removed and eaten (Figure 3.2a).

One recording day consisted of 2-5 sessions, in which the animals were presented with one full board. The session ended when all pellets were

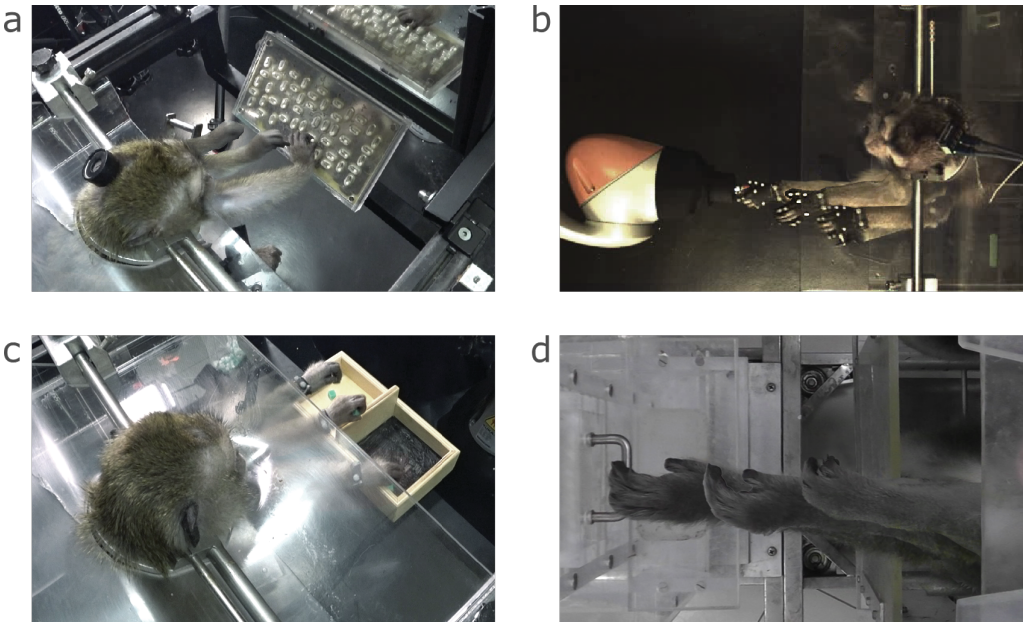

Figure 3.2: Kinematic assessment tasks Exemplary depictions of the execution of the employed tasks. (a) Reach and grasp movement to retrieve a food pellet from the modified Brinkman board. (b) Reach and grasping of the spherical object during the robotic object presentation task. The precision and cylindrical grip objects are not shown. (c) Pick-up and passing of a block (green) in de adapted Box and Blocks test. (d) Reach and grasp for the cylindrical grip during the Drawer test.

cleared from the board, or after 5 minutes had passed.

Robotic object presentation

The robotic object presentation system was developed in house, and is a modular object presentation system suited to assess non-restricted and targeted reach-and-grasp movements in 3D space (Barra et al., 2019). The system is based on an industrial robotic arm (IIWA, KUKA, Germany), fitted to present various grasping objects to the subject. For our assessment, we used four objects of different shapes and sizes: a small sphere (⌀15 mm), a large sphere (⌀30 mm), a cylinder (⌀15 mm, length: 80 mm), and a flat, triangular object (base: 20 mm, height: 15 mm, thickness: 5 mm). Whereas the spherical and cylindrical objects prompted a spherical and cylindrical grip respectively, the triangular grip required a lateral precision grip to be successfully grasped. The objects were presented at a set position in space and were to be pulled 6 cm (spheres/cylinders) or 2 cm (triangle) towards the subject in the primate chair. The system further enabled the researcher to set various pulling resistances and to monitor the applied forces in 3D

space.

The animals were introduced to one object at a time. They were trained to place their hand on the primate chair's resting bar. On the go-cue (sound and light) the previously blocked robot switched to interaction mode and the monkey was able to grasp and pull the presented object towards them. Upon completion of a successful trial, a small food reward was given (Figure 3.2b).

During training and recording sessions, the subject's upper arm was fitted with reflective markers, and a primate glove was worn to allow for kinematic tracking. The recording day consisted of 15 to 20 sessions, consisting of 10 to 20 pull attempts each, in the healthy condition. Each recording day the animals were presented with up to 3 objects or pull resistances, resulting in around 50 to 100 trials per condition per day.

Adapted Box and Blocks task

The Box and Blocks task is routinely used as an assessment of unilateral gross manual dexterity in human stroke patients(Kontson et al., 2017; Hebert et al., 2014). It consists of two adjacent boxes, separated by a dividing wall. One of the boxes is filled with small cubes. The subject's task is to pass single cubes from one box into the other, doing so as fast as possible (Mathiowetz et al., 1985). This task was adopted to fit the requirements of monkey research. To better fit monkey hands, both the boxes and blocks were scaled down by a factor of 3. This yielded two wooden square boxes (85mm) divided by a wall with a height of 50 mm. For the blocks, 8 mm plastic cubes were used. The boxes were attached to the experimental primate chair in front of the monkey, allowing recordings with up to three modalities (Chapter 3.2.3). A major alteration required due to the language barrier between the researchers and subjects, was the number of cubes simultaneously presented: only one cube was presented in the starting box, and subsequent cubes were only added once the previous cube was transferred (Figure 3.2c).

The task was introduced after the general training (Chapter 3.2.4). During the task, the subjects sat in the primate chair (Chapter 3.2.3) with their right arm restrained. To train the monkeys in the task, single cubes were presented in the researcher's hand. The animals' natural curiosity prompted them to grab it immediately. Reward was given when the block was dropped into either side of the box. After the monkey understood the concept of dropping the cube, reward was given only when the cube was released into the right box. Finally, the cubes were placed into the left (start) box.

The number of repeated transfers needed to receive a food reward was then continually increased until the subjects reached roughly 1 minute of consecutive passes.

For kinematic recordings the subjects were fitted with the usual three arm markers in combination with a two-marker wristband.

Drawer task

As a gross motor assessment for reach-and-grasp capability, a new 'Drawer task' was developed. The animals were to reach for and grasp a drawer that could be equipped with different handles/objects. On a successful pull, the drawer automatically released a food reward. The task was deployed in the lab of our Chinese collaborators (Motac Neuroscience, Beijing China). Its design had thus an additional focus on reliability, ease of use and deployment, as well as repairability. We manufactured multiple drawer insets with different pulling objects. They could easily be exchanged in a matter of seconds, thus allowing the testing of multiple objects during one recording session. We utilized five objects: a sphere (∅25 mm), both cylindrical handles (∅5 mm), and plates (thickness: 5 mm) attached vertically and horizontally. They were inserted into a Plexiglas®tower fitted with a food retention tray, into which the food reward was released. The pull resistance was regulated with exchangeable springs, connecting the tower and drawer-insets. The whole system was constructed from 1cm thick, clear acrylic glass and rooted on a rectangular base that could be attached to a movable trolley available on site (Figure 3.2d).

During recording sessions, the drawer was positioned in front of the animals, which were seated in a mobile primate chair. The animals were trained by the local team of researchers and veterinarians. Training involved exposing the animals to the task, and getting them to pull the handles until they associated the drawer pulls with food reward. For recording sessions the animals' digits and arm were painted with white on black markers (nail-polish) and recorded with a marker-based motion tracking system (SIMI Reality Motion Systems, Germany).

3.2.5 Kinematic analysis

Adapted Box and Blocks task

The adapted BBT performance analysis was based on the marker-based 3D-pose estimation files recorded with the Vicon system (Methods 3.2.4). The captured marker data and joint assignments were manually validated,

and incorrectly assigned markers were corrected using the Vicon Nexus software (Vicon Motion Systems, UK). For quality testing purposes, the relevant events were marked: start reach, start grasp, end grasp, fail, and success. The marker and event data were then exported in .c3d format for further analysis in Matlab (version: 2019b, Matlab, USA) and Python.

A custom script was developed for semi-automatic extraction of relevant trial events: start and stop of a trial, passage of the divider, and pass quality. The calibrated Cartesian marker coordinates were used to set thresholds in space corresponding to the location of the testing apparatus. The box pickup and drop-off events were estimated using a combination of indicative movement patterns, such as maximal wrist extensions before a barrier pass. These events were then manually validated and used for trial segmentation.

From the extracted Cartesian positions a range of features were calculated: sub task durations, grasping trajectory length and speed, as well as the angles of the shoulder abduction, elbow-flexion and wrist pronation/supination, and their respective range of motions (Table appendix 2). A principal component analysis (PCA) was performed on the extracted features of all subjects and time points, resulting in one combined principal component (PC) space. The two PCs accounting for the largest variance were used for the further analysis. The recording days were then binned into four time-frames: intact (days up to lesion), acute (days 1-30 post lesion), late acute (days 31-90 post lesion) and chronic (day 91 post lesion and after). For each animal, the euclidean distance of all trials, compared to the centroid of the intact performance was calculated, to gain a general kinematic recovery measure. The PCs individual contributions and their loading factors were extracted (Courtine et al., 2009; Barra et al., 2019).

Robotic object presentation

The robotic object presentation performance analysis was based on the marker based 3D-pose estimation files recorded with the Vicon system (Methods 3.2.3). The captured marker data and joint assignments were manually validated and incorrectly assigned markers were corrected using the Vicon Nexus software (Vicon Motion Systems, UK). Relevant events were manually marked: start reach, start grasp, end pull, fail and success. The marker, event and robot data was then exported in .c3d format for further analysis in Matlab (version: 2019b, Matlab, USA) and Python.

An automatic trial identification and event detection script was implemented to aid in data segmentation. Using the location of physical objects such as the resting bar, we defined thresholds to identify movement initia-

tion and trial end. The begin and end of the grasping phase were defined by identification of movement patterns, such as the maximal arm extension. The extracted events were manually verified and further used for trial segmentation and binning.

The absolute Cartesian marker positions were converted to their corresponding joint angles and relative distances between joints. 13 angles were extracted: metacarpophalangeal flexion for the thumb, index and pinkie, thumb interphalangeal flexion, pinkie and index proximal interphalangeal flexion, wrist ulnar deviation and flexion, thumb palmar and radial abduction, index and pinkie abduction and elbow flexion, as well as shoulder abduction. From the resulting angle trajectories, further features such as angular velocity, acceleration, and jerk features, were extracted. From these dynamic features a range of static features were computed: range of motion, swiped area, maximal and mean velocities, as well as trial duration (Table appendix 3). For each object, a separate PCA was performed on the extracted static features on all subjects and recorded time points, resulting in three separate PC spaces, one for each object: triangle, sphere and cylinder. The two PCs accounting for the highest variance were considered for the further analysis. The recording days were then binned into four time-frames: intact (days up to lesion), acute (days 1-30 post lesion), late acute (days 31-90 post lesion) and chronic (day 91 post lesion and after). In each objects' PC space, the individual animal's euclidean distance of all trials, compared to the centroid of the intact performance was calculated. The PCs individual contributions and their loading factors were extracted.

Modified Brinkman board

The modified Brinkman board (mBB) was assessed in both the local Fribourg laboratory (FL) and the collaborative facility (ML) in Beijing. At FL the trials were recorded with a synchronized two camera system in addition to the Vicon system (Methods 3.2.3), whereas at ML, the recording was done with a SIMI system (Simi Reality Motion Systems, Germany) as well as a camcorder (Sony, Japan). The grasping performance was assessed using a video player (VideoLan, 2006), recorded in Excel (Office suit, Microsoft, USA) or the SIMI systems proprietary software. The subsequent analysis was performed in Python. To assess the performance in the mBB, two key measures were used: success rate and grasps per minute. A three-point success measure was used: 'success': the monkey successfully grasped the pellet and fed themselves; 'fail': the pellet was removed from the slot but could not be eaten; 'next': the monkey attempted to remove a pellet

from a slot but then moved on to another slot. The time was recorded from the first touch of the board until the last pellet was removed. In the case of inactivity, the timer was stopped after 5 seconds and resumed on the next grasping attempt. The resulting success rates were then binned into four time frames: intact (days up to lesion), acute (days 1-30 post lesion), late acute (days 31-90 post lesion) and chronic (day 91 post lesion and after) and statistical analysis was performed (Methods 3.2.6).

Drawer task and flexor synergies

The trials of the drawer task were performed at Motac (ML), the collaborative facility in Beijing. The recordings were performed using the local SIMI system (Simi Reality Motion Systems, Germany) as well as a camcorder (Sony, Japan), and the data analysis was done using the Python environment. The performance pre and post lesion was assessed using two measures: success rate and grasps per minute. The success rate was defined with a three point rating system: 'success': the monkey successfully pulled the drawer and retrieved the food; 'pull': the monkey successfully pulled the drawer but did not manage to feed themselves; 'fail': the monkey attempted to pull the drawer but could not trigger food release. The time was counted during active reaching phases, defined as the first move reaching for the drawer until the last pull attempt. In case of inactivity between pulls, the timer was stopped after 5 seconds and resumed on the next pull attempt.

To assess the 3D kinematic, the arm joints were marked with black and white nail polish: shoulder, elbow, as well as the radial and ulnar wrist joints. The interpolated 3D positions of each joint were then extracted with SIMI's software. The range of motion of the elbow was extracted from the resulting elbow angle.

The resulting performance and range of motion data was then binned into four time frames: intact (days up to lesion), acute (days 1-30 post lesion), late acute (days 31-90 post lesion) and chronic (day 91 post lesion and after) and statistical analysis was performed 3.2.6.

3.2.6 Statistics

All data was reported as $mean \pm SD$. Significance calculations were performed using Wilcoxon rank-sum tests followed by post-hoc correction for multiple comparisons.

3.3 Results

3.3.1 Development of two novel upper-limb assessments in non-human primates

The lesion model for subcortical stroke devised for this study has little precedent in previous studies. As such, in the beginning of the study, the amount of motor impact to be expected from the administered lesion was uncertain. In the study facility, two upper-limb motor assessments had been well established before the start of this study: the modified Brinkmann (mBB) board as well as the robotic object-presentation (ROP). While the mBB provides a sensitive readout for dexterous digit control, the ROP provided a wide array of assessment possibility spanning from fine digit control to a gross movement reach-and-grasp task. However, for the ROP task, a residual amount of force is key to the successful completion of the trials. A task assessing the general ability of hand closing and opening, not requiring a large amount of force would therefore complete the assessment ensemble.

For the collaborative effort in China only the mBB paradigm has been previously established. Due to the comparative limited training time and control, as well as the local recording equipment limitations, a simple yet performant task approximating the capabilities of the highly advanced ROP task was needed.

Therefore, two new motor assessments were developed: the adapted BBT and the Drawer task. The BBT is an assessment routinely used in the evaluation of the upper-limb motor skills in human stroke patients. It is built up from two adjacent boxes, divided by a separation wall. One of the boxes is filled with small cubes, while the other is left empty. The patient's objective is to pass the cubes, one by one, from one box into the other. The speed and success rate during this task is then used to assess the general grasping ability, as well as coordination and range of motion of the patient. This task was chosen and adapted to fit the needs of non-human primates by down-scaling according to the smaller hand dimensions, as well as reducing the cube count in the start box to a single cube at the time (Figure 3.3), Methods 3.2.4). To be integrated into the existing recording system, the task was made to be mountable on the standardized experimental chair (Methods 3.2.3). The animals' learning time for this new task was around one month for subjects that had already undergone general acclimatization to the training room, and was therefore easy to integrate in the existing training schedule.

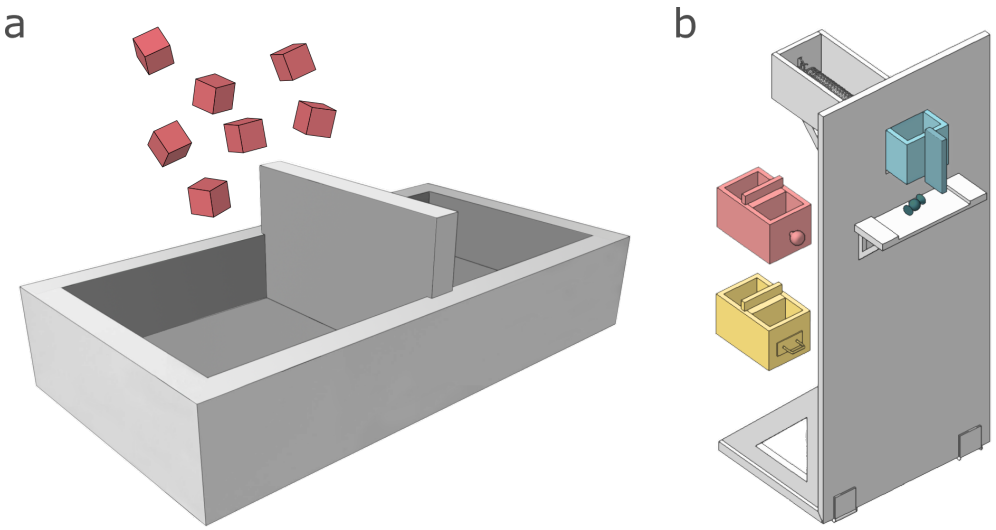

Figure 3.3: Two novel upper-limb motor function tasks Schematic depiction of two new tasks for the functional assessment of motor control: the adapted Box and Blocks test and the Drawer task. (a) The adapted Box and Blocks tasks was adapted from the human equivalent routinely applied in stroke assessments (Hebert et al., 2014). The task requires the reaching and grasping for cubes (red) placed into the left box, and subsequently passing them to the right, target box. The animal's ability to perform this task, as well as kinematic features, were used for its analysis. (b) The Drawer tasks is a reach-and-pull tasks, and allows the assessment of various levels of upper-limb dexterity and force. The system was equipped with multiple, exchangeable drawers, allowing the assessment of the precision grip (cyan), spherical grip (red), and power grip (yellow). After successful grasping and drawer pulling, a food reward (blue) is automatically dispensed. The Drawer task was developed as a low-tech equivalent of the robotic object presentation task, to be deployed and used at the collaborative laboratory Motac (Beijing, China).

For the device in the collaboration facility in China, the drawer task was devised. According to the local laboratory environment, a lightweight, low-tech drawer system with automatic reward distribution was devised (Figure 3.3). The system was built as a single drawer cabinet, with exchangeable pulling handles. The handles mirrored the objects presented with the ROP: a vertical plate forcing precision grip, a spherical handle for spherical grasping, and a horizontal cylinder to assess a power grip. The drawer was retained by an interchangeable spring, allowing the regulation of the pulling force required to complete the task. When the subject successfully pulled the drawer to the maximal extension, a food reward was automatically dispensed. The device was built from acrylic glass, and engineered to be easy to mount and dismount, as well as able to fit into a standard piece of luggage for transportation to the experimental site. The system was then mounted on a height adjustable table in front of the standardized primate

chair on site, and the kinematics were recorded with the local motion tracking system 3.2.3. In case of damage, each piece of the device was quickly replaceable, either locally or via shipment (Methods 3.2.4). As the task was very straight-forward to learn, as soon as the automatic reward system was understood, the training time for the local staff and the subjects was less than a week. Despite the precautions for repair ability, the device suffered no damage during the recording time.

3.3.2 Spontaneous functional recovery after subcortical stroke

Four young adult female *M. fascicularis* were trained to perform three upper-limb motor tasks: the modified Brinkman board, an adapted BBT, and an automated object-presentation task (Figure 3.2, Methods 3.2.4). The animals' performance and kinematics were recorded for several weeks before the lesion administration, as well as during the recovery period, ranging up to six months post lesion administration. During the recordings, the kinematics of the animals were monitored with a marker-based 3D recording system. Furthermore, neural (n=4) and muscular recordings (n=2) were employed to complement the monitoring of the lesion impact and the recovery process (Methods 3.2.3, data not shown). Post-lesion all animals showed a marked deficit in left upper-limb function. In the first few weeks Mk-Re and Mk-Pa (mild group, cyan) showed a fast recovery of basic motor function, whereas Mk-Le and Mk-Jy (moderate group, yellow) showed a long-lasting deficit in both basic and fine motor skills. Lastly, the severely impacted cohort (severe group, red; Mks 03, 05, 06 and 11) showed no discernible recovery despite intensive rehabilitative training.

Dexterous hand control

The modified Brinkman board (mBB), as well as the precision grip object in the RoP, required a precision grip as well as wrist supination to be successfully completed. While the mBB was employed in both facilities, the RoP task was only employed in the local Swiss laboratory, where Mks Re, Pa, Jy and Le were housed and trained.

To assess digital dexterity in the robotic object-presentation task, the subjects were tested with the pinch / precision grip object (Methods 3.2.5). The rate of successful trial completion was recorded. Only Mk-Re and Mk-Pa regained the ability to perform the task, reaching baseline performance after the first month of recovery. In contrast, the other two animals never

regained the ability to pull this object during the observed period, closely mirroring the observation with the Brinkman board (Figure 3.4 a). The observed recovery to intact performance was observed within the first 30 days in both recovering animals.

The mBB task was used as a functional measure of fine motor skill, in that it demanded a precision grip (finger opposition of thumb and index finger), as well as limited pro and supination in order to access the pellets in the vertically and horizontally arranged slots (Methods 3.2.4. Both the success rate and speed of execution were used to assess the animals pre- and post-lesion performance. Both Mk-Re and Mk-Pa fully recovered their success rate over the first month post lesion, whereas both Mk-Le and Mk-Jy showed no discernible recovery in their ability to perform the task over three months post injury. Notably, after 3 months Mk-Jy changed the grip pellet retrieval strategy and began to grip the pellet between the index and middle fingers, instead of the thumb, bringing the success rate up to around 10% of the original performance (Figure 3.4 b). As for the pellet retrieval speed, there was a marked difference between the two animals in the fast-recovering group. While Mk-Re showed a progressive increase in pellet retrieval speed up to the pre-lesion speed over two months, Mk-Pa only recovered up to half the initial speed and remained at this pace from that point on (Figure appendix 1).

General reach and grasp control

The spherical grip object in the RoP, as well as the adapted BBT, were utilized to assess the animals' general ability for targeted reaching and coordinated hand closing. In the spherical grip task, the subjects further required a residual amount of strength to perform the task. The mild lesion group (Mk-Re and Mk-Pa) showed a quick recovery to baseline performance in only the first week post lesion, while the other two subjects (Mk-Le and Mk-Jy) regained 80% success rate within the first 40 days post lesion, and further improved over the next 6 months (Figure 3.5 a).

The BBT requires both an adequately large range of motion of the arm as well as residual finger control to both successfully grasp and pass the presented cubes into the target box. Only three monkeys were trained on this task (Mk-Pa, Mk-Le, Mk-Jy), as it was introduced after Mk-Re had already undergone the lesioning procedure. As a measurement of the general functional ability to perform the task, the rate of successful passes was assessed. As in the case of the brinkman board, Mk-Pa reached the pre-lesion performance in this task during the first month of recovery. Both

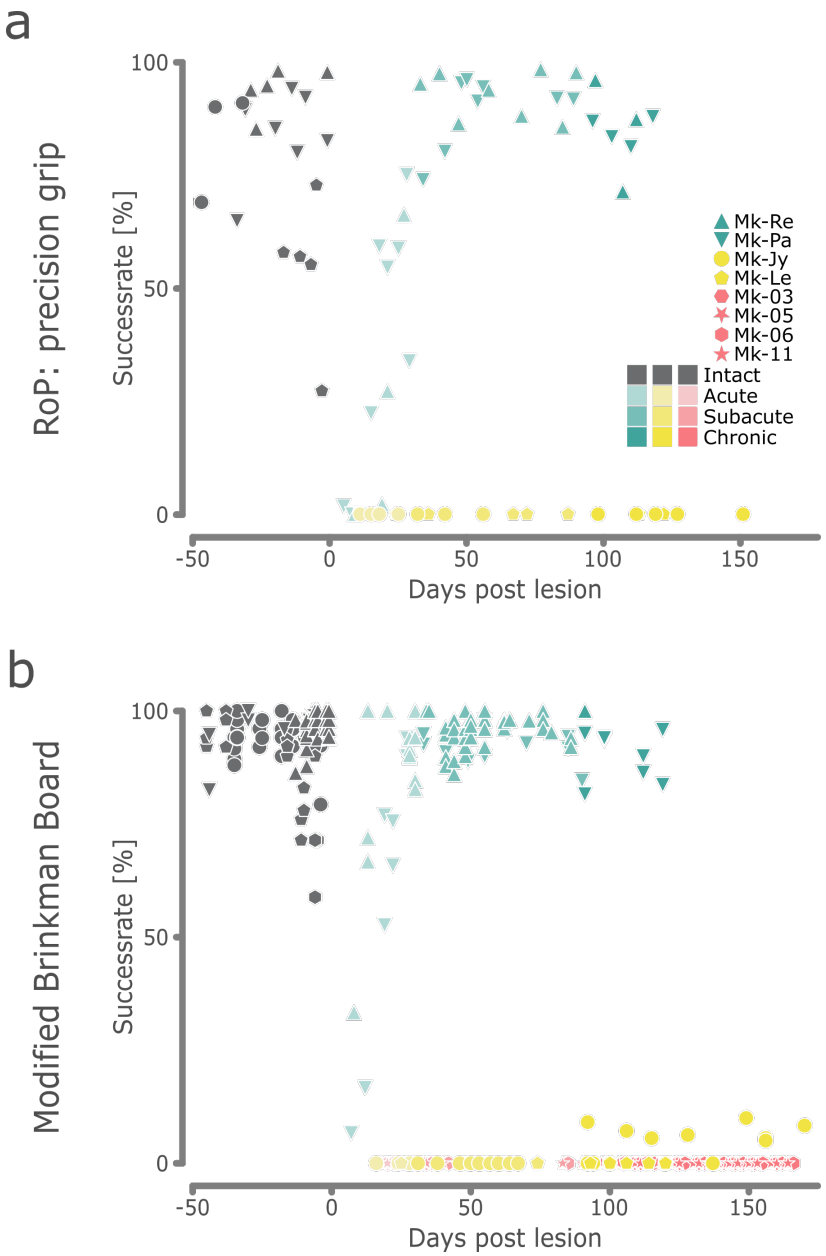

Figure 3.4: Functional recovery: dexterous upper-limb control A collective overview of the functional recovery in the modified Brinkman board task, as well as the robotic object presentation with the precision grip attachment. Both tasks require a precision grip, as well as wrist supination to be completed. (a) The rate of the successfully grasped and pulled pinch/precision-grip objects presented is displayed. (b) The modified Brinkman board's success-rate was defined by the amount of retrieved food rewards per total grasp attempts. Mks Re, Pa (cyan), Jy, and Le (yellow) were subjected to both tasks, whereas Mks 03, 05, 06 and 11 (red) were only assessed with the modified Brinkman board task. The intact performance is shown in gray, with acute (light), subacute (medium) and chronic (saturated) time points shown.

Mk-Le and Mk-Jy did not show any improvement over the first two months. After this time-point Mk-Jy, showed a remarkable recovery of the success-rate over another 2 months, finally reaching base-line level performance around four months post lesion. Mk-Le on the other hand, showed only marginal improvement in their ability to successfully pass the cubes, also after four months of recovery (Figure 3.5 b).

Retained functional force

In order to assess the retained functional force, as well as the presence of residual reaching skill, two cylindrical gripping tasks were employed. As the Drawer tasks aims to mimic the functional requirements of the ROP platform, it was used as an equivalent measure in the collaborative facility in Motac (Beijing, China). Both tasks presented the subjects with a cylindrical object to be grasped and pulled with a power grip. In the assessment of the ability to perform the task with the RoP task, Mk-Re and Mk-Pa showed a decline of less than 25% compared to intact performances during the respective first days of recording post lesion. The moderate animals, on the other hand, showed an inability to perform the task to a severe deficit ($< 40\%$ success-rate) in the first two weeks post lesion, followed by a rapid recovery to intact success-rates within the first month (Figure 3.6a). The subjects (Mks 03, 05, 06, 11) present at the collaborative facility Motac (Beijing, China) were recorded during the drawer task, and reached a pre-lesion success rate of $68.8 \pm 14.3\%$. Due to the very profound impact of the large lesions administered, none of the animals were able to perform a single pull of any object presented post lesion (Figure 3.6b).

3.3.3 Residual kinematic impairment after spontaneous functional recovery

Adapted box and blocks test

The BBT allowed recording of marker-based kinematics (Methods 3.2.3), paving the way for the kinematic assessment of the recovery process. From the kinematic recordings, the marker positions were extracted and the corresponding kinematic features were calculated: joint angles, velocity and ranges of motion, as well as the distance traveled and sub-trial duration (Methods 3.2.4). It should be noted that only the arm's kinematics could be recorded and individual finger movements were not taken into account.

In the monkeys that recovered the ability to perform the task at a pre-lesional performance, the movement patterns were investigated. A shift

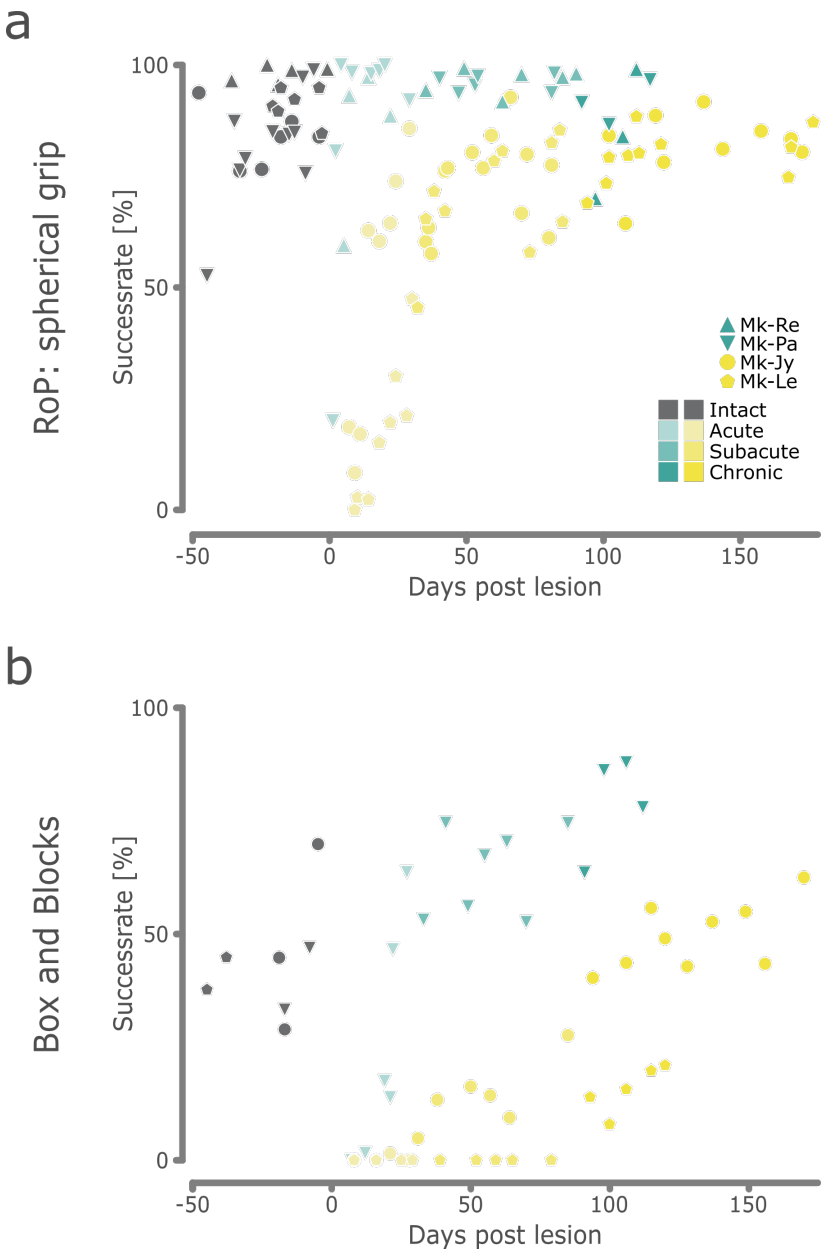

Figure 3.5: Functional recovery: general upper-limb control A collective overview of the functional recovery seen in the spherical grip robotic object presentation task, as well as the adapted Box and Blocks task. In order to be successfully completed, both tasks require residual reach-and-grasp control. The object presentation, further requires an adequate force output, whereas the adapted Box and Blocks test further prerequisites a larger available range of motion. (a) The rate of the successfully grasped and pulled sphere-objects presented is displayed. (b) During the Box and Blocks task the rate of successful pickups of the presented cubes, followed by dropping the cube into the target box was recorded. Mks Re, Pa (cyan), Jy, and Le (yellow) were subjected to the object presentation task. Only three subjects underwent testing in the Box and Blocks task as the new task was adopted after the lesion induction in Mk-Re. The intact performance is shown in grey, with acute (light), subacute (medium) and chronic (saturated) time points shown.

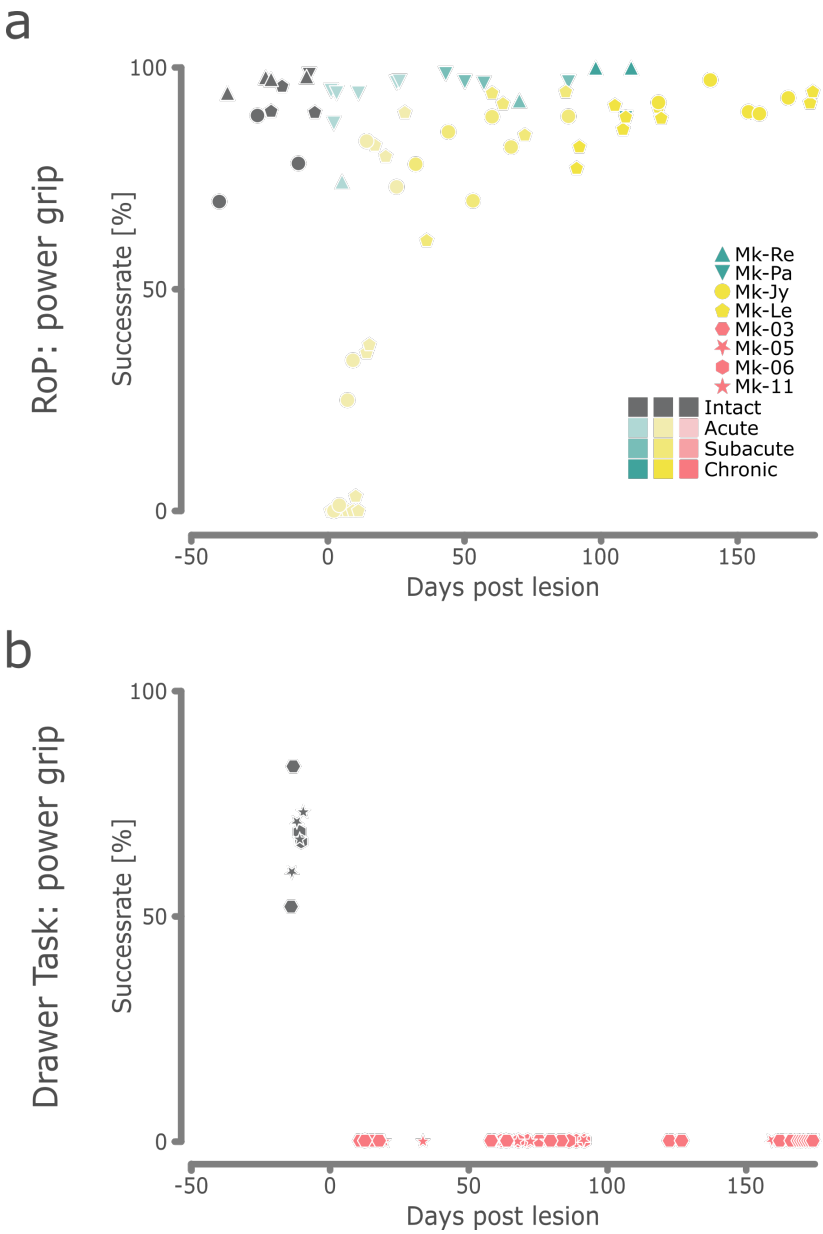

Figure 3.6: Functional recovery: retained functional force The functional force after subcortical stroke was assessed with two reach-and-grasp tasks: the robotic object presentation using the cylindrical object, as well as the Drawer task with the cylindrical grip. Both tasks required only a residual ability to reach, grasp and apply force during the pull to be completed. (a) The rate of successful pulls over the total amount of reaches is reported for the cylindrical power grip object. (b) The rate of successful pulls over the total amount of reaches is reported for the cylindrical power grip object. As the subjects were not able to perform full reach movements post lesion, attempted reaches were counted as failed attempts. Mks Re, Pa (cyan), Jy, and Le (yellow) were subjected to the object presentation task in Fribourg, whereas Mks 03, 05, 06 and 11 (red) were assessed with the cylindrical Drawer task. The intact performance is shown in gray, with acute (light), subacute (medium) and chronic (saturated) time points shown.

in movement patterns was visible in the acute phase (Figure 3.7a). Even though the ability to perform the task returned (Figure 3.5b), the movement patterns remained, in many aspects, similar to that observed in the acute phase (Figure 3.7b) This was especially true in the moderate deficit animal, Mk-Jy, in all three observed angles (elbow flexion, forearm supination, shoulder abduction) during the grasping, as well as the passing phase, where they showed significantly altered movement patterns ($p < 0.001$). However, also Mk-Pa, who recovered their ability to perform the task to pre-lesional levels within the first month of recovery showed highly significant movement patterns in shoulder abduction and wrist supination during both reach and pass as well as the passing phase for elbow flexion ($p < 0.001$; Figure 3.7c). These altered movement patterns contrast with the regained success in completing the task. The altered movement patterns thus support the change of strategy applied during the task.

Robotic object-presentation task

A similar analysis to that described above was performed for the spherical object presentation. For this task, the full range of arm and hand markers was used (Methods 3.2.5). All four investigated animals (Mk-Pa, Mk-Re, Mk-Le and Mk-Jy) reached pre-lesional success-rates by the beginning of the chronic phase (Figure 3.5a), and were included in the analysis. As a general readout the wrist trajectory was assessed, where a clear disruption was observed in the acute phase, resulting in highly variant movement patterns in animals of the moderate group. Recovery of an intact-like trajectory was observed in all animals before the chronic phase (90 days post lesion), however, in the mild group this had already been achieved during the acute phase (Figure 3.8a). With the aid of the 3D motion tracking system, various features, such as velocity, angles and joint distances were extracted and their trajectories were time-normalized. Persistent changes in trajectory could be observed in some features, especially during the grasping and pulling phase (Figure 3.8b). Deviations from baseline trajectories were especially large in the moderate group. In order to approximate the differences of trajectories, the mean feature values during the reaching and grasping phase were calculated (Figure 3.8c). Out of the features calculated, $58.0 \pm 17.0\%$ were found to be significantly changed between the intact and the chronic phase, showing an altered movement pattern despite similar success-rates. A notable outlier was Mk-Re, where only 32% of features were significantly changed (Appendix 3). As in the BBT, changes in the underlying movement patterns, despite the recovery of functional control during this task, supports compensatory strategy use.

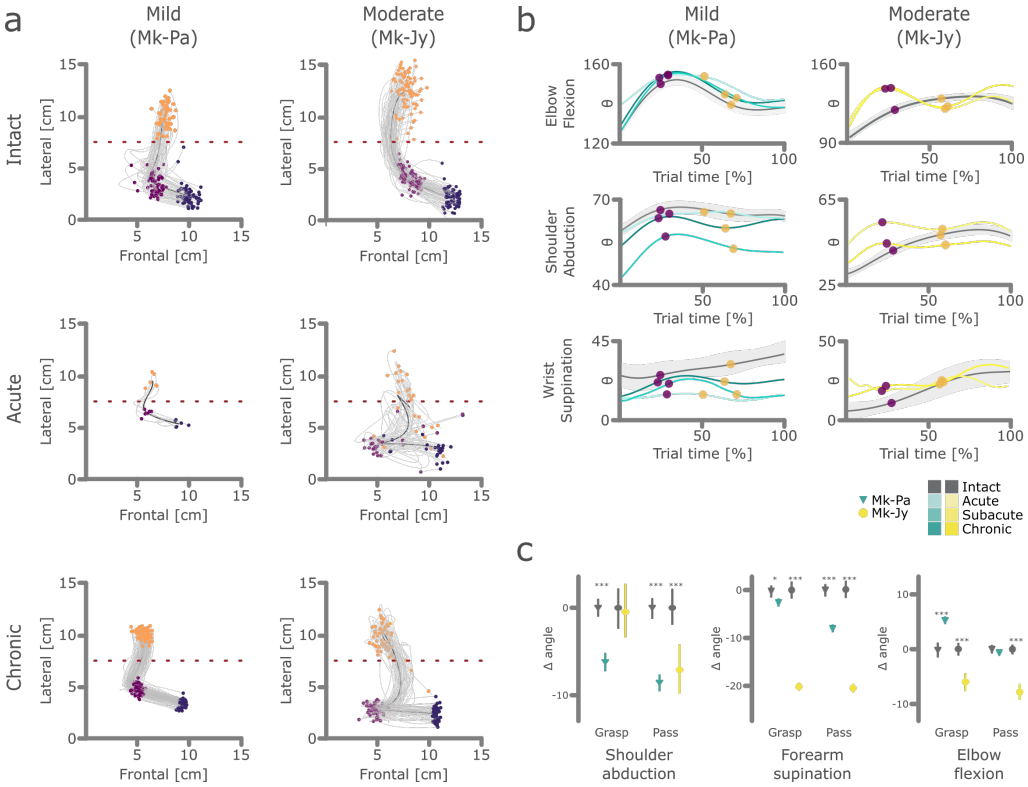

Figure 3.7: Persistent but altered movement patterns after functional recovery: Box and Blocks test The movement patterns in functionally recovered animals during the adapted Box and Blocks test are shown. (a) Wrist trajectories (gray) during the task completion with the movement events denoted as dots: start (blue), grasping (purple) and release (orange). The position of the box separator is indicated by the dashed line (red) (b) The mean angle trajectories during intact (gray with standard deviation), acute (desaturated), subacute(medium) and chronic (saturated) trajectories are displayed. The mean grasping point (purple) and passing of the separator (red) are marked. The trials were time-normalized to 100% duration. (c) The mean features and standard deviation of all measured angles during the grasping and passing phases were calculated. Significance was computed with a unpaired t-Test (***: $p \leq 0.001$, **: $p \leq 0.01$, *:$p \leq 0.05$)

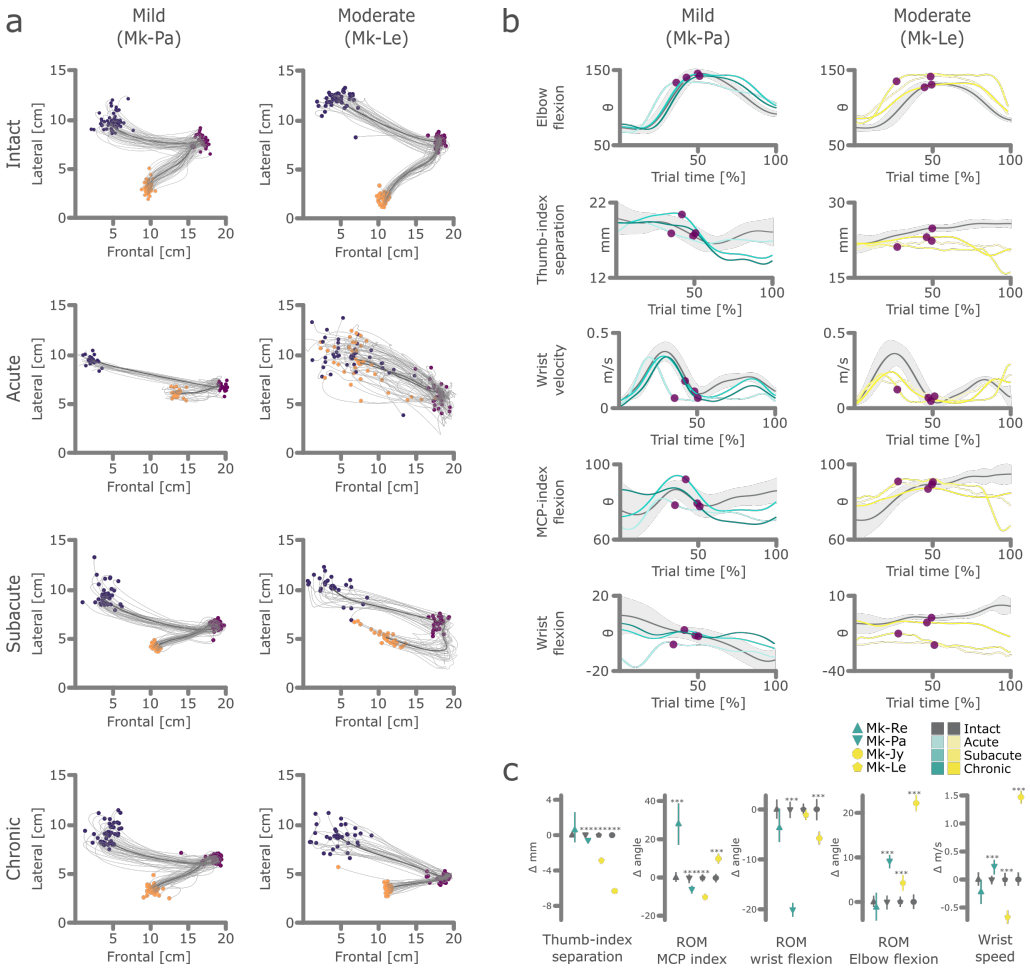

Figure 3.8: Persistent but altered movement patterns after functional recovery: Robotic object presentation The movement patterns during the spherical object presentation task are shown. All animals shown displayed pre-lesional performance levels upon reaching the chronic phase. (a) Wrist trajectories (gray) during the reaching and grasping are shown with dots denoting the start (blue), grasping (purple) and release (orange). (b) For two animals exemplary features are displayed. The mean angle trajectories during intact (gray with standard deviation), acute (desaturated), subacute(medium) and chronic (saturated) trajectories are displayed. The mean grasping points are marked (purple). The trials were time-normalized to 100% duration. (c) The mean features and standard deviation of all measured angles during the grasping and passing phases were calculated. The features were pooled from all days during the intact and chronic phases. Significance was computed with a Welch corrected t-Test (***: $p \leq 0.001$, **: $p \leq 0.01$, *:$p \leq 0.05$)

3.3.4 Principal component analysis based movement analysis

In order to obtain a unified measure of the kinematic deficits, a principal component analysis (PCA) was performed on the collected features (Methods 3.2.5 and 3.2.5), in both the BBT and the spherical object presentation task (Figure 3.9a,d). For the analysis, the trials were pooled into four time periods: before the lesion (intact), 1-30 (acute), 31-90 (subacute), and 91+ (chronic) days post lesion. In the PCA space, the euclidean distance between the performance during these critical time periods compared to the base line, was used as a general indicator of kinematic recovery.

The loading analysis in BBT revealed that the first principal (37.0%) component (PC) axis predominantly summarizes the movement quality (general trajectory and joint angles), whereas the second PC axis (23.0%) coded for the speed of execution (Figure 3.9c). The euclidean distance analysis revealed a significantly lower impairment of the mildly (Mk-Pa) and the two moderately impaired subjects (Mk-Le: $p < 0.001$; Mk-Jy: $p < 0.001$). While Mk-Pa shows a significant regression back towards the baseline performance, before plateauing during the chronic phases. Mk-Pa showed the largest deviation in the second PC and only marginal alterations to the overall movement quality. The recorded movements were, in general, relatively similar to each other in each respective time frame, as indicated by the relatively narrow distribution in both PC axis, with the acute phase showing the largest variance. In the moderate group, Mk-Le showed a recovery from being unable to complete the task in the acute phase, followed by a significant recovery between the subacute and chronic phase. Both Mk-Jy and Mk-Le showed strongly altered movement patterns during the chronic phase (Mk-Le: $p < 0.001$; Mk-Jy: $p < 0.001$). Whereas in the case of Mk-Jy, this coincided with the inability to perform the task, Mk-Le showed better performance scores than in intact recordings.

In the spherical-ROP, the loading factors showed the first (15.2%) coding for general hand shaping, with multiple inter joint distances, as well as the index finger extension, whereas the second PCs (12.0%) occupied a more gross motor domain, correlating with wrist control as well as the swiped area during the trial (Figure 3.9f). The euclidean distances from baseline performance showed a significant increase in three out of four animals, followed by a steep decline in kinematic impairment until the sub-acute phase (Mk-Re: $p < 0.001$, Mk-Le: $p < 0.001$; Mk-Jy: $p < 0.001$). Only Mk-Le showed further kinematic improvement during the sub-acute phase ($p < 0.001$). Nevertheless, Mk-Le and Mk-Jy showed significantly differing

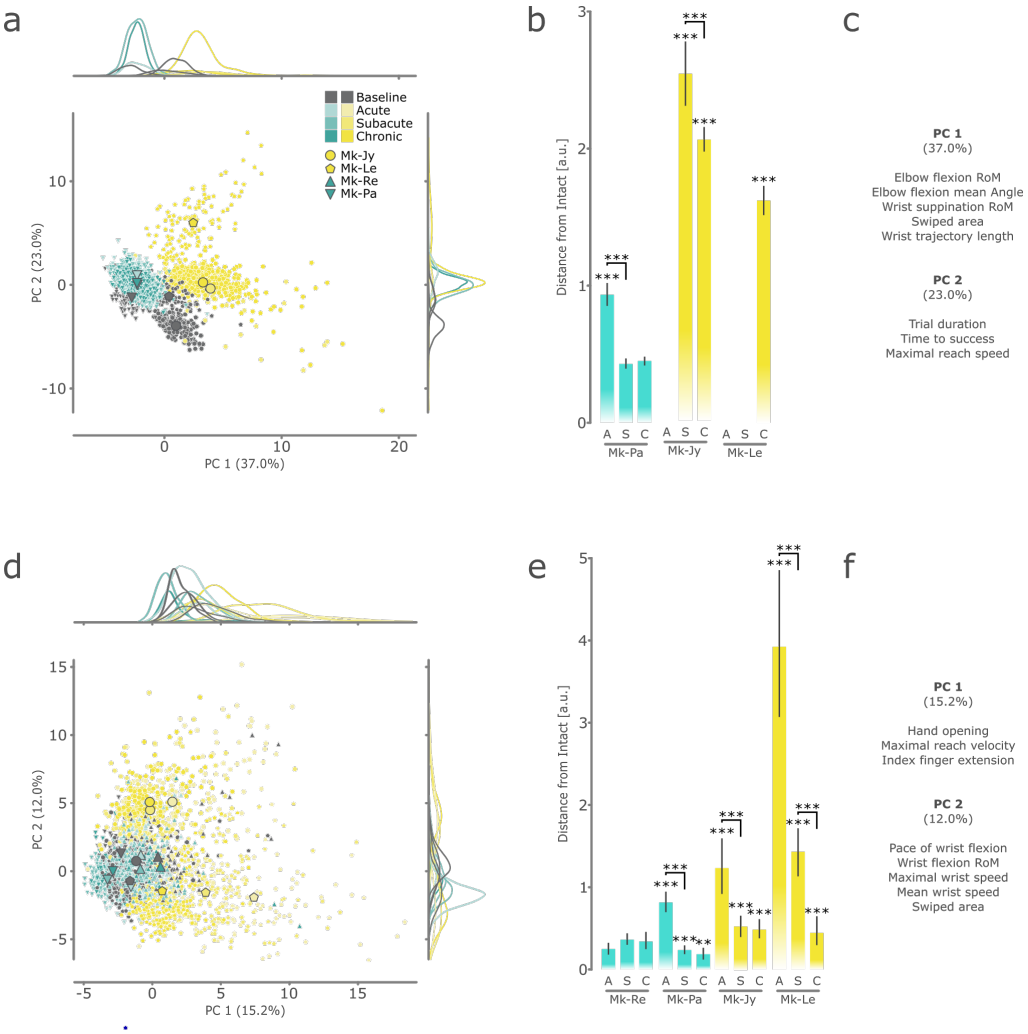

Figure 3.9: Principal component analysis: General reach and grasp control Movement qualification by principal component analysis of the kinematic features during the adapted Box and Blocks test, and the spherical object presentation task. (a,d) Qualified movements in the first and second principal component space, with single trials displayed as small markers and the centroids of each recovery period denoted by large markers. The point density along each principal component axis is reported in the marginal plots. (b,e) The euclidean distances from the baseline performance of each tested animal are reported during the acute, subacute and chronic phases. Empty bars denote no successful trials to be analyzed (c,f) Main features contributing to the first and second principal components (loading-factor ≥ 0.8) (a,b,c) adapted Box and Blocks test. (d,e,f) spherical object presentation test. The recovery period was subdivided into intact (gray), acute (A, p1-30, desaturated), subacute (S, p31-90, medium) and chronic (C, p91+, saturated) periods. The significance towards baseline performance is denoted by stars above the individual bars, with post-lesional changes denoted above connection lines (***: $p \leq 0.001$, **: $p \leq 0.01$, *:$p \leq 0.05$, Wilcoxon rank-sum, post-hoc corrected).

kinematic patterns compared to their intact performance, despite showing equal success in completing the task($p < 0.001$).

3.3.5 Qualitative assessment of flexor synergies in severely lesioned animals

Since subjects of the severe group (Mk-03, Mk-05, Mk-06, Mk-11) were not able to perform a single Drawer pull, as they could not extend their arm far enough to reach the object itself, the residual reach attempts during the recorded recovery period were assessed. The kinematics of the elbow flexion were analyzed, and a stark and persistent decrease in the range of motion was reported (Figure 3.10a). An unexpected by-product of this assessment was the qualitative observation of the development of aberrant flexor-synergies, a spasticity induced movement pattern, in 3 of the severely lesioned monkeys (Figure 3.10b). To our knowledge flexor-synergies have not previously been reported in a NHP model of stroke.

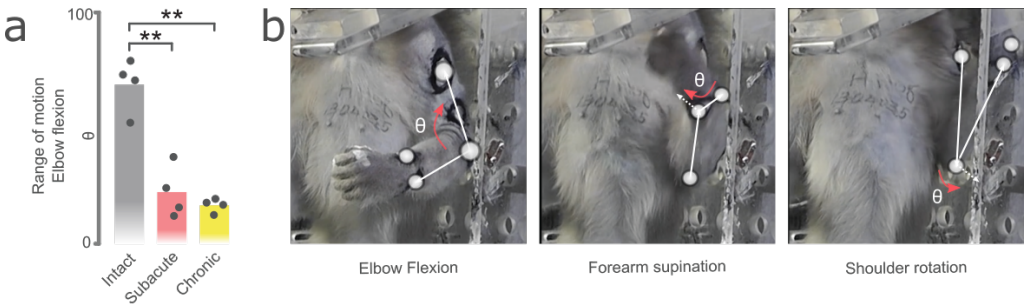

Figure 3.10: Flexor-synergy after severe subcortical stroke in NHP The severely impaired animals (n=4) were not able to perform any reaching movements post injury. A qualitative assessment of the residual movement patterns resemble the flexor-synergy seen in human stroke patients. (a) The residual range of motion for the elbow flexion was quantified, using a 3D marker based kinematic system (Reality Motion Systems, Germany). Both the sub-acute (p=0.005) and chronic (p=0.004) ranges of motions were significantly decreased compared to intact movements. (b) Exemplary depiction of the observed flexor-synergy pattern during attempted reaching. Flexor-synergy induced changes are indicated by the red arrows

3.4 Discussion

3.4.1 Task selection

As a goal of this study was the quantification of the residual movement and its recovery after subcortical stroke, the task selection was required to fulfill multiple standards: (1) clinical relevance, by assessing movements that would be relevant outside the laboratory setting (2) complementing the other tasks to yield a wide array of motor assessments, ranging from fine motor control to the assessment of the residual functional force, and (3) the ability to be integrated into the 3D kinematic recording system, to allow the assessment of the kinematic ability of the animal.

There are many tasks traditionally used in the assessment of upper-limb functionality in non- human primates, however many of them did not fit one or more of the criterion posed. Tasks using static objects (Brochier et al., 2004; Ethier et al., 2012; Schaffelhofer and Scherberger, 2016) or horizontally constrained manipulandums (de Haan et al., 2018; Omrani et al., 2016) were either not producing clinically relevant movements or were impossible to be integrated into the current setup. The recently developed robotic object presentation (Barra et al., 2019), however met these criterion, as the task is a highly versatile platform allowing the placement of objects in 3D space, and the subsequent free manipulation against a set amount of force. The platform allows for the attachment of multiple object types, ranging from objects requiring a precision grip to manipulate, to a cylindrical grip to assess the residual functional force a subject can apply. As a further powerful option of assessing the fine motor control, the modified Brinkman board was chosen, as the task of retrieving pellets out of small slots requires intact reaching, supination, as well as a precision grip to successfully perform (Brinkman and Kuypers, 1973; Rouiller et al., 1998). As the setup is fairly small it was easily integrated into the recording area. As a final tasks, a clinically proven upper-limb assessment was adapted for the specifications of NHP models: the Box and Blocks task (Hebert and Lewicke, 2012; Hebert et al., 2014). The adapted BBT allows for the assessment of skilled reaching and grasping of a small object and further assesses the lateral range of motion and coordinated object release.

3.4.2 Clinically relevant range of stroke phenotypes

In a clinical setting, many assessments for the residual movement ability in the upper-limb are used (Fugl-Meyer et al., 1975; Williams et al., 2000; Hayward et al., 2016; Santisteban et al., 2016). The cut-off for a severe

lesion is often defined as either the loss of dexterous hand movement, or in some cases, the loss of movement against gravity (Hayward et al., 2016). For mild and moderate lesions, many scales are less clearly defined, as many measures are insensitive to differences of that scope (Bohannon, 2004; Raghavan, 2015). As for the scope of this study, the cut-off between mild and moderate lesions was defined as a lasting deficit to perform a precision grip.

The assessment of the phenotypes produced thus suggested the splitting of the cohort into three distinct qualitative impairment groups: mild, moderate and severe. Mk-Re and Mk-Pa regained the ability to perform all tested tasks within the first month post-lesion (acute phase). They exhibited lasting deficits that would only be visible after thorough investigation of the movement pattern and the trained eye of the investigators. Their functional ability to perform the tasks successfully was indistinguishable from or even surpassed their performance while intact. They were thus qualified as the mild group. The observed impairment and functional recovery is consistent with spinal cord injury studies ablating 50% of the lateral CST at C4/C5 level (Sawada et al., 2015) and large lesions of the M1 cortex (Murata et al., 2008; Hoogewoud et al., 2013; Herbert et al., 2015). As a stark contrast, the animals in the moderate group (Mk-Le and Mk-Jy) experienced a severe loss of control in their manual dexterity, never reattaining the ability to perform any of the fine motor tasks again. During the rehabilitation process, they showed variable recuperation of their gross grasping ability and a significant shift to compensation strategies. This lesion degree seems to mirror the impact of a large sensorimotor cortex lesion targeting the hand M1 area and spanning into the caudal parts of PMd and PMv (Liu and Rouiller, 1999a; Murata et al., 2008; Hoogewoud et al., 2013).

The severe group (Mk-03, 05, 06, 11) was qualified by the absence of quantifiable recovery of even gross hand and arm function. In contrast to the other two groups, these animals also showed a severe impairment in their reaching ability, precluding them from performing any of the posed tasks post lesion induction. This degree of severity is congruent with spinal hemi sections and contusions at cervical level and full CST ablations (Salegio et al., 2016; Barra et al., 2021).

3.4.3 Residual kinematic impairment after full functional recovery

The question "to which extent patients experience motor recovery or motor compensation after stroke?" has long been one of the big debates in the field

(Nakayma et al., 1994; Roby-Brami et al., 2003; Levin et al., 2009; Murphy and Corbett, 2009; Darling et al., 2011; Alaverdashvili and Whishaw, 2013; Krakauer and Carmichael, 2017). As patients recover from the insult, they might partially regain the ability to perform the various motor tasks of every day life. The aim of neurorehabilitation applied in clinics is to aid the patients in relearning motor patterns. The progress of the rehabilitation is routinely measured using different performance scales such as the Fugl-Meyer Test (Fugl-Meyer et al., 1975) and many others (Santisteban et al., 2016). Many of these assessments do not distinguish between progress due to a regaining of motor ability, or to the perfection of a compensatory strategy used to perform the tested tasks (Levin et al., 2009). This leads to an information disconnect as to whether the applied therapies are effective in the restoration of the underlying bodily functions and processes (recovery) or whether they efficiently teach and cement coping strategies (Krakauer and Carmichael, 2017). However, to advance in the investigation of future rehabilitation techniques, such a distinction is of utmost importance. One suggested mode of action to distinguish these two modes of recovery is to split measurements into two categories: the ability to perform certain tasks and the underlying kinematic movements.

This concept was investigated in the present study, by splitting the success rate in any task from the kinematic measurement. While all animals in both the mild and moderate groups showed some improvement in the ability to successfully complete the tasks, the analysis of the underlying kinematics told a different story. In all moderately impaired animals, the kinematic patterns were significantly altered, even in tasks where they fully recovered the ability to perform the task at intact levels. In Mk-Le, who showed a functional recovery in performing the BBT task with a higher success rate than achieved during intact recordings, retained the same kinematic method, while seemingly perfecting the strategy of coping with the impaired movement control, demonstrating that compensation can fully mask the remaining deficit in a complex reach-and-grasp task. Similar results have previously been reported in human patients by Roby-Brami et al. (2003). In the mild animals, there was a marked improvement during the acute phase, however, in the later phases, as in the moderate group, there was very little change in the underlying kinematic quality. This provides evidence, that no matter the lesional impact, recovery has a very limited time frame in which it can take place, with a large part of the improvement stemming from the optimization of compensation strategies still possible with the remaining motor function (Biernaskie, 2004; Merdler et al., 2013; Cortes et al., 2017).

These findings further support the need for a clear distinction between mo-

tor recovery and compensation in the search for new rehabilitation paradigms. This is especially true for mechanistic neuronal studies targeting specific circuits and brain areas to improve the functional outcome after a stroke.

3.4.4 First evidence for flexor synergies in a NHP model

The monkeys included in the severe group (Mks-03, 05, 06, 11) were not able to perform a single successful post-lesional trial in either of the tested tasks (modified Brinkmann board and drawer task), due to a vastly decreased control of the upper-limb. To nevertheless quantify the deficit past a crude 0% success rate assessment, the range of motion during the residual movement attempts were investigated. From this investigation, it became evident that the remaining movement followed highly stereotypical movements: an elbow flexion followed by a forearm supination and a lateral shoulder rotation. This corresponds with the flexor synergy that has been previously described in hemiparetic stroke patients (Twitchell, 1951; Brunnstrom, 1970; Dewald et al., 1995, 2001).This synergy has been reported to be a major indicator for a poor upper-limb recovery process, and even an indicator for post stroke deterioration of everyday tasks. Further a lesion characterization study of patients with and without spasticity revealed a common lesion site in spastic patients, that very closely resembles the lesion site found in the severe group investigated here (Cheung et al., 2016). As of today, the presence of flexor synergies in an experimental NHP model has not been described. As the mechanistic processes leading to these symptoms are not fully understood, novel and pivotal insight into the treatment and amelioration of these symptoms could be gained from the study of the present subcortical stroke model.

3.5 Limitations

In the analysis of the presented tasks, one major limitation was the reliance on markers for the assessment of the 3D kinematics. The interaction of the monkeys with the markers sometimes produced a loss of signal during recording sessions. Furthermore, the necessity of applying a glove to the hand of the animal, further diminishes sensory feedback from the fingers. This could have devastating effects on the animals ability to perceive the presented objects. With the emergence of marker-less pose estimation algorithms (Nath et al., 2019; Karashchuk et al., 2021), a switch to such a system might prove advantageous in the finer motor assessment tasks, especially in tasks such as the modified Brinkman board, where marker

based assessments are impossible due to the monkeys feeding themselves and having full access to the markers.

In a similar way, the reliance on task-dependent assessments for the quantification of clinically relevant impairment has its innate problems. As the task can only be completed with a defined set of movements, the methods used do not describe changes in behavior of free-roaming animals. As such, the applied testing might lack the sensitivity to describe mild deficits, as seen in Mk-Re. Also, marker-less observations in a natural habitat might reveal subtle adjustments in behavior changes, not visible during the constrained recording sessions (Berger et al., 2020; Bala et al., 2020).

3.6 Conclusion

The functional deficit in a wider array of clinically relevant tasks was assessed in a novel model of subcortical stroke in non-human primates. The observed phenotypes represent a clinically relevant range of deficits observed in human patients, with flexor-synergies present in the most severe group. The residual kinematic deficits were quantified, and it could be demonstrated that compensatory movement strategies form a major component in functional recovery after stroke.

Chapter 4

Unbiased quantification of multi-cortical descending axonal projections after subcortical stroke in non-human primates

4.1 Introduction

Subcortical strokes comprise 25% of all stroke incidents in human patients (Sudlow and Warlow, 1997; Wang et al., 2007; Ramsey et al., 2017). As compared to cortical strokes, even very small lesion sizes can lead to a great loss in motor function. This discrepancy stems mainly from the anatomy of these structures. While the computational layers of the cortex are distributed over a relatively large amount of cortical surface, the subcortical regions comprise of highly aggregated bundles of axons, transmitting signals cortico-cortically, or in the case of the CST, corticospinally. The internal capsule forms the main relay from the brain to the spinal cord, with the corticospinal tract relaying direct motor commands to the spinal cord and, ultimately, to the musculature. At its narrowest parts, the internal capsule spans only a few centimeters, with small lesions potentially interrupting a large portion of the brain's efferent control. The amount of corticospinal

tract spared after a sub cortical stroke is currently the best predictor of the residual and regained motor function a patient can achieve during rehabilitative training (Park et al., 2016; Ramsey et al., 2017). However, in many cases, the recovery lags behind expected outcomes. Indicators currently used in the clinic are often inconclusive, presenting a dire need for the adjustment of predictive techniques and markers, in order to provide the best possible care to the affected (Hayward et al., 2016; Krakauer and Carmichael, 2017). Possible reasons for this lack of predictability might be two-fold in nature: confounding lesion locations may mask the real indicators, and a lack of resolution in the clinical assessment methods may also contribute. By harnessing the specificity and resolution of histological assays, this study aims to provide insight on the involvement of the motor region specific sub-tracts in the corticospinal tracts, and their individual contribution to impairment and recovery after an internal capsule stroke.

The corticospinal tract is comprised of topographically arranged tracts originating from the different regions of the cortex (Morecraft et al., 2002). About 50% of neurons in the CST originate within the primary motor cortex (M1), with the premotor cortices (PM) and supplementary motor area (SMA) accounting for a combined 40%. While lesions affecting the cortico-fugal M1 projections show the most significant correlation with motor function loss, the amount of residual CST integrity of the dorsal and ventral PM, as well as the SMA, have been associated with a decline in expected performance after stroke (Riley et al., 2011; Schulz et al., 2012). In this study, a histology based quantitative assessment of the interruption of M1, PMv and PMd after a focal subcortical lesion was performed. The relative location of the affected tracts was then investigated by the registration of the histological preparations into the Montreal Neurological Institute (MNI) standard atlas space for *M. fascicularis*.

4.2 Methods

4.2.1 Animal Model

The animals included in this study as well as their housing situation are described in chapter 4.2.1. In addition to the described animals 2 further animals were included in the study. Mk-Va and Mk-Me, two young aldult (3.3 ± 0.3 years) (*M. fascicularis*), weighing $3.1 \pm 0.2kg$ were included in the study. They were housed in the described Fribourg facility and investigated according to license 2020_26_FR. They served as intact control animals for the described tracing procedures.

4.2.2 Tracer injection

The animals were sedated and prepared for surgery as described in chapters 2.2.2 and 2.2.2.

A craniotomy exposing both the central- and the arcuate sulci was performed, providing access to the areas to be injected: the primary motor cortex (M1) and pre-motor cortices (PMv and PMd). The extracted bone flap was kept in ringer-lactate solution. The dura mater was incised and rolled up toward the mid-line, where it was kept hydrated with saline solution. Micro-electrode arrays implanted in the injection sites, were explanted prior to injection. M1, PMv and PMd were each sequentially injected with one tracer respectively: AAV8-CAG-drComet (titer: $7.89E12$), AAV5-CAG-gComet (titer: $1.44E13$; unpulished, Aebischer Lab, EPFL, Switzerland), biotinylated dextran (BDA-10000, Invitrogen D1956, USA, 1:10 in H_2O). All tracers were injected with 4 nl/s using 10 μl glass syringes and 35G beveled needle tips (NanoFil, World Precision Instruments, United Kingdom). The injections were regulated with a UMP3 injection pump with a Micro 4 controller (World Precision Instruments, United Kingdom). Depending on the injection site multiple depths were injected, starting with the deepest and ending with the most shallow. After the last injection at each site, the needle was left in place for 1 minute to ensure adequate diffusion. The injection pattern and volumes are described in (Figure 4.1). Areas that were not actively injected were kept hydrated using saline soaked cotton balls.

The dura was then sutured, and the bone flap was replaced and fixed with 4x1 titanium mesh pieces (TiMesh, Medtronic, Ireland) and self-drilling screws (1.6x3.5 mm, Medtronic, Ireland). Gaps in the bone structure were filled with Spongostan™(Johnson&Johnson Medical, Belgium). The skin

was then sutured and disinfected with Betadine solution (Mundipharma, Switzerland).

Post operative care was administered as described in chapter 2.2.2.

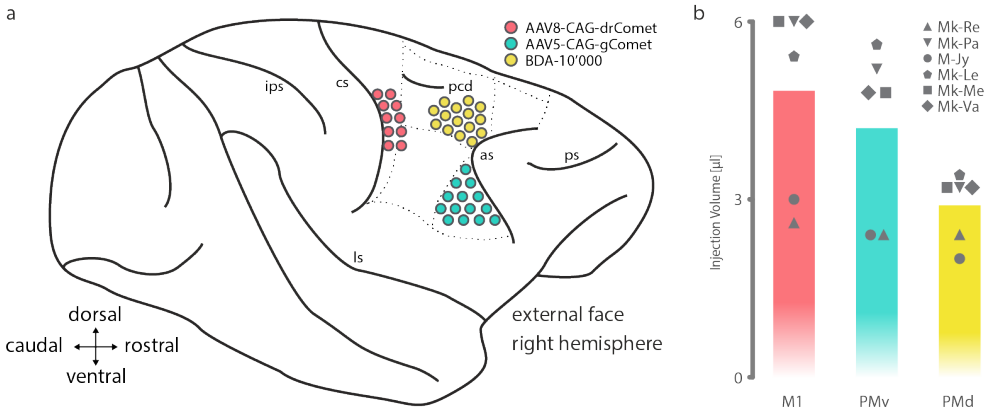

Figure 4.1: Neuronal tracer injections (a) The injection plan for the triple color injections in the motor cortex. The injected regions were located in the upper-limb regions of (1) M1 with AAV8-CAG-drComet (red), (2) F5/PMv with AAV5-CAG-gComet (cyan), and (3) F2/PMd with BDA-10000 (yellow). Sulci are denoted as: cs - central sulcus; as - arcuate sulcus; ips - intraparietal sulcus; ls - lateral sulcus; pcd - precentral dimple; ps - principal sulcus.(b) The injected tracer volumes in each region and animal are reported.

4.2.3 Histological processing

The tissue was extracted and processed according to the protocols described in chapters 2.2.9, 2.2.11 and 2.2.13.

BDA staining The staining of the injected biotinylated dextran amine (BDA) staining was conducted using the components of the Alexa Fluor™ 647 Tyramide SuperBoost™Kit (B40936, Invitrogen™, USA).

The slices were mounted onto slides and left to dry. They were then washed (3x, 0.1 M PBS). Endogenous peroxidase activity was quenched using 3% hydrogen-peroxide solution (500 μl, 1h, RT). After a wash sequence (3x, 0.1 M PBS), the tissue was blocked for 1h with 10% normal-goat serum in PBS (0.1M), followed by an over-night incubation at 4°C with HRP-conjugated streptavidin solution (7 drops, Kit). On the second day, the tissue was washed (3x, 0.1M PBS) and amplified with tyramide solution (200 μl, Kit) for 5 minutes. The amplification reaction was stopped by

adding 200μl stop reagent solution (Kit). The tissue was washed (3x, 0.1 M PBS), incubated with DAPI solution (1:100 DAPI in 0.1 M PBS, 10 min), washed again (3x, 0.1M PBS), dried and cover slipped (ProLong™Diamond Antifade Mountant, P36961, Invitrogen™, USA). All sections were imaged whole with four imaging channels (DAPI, FITC, Cy3 and Cy5) at 10x magnification with a slide scanner microscope (VS120, Olympus, Japan).

anti-GFP DAB Brain slices per well were transferred into 6-well plates filled with 0.1M PBS. The slices were washed (3x, 0.1M PBS) and incubated with 0.3% hydrogen-peroxide solution (1ml, in 0.1M PBS) for 15 minutes before blocking (3x5 min, 2% NGS - 0.5% TritonX-100 in 0.1M PBS). The slices were then incubated with anti-GFP antibody (1:500 in 2% NGS - 0.5% TritonX-100 - 0.1M PBS, Merck AB3080) for 4 nights at 4°C. The slices were washed (3x, 0.1M PBS) and incubated with biotinylated IgG secondary antibody (1:500 in 2% NGS - 0.5% TritonX-100 - 0.1M PBS, Vector Labs BA-1000) for 90 minutes at room temperature, before again being washed (3x, 0.1M PBS). The signal was visualized using the Vecastain ABC Kit (Vector Labs PK-6200). The slices were incubated with DAB solution (Kit) for 3 minutes before washing (3x, 0.1M PBS), mounting and coverslipping with Mowiol. All sections were imaged whole (brightfield) at 10x and 20x magnification with a slide scanner microscope (VS120, Olympus, Japan).

Tissue preparation spinal cord

The spinal cords were dissected into subsections according to the position of the dorsal roots. We obtained 5 sections: Brainstem-C2, C3-C4, C5-C8, T1-T2 and T3-T4. The sections were individually transferred into falcon tubes with 20% sucrose in 0.1M PBS. After one week they were transferred into 30% sucrose solution and left to rest for another 2 weeks. The tissue was embedded into O.C.T. compound (Tissue-Tek®, Sakura Finetek, USA) and then frozen by submerging it in iso-pentane for 5 minutes at -65°C (SnapFrost®80, Alphelys, France). The tissue was then transferred into an -80°C freezer. The tissue blocks were then cut into 40μm sections with a cryostate. The sections were stored in 0.1M PBS azide (0.03%) for further processing.

anti-GFP & anti-RFP signal amplification The sections were transferred into 24 well plates filled with 0.1M PBS (3 sections per well). They were washed (3x, 0.1M PBS) and blocked in normal goat serum solution (5% NGS - 0.25% TritonX-100 in 0.1M PBS) for 1 hour at room temperature. The sections were incubated with either anti-GFP (rabbit, Merck AB3080)

or anti-RFP (rabbit, Rockland 600-401-379) antibodies (1:500 in 5% NGS - 0.25% TritonX-100 in 0.1M PBS) for 4 nights at 4°C. The slices were then washed (3x, 0.1M PBS) and incubated with a fluorescently labeled secondary anti-rabbit antibody (Alexa fluor 647, 1:500 in 5% NGS - 0.25% TritonX-100 in 0.1M PBS, Life technologies A21245) for 90 minutes at room temperature. The slices were washed (3x, 0.1M PBS), mounted and coverslipped with Prolong (ProLong™Diamond Antifade Mountant, P36961, Invitrogen™, USA). All sections were imaged whole with four imaging channels (DAPI, FITC, Cy3 and Cy5) at 10x magnification with a slide scanner microscope (VS120, Olympus, Japan). The resulting images were used for the spinal cord quantification (Figure 4.2)

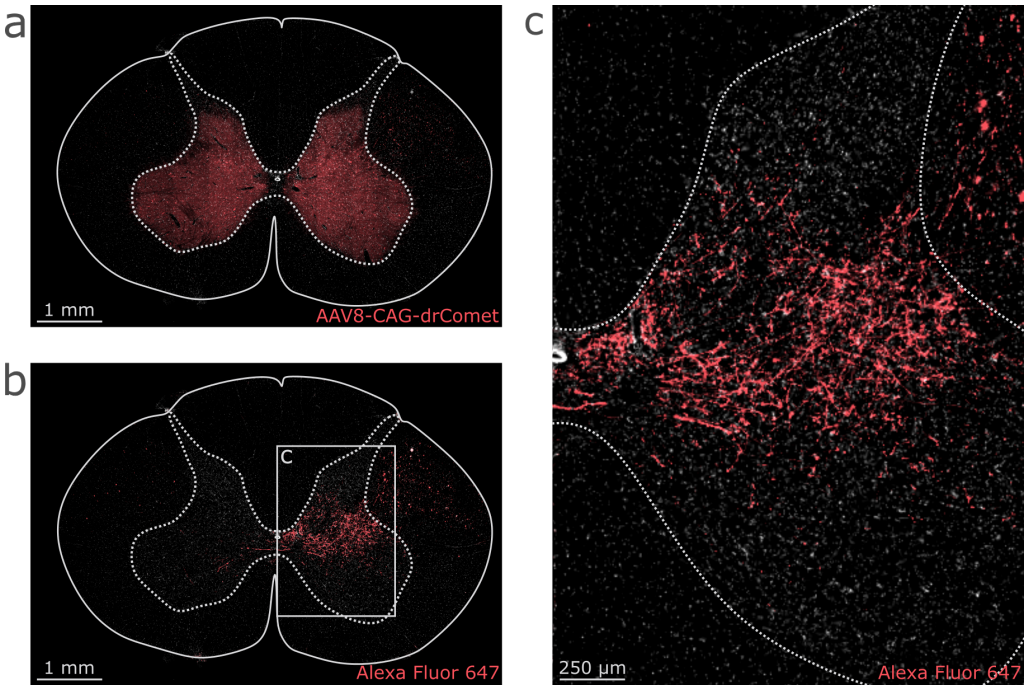

Figure 4.2: Fluorescence signal amplification in spinal cord Deptictions of the fluorescent signal of a spinal cord section at level C5 pre- and post-amplification with an anti-RFP staining assay. (a) Exemplary fluorescent AAV8-CAG-drComet signal imaged in a red channel (488-532 nm). A high amount of auto-fluorescent signal is present in the gray matter. (b) Exemplary signal of the signal post-amplification with anti-RFP antibody and Alexa fluor 647, imaged in a far-red channel (594-643 nm). A vastly improved signal to noise ratio could be achieved. (c) A magnified image of the fluorescent AAV8-CAG-drComet signal.

4.2.4 Internal capsule fiber quantification Pipeline

In order to quantify the lesion induced fiber density loss in the IC a pipeline consisting of 6 steps was devised : (1) software assisted manual marking of the Internal capsule and the surrounding structures, (2) segmentation of the neurons using pixel classifiers, (3) extraction of the direction of the marked neuronal tracts (4) 3D volume creation of the internal capsule, (5) neuronal direction extraction and clustering into distinct neuronal tracts, and (6) animal wise normalization, accounting for injection differences(Figure 4.2)

As each section image amounted to multiple gigabytes of data, only the internal capsule was used for this in-depth analysis, achieved by labeling the IC and IC adjacent structures, in QuPath (Bankhead et al., 2017) and using these as a mask for subsequent analysis steps (Figure 4.2a). In a next step, the traced neurons were automatically marked. To achieve this, representative sample images were selected in one data set and combined into a training image. On the training image, around 50 neuron and non-neuron structures were labeled. A pixel classifier based on a multi-layer perceptron artificial neural network (MLP-ANN), was then trained on the marked pixels. The classifiers were trained on selected, representative image regions, using all four acquired channels (DAPI, FITC, Cy3 and Cy5). For fiber segmentation the best performing combination of filters was found to be: Gaussian, Laplacian of Gaussian, Weighted standard deviation, and Hessian minimal Eigenvalue. The filters were applied at a resolution of 2.59 μm/pixel. Individual classifiers for each injected virus, and the far-red BDA staining were created, and the obtained classification was applied as a neuronal mask for further processing steps. This resulted in 5 MLP-ANNs that allowed to automatically mark the neuronal tracing present in all monkeys involved in this study (Figure 4.2b). The main CST tract and collateral branches were then pieced apart utilizing the directional analysis tool OrientationJ (Püspöki et al., 2016; Rezakhaniha et al., 2012) developed for Fiji (Schindelin et al., 2012). This allowed the measurement of the local direction in a provided image of each segmented neuronal pixel (Figure 4.2c).

To identify the injection site and the labeled fiber tracts we trained pixel classifiers with QuPath's integrated multi-layer perceptron artificial neural network (MLP-ANN) (Bankhead et al., 2017).

Combining histological images with neuronal tracing in the internal capsule, a volume of the internal capsule was created, and subsequently dorso-ventrally sliced into 20 sections. The distribution of the observed directions in each section was captured and the probability density functions esti-

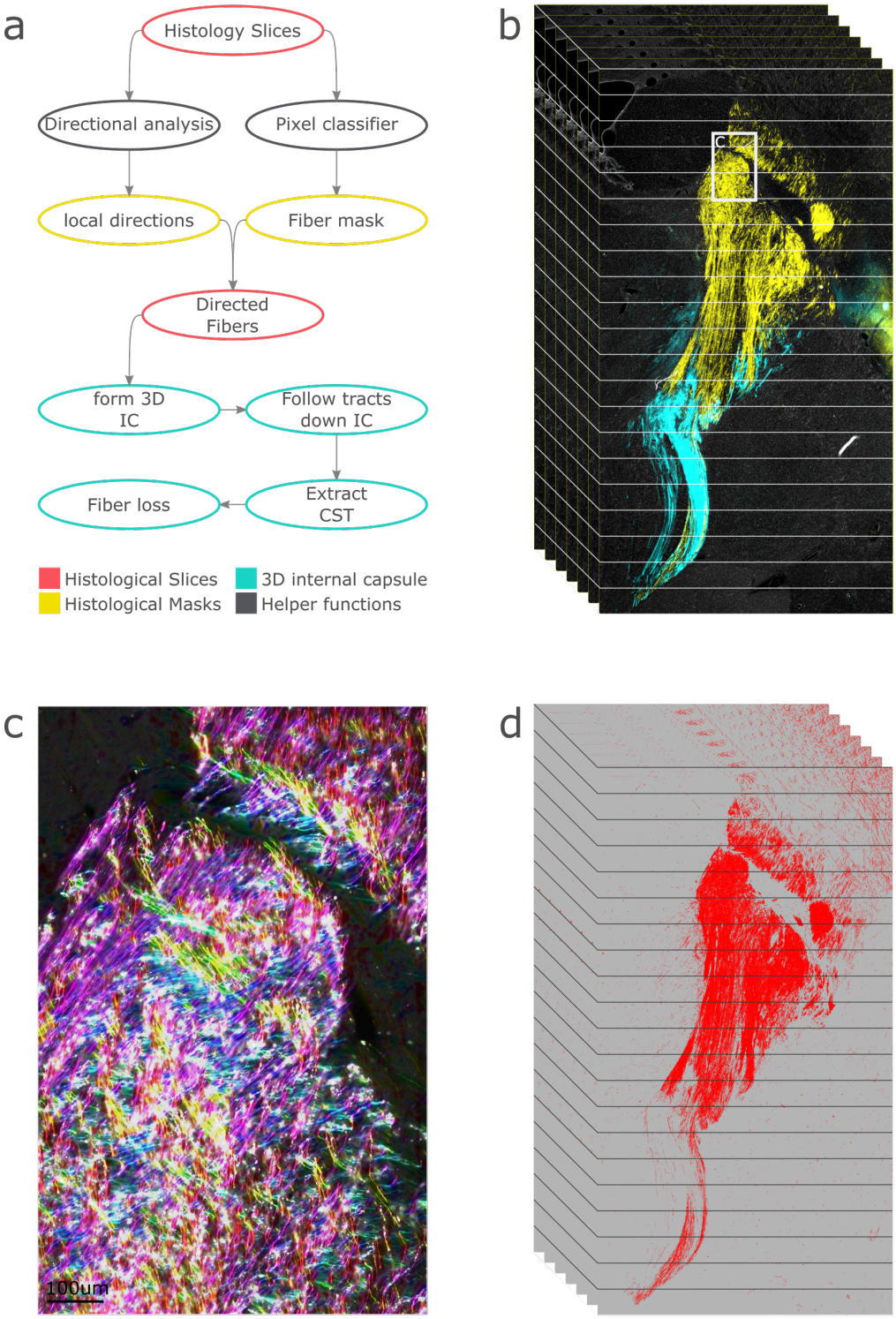
a
Histology Slices
Directional analysis
Pixel classifier
local directions
Fiber mask
Directed Fibers
form 3D IC
Follow tracts down IC
Fiber loss
Extract CST
Histological Slices
Histological Masks
3D internal capsule
Helper functions
b
c
100um
d

Figure 4.2: Direction based corticospinal tract detection Depiction of the image processing pipeline for the detection and isolation of the corticospinal tract from other tracts in the internal capsule. (a) A graphical depiction of the analysis pipeline is displayed. From the histological slices two data streams are analyzed: the fiber mask and the local directionality. The data streams are later combined to form an ensemble of fibers with known directionality throughout the internal capsule. In a series of steps, a 3D representation of the internal capsule is built and the tracts are split into subtracts by directional clustering. The tracts passing through the entire internal capsule are isolated. From this isolated tract the fiber loss is calculated using intact subjects' baseline. (b) Exemplary representation of descending tracts through the internal capsule volume. The descending fiber tracts of M1 (yellow) and PMv (cyan) and cell bodies (white) are shown. The rectangle depicts the area represented in (c) Exemplary close up of directionality analysis assay. Different hues depict the different local direction of fibers. (d) An exemplary 3D representation of the internal capsule with the pixel classifier generated fiber mask (M1) in red.

mated with circular kernel density estimation (cKDE). The fitted kernel was obtained using a von Mises distribution, a circular equivalent of the Gaussian distribution (Mardia and Jupp, 2000; Rezakhaniha et al., 2012). The smoothing factor (kappa=25) was empirically chosen. This method allowed for clustering of the dominant directions in each slice by separating the cKDE by its mathematically well-defined minima. For each cluster or 'tracelet', the circular mean (cMean) and standard deviation (cSTD) were computed (Mardia and Jupp, 2000). Each sections' tracelets were then matched up with the next sections' tracelet, and the tracelets matching within ($cMean \pm 1.7 * cSTD$) were connected, eventually forming continuous 'traces' throughout the volume, with some tracts eventually exiting the internal capsule, and others deviating and innervating internal capsule adjacent structures (Figure 4.2).

For each animal, the tracts exiting the internal capsule were selected, by computing the maximally intense tract. Their intensity throughout the internal capsule volume was measured and normalized by the maximal section intensity per animal, accounting for differences in viral expression efficiency and projection patterns above the internal capsule. Providing a quantification method for the fiber tract interruption caused by the administered subcortical stroke.

4.2.5 Spinal Cord Pipeline

The projections in the spinal cord were analyzed from the first segment of the cervical spinal cord (C1) until the fourth segment of the thoracic spinal cord (T4). For the grey matter lamina analysis we used far red counter-stained sections (Chapter 4.2.3). The acquired images were pre-

processed using QuPath(Bankhead et al., 2017). To automatically segment the grey and white matter, we employed a Gaussian blur followed by automatic thresholding provided by Fiji (Intermodes, Percentile, Schindelin et al. (2012)). Manual correction was applied as needed. The images and annotations were then exported for further analysis (Figure 4.3).

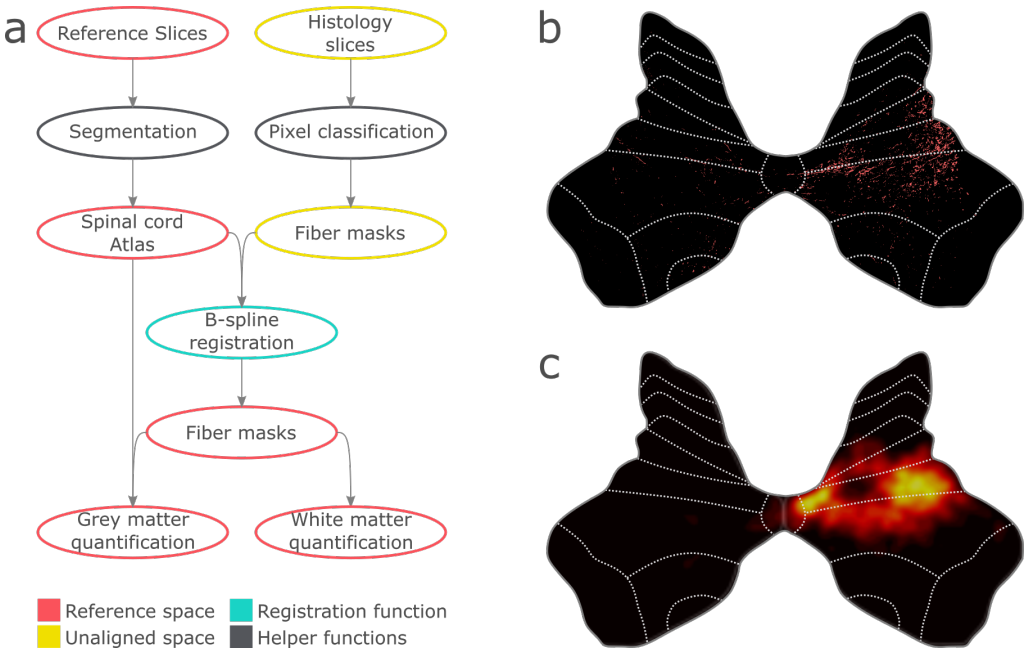

Figure 4.3: Spinal cord analysis pipeline Depiction of the image processing pipeline for a standardized analysis of the descending tracts in the spinal cord, both in the gray matter and the white matter respectively (a) A graphical depiction of the analysis pipeline is displayed. From the histological slices, a fiber mask is extracted using an artificial neural network based pixel classifier. The resulting signal masks were then registered to the reference space of the created spinal cord atlas. Group-wise analysis of both the terminations in the gray matter, as well as the descending tracts in the white matter, were then performed. (b) Exemplary representation of the registered termination in a C5 section. The descending fibers tracts of M1 (red) are shown overlayed with the spinal laminas outlined in white. (c) A representation of the summed termination signals (M1) at spinal level C5.

Lamina analysis

Using the exported annotations, the individual spinal cord sections were registered to a labeled spinal cord atlas adapted from a *M. mulata* spinal cord atlas (Sengul, 2012). The atlas was transferred to representative sections of *M. fascicularis*, by affine registration of the lamina annotations of the original atlas using simpleITK (DoF: 12, (Lowekamp et al., 2013)).

These sections were used as the reference images for further registration. The further registration was performed likewise with the simple-ITK library using the atlas as the fixed image, pairwise registering the individual sections. A rigid alignment was first performed and followed by a b-spline transformation. The signal, grouped by the respective spinal cord segment and analyzed the signal intensity in the general gray-matter as well as separately in each lamina, was summed. The signal was normalized by the maximal amount of signal of the descending tract in the internal capsule (Chapter 4.2.4)

White matter analysis

The projections in the white matter were analyzed using the previously gray- and white-matter segmented images. The fibers were detected using a pixel-classifier, as previously described in Chapter 4.2.4, but with a focus on more circular structures. Individual descending fibers were then distinguished by applying a watershed algorithm. The number and location of the descending fibers was calculated for each slice, and subsequently summed per segment. The summed signals were then registered to the adapted spinal cord atlas, as described in section 4.2.5.

4.2.6 Statistics

All data was reported as $mean \pm SD$. Significance calculations were performed using paired t-tests followed by post-hoc correction for multiple comparisons.

4.3 Results

4.3.1 Tri-color tracing

The health and sparing of the descending corticospinal tracts after a stroke is one of the core indicators of the expected recovery in patients. Therefore, a detailed study of the descending tracts was conducted, focusing on some of the most promising motor areas involved in regaining hand motor function after stroke: M1, PMv, and PMd (Riley et al., 2011; Schulz et al., 2012). The three areas were labeled with anterograde neuronal tracers, in healthy conditions ($n = 4$), as well as in individuals that previously underwent subcortical lesioning ($n = 8$) (Figure 4.4). Before the tissue was dissected and processed for the histological assessment, the brain was

extracted and a high resolution post mortem DTI was acquired in collaboration with the Center for Biomedical Imaging (CIBM, EPFL, Switzerland, Methods 2.2.10). The brain tissue was then dissected and stained to illuminate the non-autofluorescent traces (BDA). To enable the further analysis, high resolution images of whole hemisphere sections were acquired using a slide-scanner system (Figure 4.5).

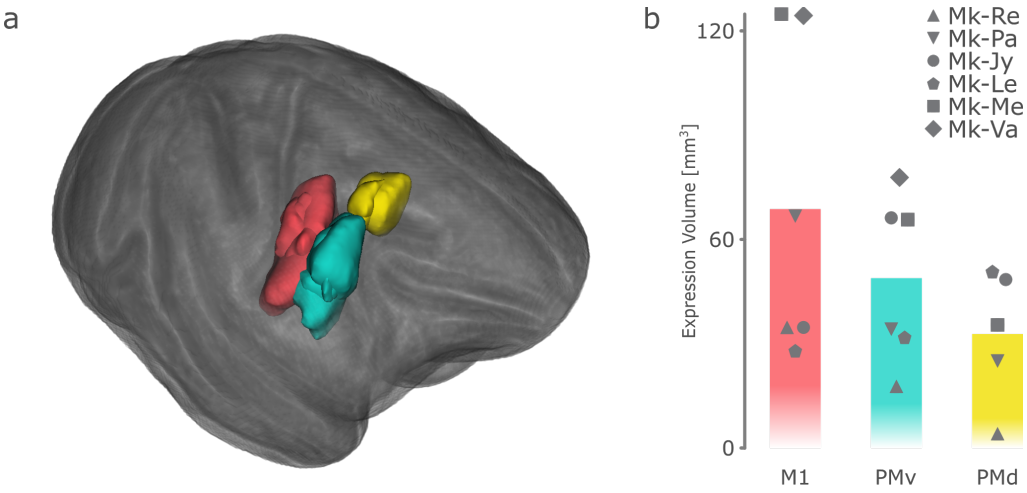

Figure 4.4: Tri-color tracing: injection sites A depiction of the effective expression volumes in the normalized atlas space (MNI Atlas, *M. fascicularis*, Frey et al. 2011). (a) Overlapped expression in injection sites of the three injected motor cortical areas M1 (red), PMv (cyan), and PMd (yellow). (b) The mean expression volumes of each injection site with the individual animals broken down.

4.3.2 Histological assessment of tract interruption

As the neuronal tracts descend through the IC, some of them will interact with the surrounding structures, such as the putamen or thalamus. These neurons eventually branch off and reach their target at an angle towards the general direction of the CST. Assuming the percentage of fibers innervating surrounding structures and descending into the spinal cord is similar between animals in the healthy condition, the natural decrease in fiber density throughout the internal capsule should be constant between animals. A deviation from this general decline, especially a decreased emerging neuronal output, could therefore be largely attributed to a lesion situated in the IC, thus allowing the quantification of the interruption of the CST, specifically.

From each animals CST tracts, the dominant descending tracts were normalized by their maximal prevalence in the IC (Figure 4.6a). The remaining

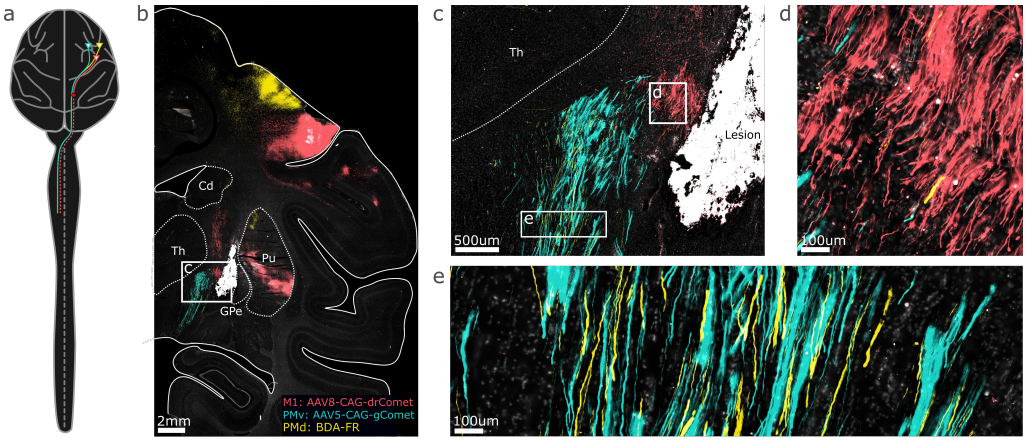

Figure 4.5: Tri-color tracing: descending tracts An exemplary depiction of the three descending tracts of M1, PMv and PMd passing through the internal capsule (Mk-Le). (a) Schematic representation of the descending tract with M1 fibers (red) stopping at the lesion level, with PMd (yellow) as well as PMv (cyan) bypassing the lesion tissue and descending into the spinal cord. (b) Coronal section of the lesioned hemisphere. The lesion is visible in white (auto-fluorescence), with tracts from M1 above the lesion, and PMv and PMd below. The sections outline (solid) and internal capsule adjacent structures (dashed) are outlined in white. The injection sites of both M1 and Pmd are visible in the cortical area. (c-e) Close up images with all three tracts as well as the lesion visible. The pre-motor cortex fibers traverse dorsal to the M1 tracts. (d) The seperate tract of M1 is depicted in red and (e) the intermingling tracts of PMd and PMv corticospinal tract.

CST below the maximal lesion extent was then taken to estimate the remaining fibers originating from each traced cortex, and descending into the spinal cord (Figure 4.6b). In fibers originating in M1, a significant decrease in fiber density was observed in the two of the lesioned animals, as compared to the control group, with an estimated sparing of $24.9 \pm 4.9\%$ in Mk-Le ($p < 0.001$) and $1.1 \pm 1.2\%$ in Mk-Jy ($p < 0.001$). This decrease was non-significant in both Mk-Re and Mk-Pa. PMv fibers were significantly reduced in two animals, with Mk-Re experiencing a full loss of fibers ($0.7 \pm 0.2\%$, $p < 0.001$), and Mk-Jy retaining $41.4 \pm 8.2\%$ ($p < 0.01$) of fiber density. In PMd, the fibers were fully spared in Mk-Le ($99.5 \pm 5.2\%$) when compared to the control. The three remaining animals showed a significant loss of 40% in Mk-Pa ($p < 0.001$), 80% in Mk-Jy($p < 0.001$), and 70% in Mk-Re ($p < 0.05$) (Figure 4.6c).

4.3.3 Registration of histology to MRI-atlas

Understanding the lesion impact on the descending tracts and the resulting phenotype, partially relies on having an understanding of the relative posi-

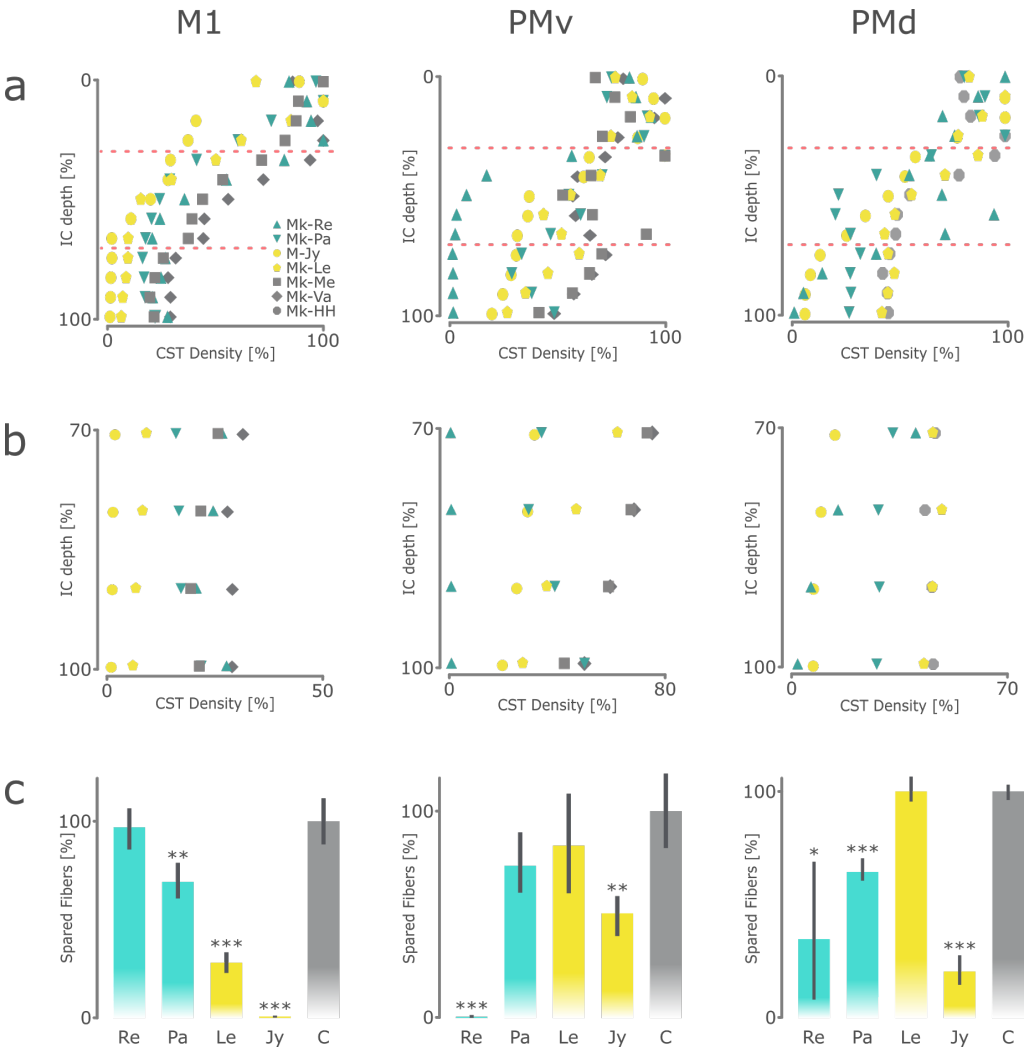

Figure 4.6: Lesion induced fiber loss of the corticospinal tract The density of the corticospinal tracts throughout the internal capsule (IC) are displayed with the estimated tract sparing compared to intact controls. The data for each injected cortical area: M1, PMv and PMd are shown in columns 1 to 3 respectively. (a) Depiction of the density evolution throughout the IC, normalized by the respective maximal density. The tracts are displayed with the most dorsal aspect of the IC as 0 and the most ventral part at 100, corresponding to the most dorsal aspect of the substantia nigra. The maximal lesion extent is indicated by the dashed red lines (b) Density evolution below the maximal lesion extent used to approximate the remaining fibers below the lesion level. (c) The estimated Fiber sparing, calculated according to the remaining density below the lesion, normalized by the control animals designated as C (Mk-Va, Mk-Me and Mk-05). The significance towards the control is indicated above the individual bars (***: $p \leq 0.001$, **: $p \leq 0.01$, *:$p \leq 0.05$, paired t-test, post-hoc corrected)

tioning of said structures. However, macaque brains can vary considerably in both size and shape, thus creating variances in the localization of substructures and tracts. In order to obtain a more unified readout and keep the precision obtained by the histological analysis, the histological slices were registered to an MRI atlas. A three step procedure was implemented to overcome this challenge: (1) forming a volume from the analyzed histological slices, (2) aligning the histological volumes to the post-mortem MRI scans, and (3) aligning the post-mortem scan to an MRI atlas (Figure 4.2).

Only the medial part of the injected or lesioned hemispheres were used in the histological analysis. To obtain a histological volume that could be used for registration with the post-mortem MRI, one histological image series was used per animal. In a pre-processing pipeline, imaging artifacts and non-tissue areas were removed, and the images were downscaled to match the MRI resolution. The obtained images were then recursively aligned to each other, by applying two pairwise registration methods in sequence: a rigid followed by a b-spline registration. The resulting volume was then saved in the NIFTI-file format in order to be used with standard MRI-alignment programs and pipelines.

The histological volume was then aligned to the individual post-mortem structural MRIs. As only one hemisphere could be histologically processed and imaged, the alignment was done masking the unused hemisphere. The alignment was achieved, by employing FSLs linear FLIRT alignment algorithm (Woolrich et al., 2009).

As a final alignment, the individual post-mortem MRIs were then registered to a common MRI atlas: the *M. fascicularis* atlas of the Montreal Neurological Institute (MNI, Frey et al. (2011)). Adequate alignment was achieved using FLIRT after skull-stripping the atlas.

The transformations received from each of the three steps were then concatenated and applied to all the data and masks collected in the histological analysis: the lesions, descending fiber tracts, injection sites, and marked brain structures. This data-set was then used for the further group analysis in a unified atlas space (Figure 4.7a).

The descending tracts showed clear overlap within the same tracts, while having a distinct topography while descending through the IC, with M1 descending rostrally to the PM fibers. However, the relative position of the ventral and dorsal parts of the PM varied between animals with Mk-Le and MK-Pa showing almost complete overlap, and others such as Mk Jy showing a clear separation. The position in the IC tends to correlate

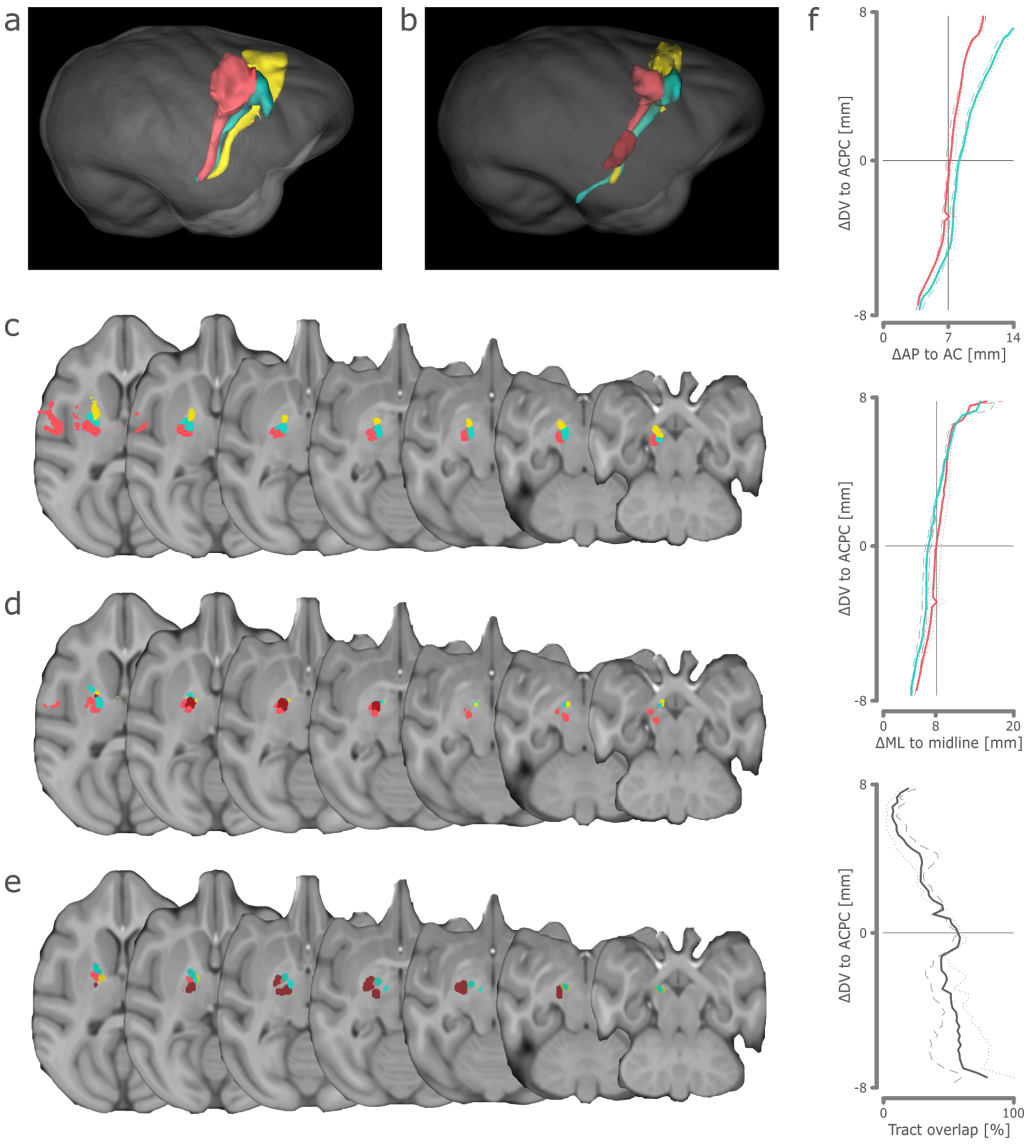

Figure 4.7: Corticospinal tracts in the MNI Atlas The corticospinal tracts of M1 (red), PMv (cyan) and PMd (yellow) registered to the reference MNI *M. fascicularis* atlas (Frey et al., 2011). The (a) intact cortico spinal tracts and the (b) interrupted tracts shown in Mk-Le. The axial series of the descending tracts in the (c) intact, (d) mild and (e) moderate groups, in descending order from dorsal to ventral. The lesions are displayed in dark red. (f) Atlas based analysis of the intact descending fibers in coronal (top) and the sagital plane (middle), as well as their volumetric overlap of PMv and M1 (bottom) in atlas space. The normalized lesion plan is indicated by the crossed lines.

with the relative position of the cortical areas in the rostro-caudal direction (Figure 4.7c-e).

The path of M1 and PMv were analyzed in the control animals, to gain insight into the effects of the lesion position. In this study, the position was determined by the extrapolation of data in *M. mulata* (Morecraft et al., 2002). This position could be confirmed and refined, using the normalized atlas space. A lesion placement $7mm$ posterior to the anterior commissure, and $8mm$ lateral of the midline at AC-PC level is likely to produce a maximal lesion of the descending M1 fibers. The amount of lesioned PM cortex CST is then determined by the depth along the dorso-ventral direction, with a more ventral lesion producing a more profound impact on both areas' CSTs (Figure 4.7 f).

4.3.4 Remaining connections in the spinal cord

The descending upper motor tracts ultimately terminate in the spinal cord. The innervation amount and pattern of the remaining tracts post lesion plays a key role in the expected clinical outcome. To investigate these tracts the spinal cord analysis was split into two parts: (1) the descending tracts in the white matter and (2) the termination pattern in the gray matter. Both kinds of analysis were proceeded by a registration of the spinal cord images to a common spinal cord atlas, to cope with the variances in individual anatomy.

At the time, no species-specific atlas of the spinal cord in *M. fascicularis* has been published. To overcome this problem, an atlas of the closely related *M. mulata* was taken and manually reformed to fit a representative section of Mk-Va at each spinal segment, ranging from C1 to T2. The obtained segmentation maps were then used as a template for all further analysis. In order to fit the spinal cord images of all animals to the obtained template, they were automatically segmented into gray- and white-matter. The segmented images then underwent a pairwise affine registration process to the atlas (Figure 4.8a,b).

For the white-matter analysis, the descending fibers were automatically segmented using intensity thresholding and then averaged per spinal segment. As expected, there was a visible decline in spinal projections correlating with the disruption seen at the IC level. However, when analyzing the white matter alone, there was no distinction in innervation pattern but, instead, a proportional decrease over the whole length of innervation (Figure 4.8c).

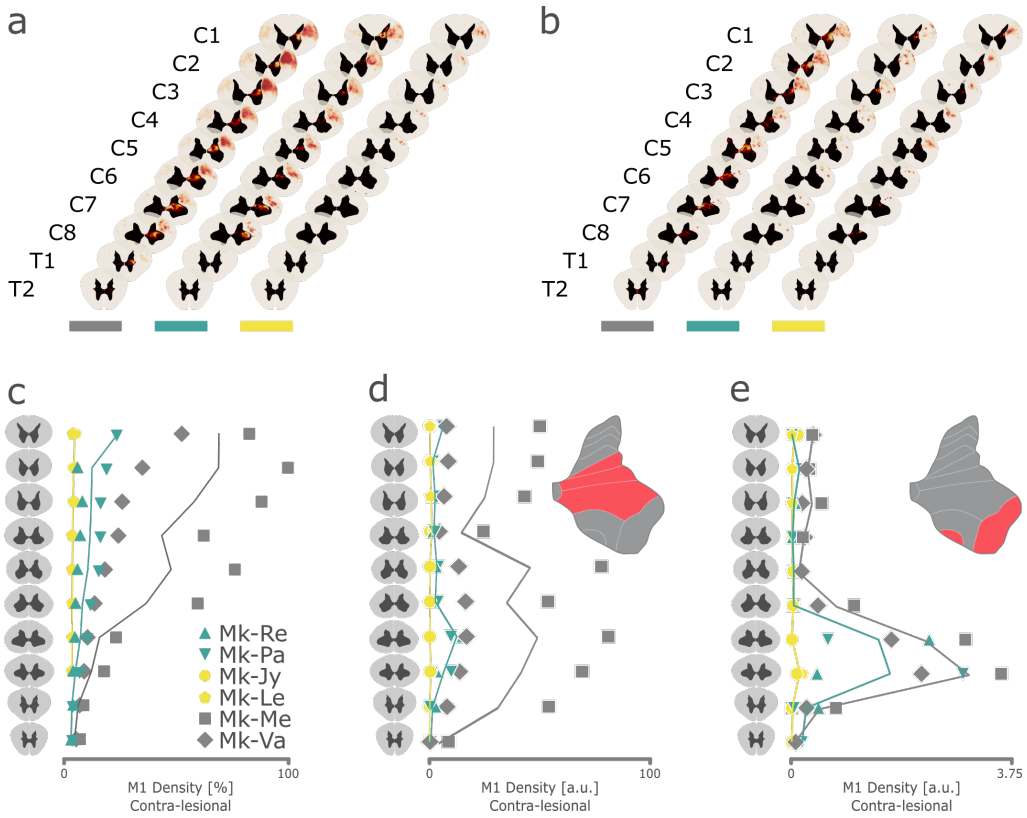

Figure 4.8: Corticospinal tracts in spinal cord The descending corticospinal tract's density in the white matter and the spinal laminas of the gray matter are displayed. Density maps of (a) M1 and (b) PMv projections in the spinal atlas series of are displayed for the intact (gray), mild (cyan) and moderate (yellow) lesion groups. The summed and normalized densities in each segment are displayed. (c) Quantification of the projections of M1 throughout the white contra-lesional white matter, normalized by the spared fiber density in the internal capsule. (d) Normalized density of the axonal terminations in the intermediary zone (spinal laminas V-VII), where mostly di-synaptic connections are made. (e) Normalized density of the axonal terminations in spinal lamina IX, where mono-synaptic connections are prevalent.

To cope with the high auto-fluorescence observed in the gray matter of monkeys, the fluorescent signal of the viral stains was further amplified using a fluorophore specific histological assay (Methods 4.2.3). The neurons on the resulting images were then automatically segmented using pixel classifiers (Methods 4.2.5), before the sections were registered to the atlas and averaged between the spinal segments. The terminations in each lamina were then calculated within each lamina mask provided by the reference atlas. In the intact animal (Mk-Va and Mk-Me), the M1 projections showed a pronounced innervation increase in the intermediary zone of the gray matter, at the spinal levels C5 to T1. Lamina IX showed a similar pattern albeit only starting at C6 and peaking at C7 and C8, the spinal level innervating the hand. The animals in the mild lesion group showed a marked but even decline in innervation at the intermediate laminas compared to the control. In the mono-synaptic lamina IX the termination density was better retained, and still showed an increased density at segments C7 and C8. Corresponding to the fiber loss in the internal capsule of the moderate group, there were very little to no terminations to be found in the Spinal segments C1 to T2 (Figure 4.8d,e).

4.4 Discussion

To determine the anatomical impact of lesions or interventions in a clinical setting, a wide array of techniques is employed, ranging from MRI and computer tomography to intraoperative electrical stimulation. These practices have led to a deep insight into the state of the health of the investigation's subjects, and have often been the starting point for new interventions that are now routinely in use. However, when it comes to these imaging techniques, many of them lack in resolution that can be achieved. The search for clinical markers which reliably predict the functional recovery potential of subcortical stroke patients has been an active field of study for many decades, but has nevertheless only brought limited improvements to the amelioration of patients motor function recovery processes (Hayward et al., 2016; Krakauer and Carmichael, 2017). An increase in imaging resolution might be the solution to finding such predictive markers, by piecing apart the contribution of different neuronal tracts affected by such a lesion, paving the way for future interventions.

In this chapter an analysis of the impact of a subcortical stroke on the descending tracts of three motor cortical areas (M1, PMv and PMd) was described. On the following pages the merits and challenges of multi color tracing in non-human primates are discussed, followed by a brief evaluation of the fiber quantification methods, as well as the procedure of histological slice registration to an MRI atlas

4.4.1 Tri-color staining in lesioned and implanted non-human primates

In this chapter, a histologic approach of tracing three likely candidates in determining the recovery potential after a subcortical stroke, was described (Liu and Rouiller, 1999b; Schulz et al., 2017a). M1, PMv and PMd, were injected with anterograde neuronal tracers in order to determine the remaining connectivity after a lesion in the internal capsule. The tracer injections took place after the completion of the kinematic assessment period (Chapter 3).

In order to trace three different structures in a single animal, tracers with different chemical binding sites or fluorescent properties have to be introduced. In this study, two viruses (AAV-8-CAG-drComet and AAV-5-CAG-gComet) as well as BDA, were used. Chemical tracers and viruses function fundamentally differently from one another in both uptake and mode of amplification, making accurate quantitative comparisons between them

difficult to impossible (Petrosyan et al., 2014; Watakabe et al., 2015). The viruses were chosen for their exceptionally good elucidation of axons. However, at the time, the green and red color variants existed only in two different viral substrains: adeno asociated virus (AAV) 5 and 8. These strains are known to have different transfection efficiencies in specific cell types and species (Petrosyan et al., 2014; Watakabe et al., 2015). This difference is further amplified by the different fluorophores, and their associated fluorescence pattern (Piatkevich and Verkhusha, 2011). Taken together, making quantitative comparisons between the tracers would be dubious at best. As for the employed anatomical location and relative, within-tracer analysis, the combination of multiple sources of fluorescence was thought to be adequate.

During the histological assessment, a relatively high variance in expression volume, not accounted for by the variance in injected tracer became apparent. There are two main factors that might play a role in this finding: The previous explantation of cortical arrays, and the lesion-induced cell death of the interrupted fibers. As the animals were previously implanted with cortical micro-electrode arrays (Utah Array, Blackrock, USA), the interventions were scheduled on the same day as the explantation procedure. During this procedure, great stress is put on the cortical tissue as the shanks are extracted from it, in some cases severely damaging or extracting tissue at the implantation site (Woeppel et al., 2021). In such cases, the injections were administered at more shallow injection depth and around the implantation site. Nevertheless, the change in cellular integrity, and especially the reduction of cortical volume, is likely to have a major impact on the absorption and expression of the viral and chemical tracers (Wang et al., 2014). The lesion itself could also account for some of the experienced inconsistency, as the white matter stroke is likely to induce an amount of retrograde degeneration processes, leading to cell death in the cortical areas of the affected neurons (Wei et al., 2019). The weight of these processes, in the presented case remains unknown. In case of future investigations, where similar experimental paradigms are applied, the trade-off in histological reliability gained by injecting non-implanted tissue and the acquisition of cortical data must be duly considered.

4.4.2 Brain atlas based analysis of the corticospinal tract

Mammals such as humans and primates are gyrencephalic, meaning their brain has a complex folded structure in order to vastly increase the cortical surface and, thus, computational power (Sun and Hevner, 2014). As these

structures progressively grow until reaching adulthood, their general layout stays the same, however, there remain relatively large variations between individuals of the same species. In order to compare functional as well as pathological characteristics between individuals, these variances must be taken into account. In the case of MRI acquisitions commonly used in clinical settings, these challenges have been addressed by linear and non-linear registration techniques, aligning similar structures to another image series or an averaged atlas brain. In order to obtain accurate results, these techniques heavily rely on the 3-dimensional contrasts that MRI imaging supplies. In the case of a traditional histological approach of sectioning tissue into thin slices, staining, and ultimately quantifying the target of inquiry, the alignment in the 3rd dimension is lost. The realignment of the analyzed slices has long posed a challenge that has recently seen very promising advances, resulting in automated tools for registration in smooth brained rodents (Xiong et al. 2018, ABBA pipeline (unpublished)). In primates, on the other hand, no such tools have yet been published. Inter animal comparisons are either done by the expert-based interpretation of the structures, or manual realignment of the acquired images. As part of this study, a semi-automated tool for the realignment of histological slices, and the subsequent registration to a species specific MRI atlas was developed. The described method is further able to achieve this registration with partial sections of the brain. In the case of this study, the slices of 15% of a single hemisphere were needed to achieve good registration results.

The obtained registration results allowed for a robust comparison between the descending tracts of the motor cortex and their topography within the IC, in both the intact and lesioned state. The results confirm that the general findings previously published by Morecraft et al. (2002) also hold true in *M. fascicularis*. As the previous study only reported descending tracts from the dorsal PM regions, the variations in descending topography and their varying rostro-caudal arrangement could not be corroborated. It can be speculated that observed positional reversal mirrors the rostro-caudal separation of the dorsal and ventral PMs in the cortex, however, with the current number of animals this could not be confirmed. The presence of variable positioning in the IC of these tracts however, indicate that a lesion in the location of the IC's genu is likely to affect the general projections of the PM, without a clear separation of the cortical areas. The intermingling tracts of PM seem to correlate findings in human tractography studies reporting either close to full overlap between the two areas (Schulz et al., 2012) or a clear separation between their descending tracts in the IC (Boccuni et al., 2019), suggesting the observed variance is also present in other

species. Furthermore, the shape of the IC, and the coalescence of the tracts within, make even small lesions in its ventral part likely to ablate both M1 and PM projections, leading to profound motor deficits (Chapter 3).

4.4.3 Remaining motor corticospinal tract after a subcortical stroke

The internal capsule forms the most direct bridge between many cortical areas and the spinal cord. In the dorsal aspect, it functions not unlike a funnel, collecting the descending fibers and forming a topologically organized conduit. It then travels further ventrally, in an oblique orientation to the axial plane. In the case of the motor cortical CST, it traverses around $8mm$ in the rostro-caudal direction, between entering and exiting the IC (Morecraft et al., 2002). Thus, if traditional coronal or sagittal histological preparations are used, the tract analysis must include at least $1cm$ worth of tissue to yield reliable results. In order to estimate the impact of the induced subcortical lesions on the remaining corticospinal tracts originating from M1, PMv and PMd, a relative analysis of the decline in fiber density, as they pass through the internal capsule was developed. As there are many subcortical structures surrounding the internal capsule, some of their innervating fibers partially descend through the internal capsule. Furthermore, CST fibers form collateral branches which interface with these structures as well. Thus, to estimate the number of fibers being interrupted by the induced lesion, a simple in-take and out-put analysis proves inadequate, as there is an innate decline in fiber density, even in intact subjects. As a solution to this problem, a relative approach was considered, taking into account the rate of density change as well as the fraction between the maximal fiber density and the 'density plateau' observed in the lower parts of the IC. To further diminish the change in density fluctuations, a direction based clustering method was implemented. The goal of this method was to consider only neurons following the local directionality of the CST in the analysis, while excluding deviating neurons. By combining these two concepts, a robust and noise resistant method for the estimation of fiber loss throughout the internal capsule was achieved.

The analysis of the spared fibers confirmed that the interruption of M1 tracts have the most profound impact on the initial impairment and delay to recovery. Whereas individuals with significant but incomplete loss in fiber density showed a delayed functional recovery and the reliance on compensatory strategies, the complete loss of M1 fibers observed in the severe group led to a permanent disability (chapter 3.3.2). This apparent

hard threshold on CST integrity has also been widely reported in human studies (Schulz et al., 2012; Byblow et al., 2015; Feng et al., 2015). On the other side of the spectrum, Mk-Re with a non-significant change in M1 integrity showed a quick functional recovery within the first weeks, as well as no discernible alteration in movement quality analysis (chapter 3.3.4). The monkey had a profound decrease in PMv fibers as well as a decrease in PMd density, accompanied by a lesion size inside the IC comparable to the other, more impaired individuals, which should conceptually result in similar CST integrity. This discrepancy between CST integrity and functional recovery further highlights the need for highly resolved biomarkers in order to have the chance of resolving mild and moderate impairments with recovery predicting imaging techniques (Prabhakaran et al., 2008; Schulz et al., 2012; Winters et al., 2015; Feng et al., 2015).

The observed, proportional loss in termination density in the spinal cord then correlated with both the density loss observed in the IC, as well as the observed recovery. When it comes to individual spinal lamina density, the decline in connections is consistent with the loss of terminations in the white matter. Similar decreases in white matter integrity, after a white matter ablation, have previously been reported in rhesus monkeys (Terashima, 1981). From the CST descending fibers around $80-90\%$ of the connections in the spinal cord innervate interneurons in the medial zone (spinal lamina V,VI and VII), and only $10-20\%$ represent cortico-motorneuronal connections (Lemon, 2019). There was no discernible spinal lamina experiencing an above average decline in connections. In the intact and the mild group an increased termination density in segments C5 to T1 was observed, consistent with previous tracing studies in NHP (Dum and Strick, 1991, 1996). The loss of hand dexterity was strongly correlated with the decrease in termination density in lamina IX in the spinal segments C7 and C8, the termination area for mono-synaptic CST terminations controlling the hand (Witham et al., 2016) Generally these results in combination with the general kinematic analysis (Chapter 3) correlate well with the previous assessment of the main marker for stroke recovery being CST damage (Favre et al., 2014). The results further suggest that the lesion location, and the resulting interruption of different sub-CSTs, is the deciding factor for recovery potential. While major interruptions of PM fibers do in fact cause a decline in performance, their interruption seems to have a minor effect when compared to M1 interruptions (Mk-Re, Chapter 3).

4.5 Limitations

In this study the variance of tracer efficiency was substantial, varying with both chemical as well as viral substances. As discussed (Section 4.4.1), the variance likely originates from a combination of lesion induced cell death and cortical trauma after the cortical array explanation. Due the variability in both the lesion severity and the amount of cortical damage in each animal, on top of the low number of animals in this study, the separation of these effects is challenging at best. Further studies, examining the impact of IC lesions on the upstream effect on cortical areas should therefore be conducted with less invasive recording techniques.

The registration between two images or volumes, especially in the case of different modalities, depends on a correlation of contrasts between the two series. As structural MRI produces contrast between white and gray matter areas, a similar or inverse intensity is required to be present in the histological preparations. While the employed DAPI stain worked very well for this purpose, other histological assays, such as DAB or pure tracing assays, would prove far more challenging for alignment. In this case, only the outline of the cortex could be reliably used for an alignment, resulting in a devastating loss in detail. Registration would be further complicated by the large tissue distortions often seen in the cortical areas, due to the lack of structural integrity in areas of sulci and gyri. A non-compatible staining assay could still be employed, if adjacent sections with a compatible modality are available. The highly similar sections could first be aligned to each other, and then ported to MRI space in a subsequent step.

4.6 Future perspective

4.6.1 Integration of atlas registered histological data within a standardized framework

Comparison and reproducibility of findings between studies and laboratories is notoriously problematic (Baker, 2016; Miyakawa, 2020). While this crisis has been attributed to factors ranging from lack of statistical power to scientific misconduct, one of the deciding factors is a lack of accessibility to the raw and processed data the studies are based on. In the case where these data are available, they come in various formats, often incompatible with the currently employed pipelines. A move to storing the used raw and processed data as well as appropriate conversion tools to create a standardized frame work, such as the MNI brain atlas, might prove to be a first

step in the direction of improved reproducibility. Especially in the field of primate research, where animal numbers are very low and labs are sparse, this could provide an invaluable resource for field overreaching assessments.

4.6.2 Development of predictive tract interruption

As described in previous chapters, MRI guided lesion planning provides a personalized surgery plan to help optimize consistent placement of the lesion, or similar interventions. However, inter-individual differences in the local anatomy provide a challenge for the consistent targeting of structures(Miocinovic et al., 2007; Ose et al., 2022). The combination of the presented data of the intact descending tracts, as well as the tract interruption and lesion location, allows for the development of a lesion simulation tool. Such a tool would simulate multiple lesion position and their intersection with each of the traced tracts, and thus provide a pre-surgical estimation of the tract interruption. As the appropriate lesion location for the current research question is found, the standardized planning can then be transformed into the personal MRI of each subject, providing a way of automating and optimizing the surgical planning. The potential gain in reproducibility could thus led to more homogeneous cohorts and possibly reduce the number of animals needed and the processing time.

4.7 Conclusion

Within this chapter, the corticospinal tracts originating in three motor cortical areas were investigated in both intact as well as after a subcortical lesion. A method to selectively quantify the internal capsule traversing tracts was developed and used to quantify the tract specific loss of fiber density induced by the lesion. The remaining tracts were followed into the spinal cord, where their residual termination pattern was investigated. Furthermore, a semi-automated tool for the registration of partial histological brain sections into a unified MRI space was devised, providing a solid basis for atlas-based analysis and the incorporation in DTI and fMRI based studies, by providing microscopy level resolution and detail for the relatively large and varied non-human primate brain.

Chapter 5

Discussion and Perspectives

The work presented in this thesis provides a novel clinically relevant model of a unilateral sub-cortical stroke in non-human primates (NHP). The model permits the precise, MRI guided induction of a focal lesion in the internal capsule, interrupting the descending motor corticospinal tract, and specifically impairing the upper limb.

To achieve the necessary precision, a maxillary retention system was developed. A personalized maxillary mold was used to augment the traditional stereotactic frame, locking the animal into the same exact position during imaging and surgical interventions. With the implementation of this system, the placement precision could be restricted to sub-millimeter variance between interventions taking place even months apart (chapter 2.3.1). This frame work provided a robust platform, allowing the implementation of complex, longitudinal studies, including non-MRI compatible, chronic, neuronal and muscular recording systems.

Combining personalized MRI guided surgical planning with the maxillary retention framework, a unilateral thermo-coagulation lesion was induced in the internal capsule. The lesion targeting the descending corticospinal tract (CST, Morecraft et al. 2007) of the primary motor cortex (M1, hand area), produced distinct impairment in the animals' reaching and grasping abilities (chapter 3.3.2).

The functional recovery was analyzed with an array of six upper limb performance assessments; revealing three distinct levels of impairment, mirroring deficits seen in human stroke patients (Cheung et al., 2016; Krakauer and Carmichael, 2017). The mild impairment group showed functional recovery within the first month and regained dexterous movement control, allowing them to perform a precision grip. The moderately impaired group only regained the general grasping control, having permanently lost the ability to perform dexterous hand movements. No functional recovery was observed in the severely impaired group. However, flexor-synergy like movements could be observed, mirroring symptoms seen in severe stroke patients, but not previously described in animal models (Cheung et al., 2016).

By analyzing the underlying kinematic strategies during and after the recovery period, it could be shown that even in mildly lesioned animals showing full functional recovery, a significant shift in movement patterns occurred. This provides evidence for the major role of compensatory strategies in the reported functional recovery ().

For the histologic analysis of the anatomical changes induced by the lesion, the corticospinal tracts originating in M1, as well as the ventral (PMv) and dorsal (PMd) pre-motor cortices, were traced. To gain insight into the relative location of the lesions and the CSTs, a semi-automated tool for the registration of the histological sections into the MNI standard space for *M.fascicularis* was developed. The combined space allowed insight into the relative positioning of the induced lesions and could confirm the relative location of the descending tracts, with M1 projections traversing caudal to both PMv and PMd (Morecraft et al., 2002). As the fibers descending through the internal capsule form many collateral connections and further connect to IC adjacent structures, an algorithm specifically quantifying the CST fibers was devised. The resulting data showed that the observed impairment grossly correlated with the degree of lost density in M1 fibers, while PMd and PMv damage played a minor but important role, confirming prior findings of tractography studies in stroke patients (Riley et al., 2011; Schulz et al., 2015, 2017a; Boccuni et al., 2019). The remaining tracts were followed into the spinal cord and their residual termination patterns were investigated, revealing a proportional decline in axonal density in the white matter and gray matter terminations, providing evidence for an even decline in both mono- and di-synaptic connections in the spinal cord. The loss of terminations in the lower cervical level also correlated with the loss of functional control.

In summary, with the provided model, the basis for a mechanistic inves-

tigation of the fundamental changes in cortical activation and recovery mechanisms have been laid. Future avenues for their investigation and the application of the findings will be discussed in the following paragraphs.

5.1 Neural correlates after sub-cortical stroke

Changes in cortical activity following stroke have been widely reported in humans (Traversa et al., 1997; Grefkes and Fink, 2011) and animal models (Ramanathan et al., 2018). Where in smaller cortical lesions, the ipsi-lesional areas are reported to be hyper-activated, larger lesions tend to produce bi-hemispheric up-regulation (Grefkes and Fink, 2014). The reversal to normal activation levels with time, supports the idea of lesion initiated plastic changes in the brain (Ward et al., 2015). Further, in the case of subcortical stroke, the integrity of cortico-cortical connections between PM and M1 have been shown to be positively correlated with recovery rates (Schulz et al., 2015; Boccuni et al., 2019). The exact mechanisms and the manner of cortical interaction, as well as the functional relevance of the reported regulated states remain enigmatic. In the current lesion model, the implantation of intra-cortical micro-electrode arrays (Figure 5.1a) in 5 cortical areas (ipsi-lesional: M1, PMv, PMd, contra-lesional: M1, PMv; Methods in appendix 5.3) attempted to elucidate parts of these questions. The findings of the multi-unit analysis correlated with previous reports in humans: an ipsi-lesional up-regulation in cortical activity, combined with an enhanced functional connectivity and cortico-kinematic correlation could be reported in the mild impairment group. In the group with moderate impairment, a shift towards contra-lesional control was seen (Figure 5.1a,b). This data suggests that the increase in cortical activity seen in patients is indeed of a functional nature rather than a pathological byproduct (Grefkes and Ward, 2014). Further evidence for the existence of a highly plastic phase was found in the pronounced hyperactivity and hyper connectivity during the acute phase, which receded and settled into specific, up-regulated cortico-cortical connections. A correlation between the reported neuronal changes and the kinematic impairment was present as early as the first day post-lesion. This correlation persisted throughout the chronic phase as well (Figure 5.1c). Moreover, the regional cortical changes were significantly correlated with the remaining CST fiber quantified in the presented histological assessment.

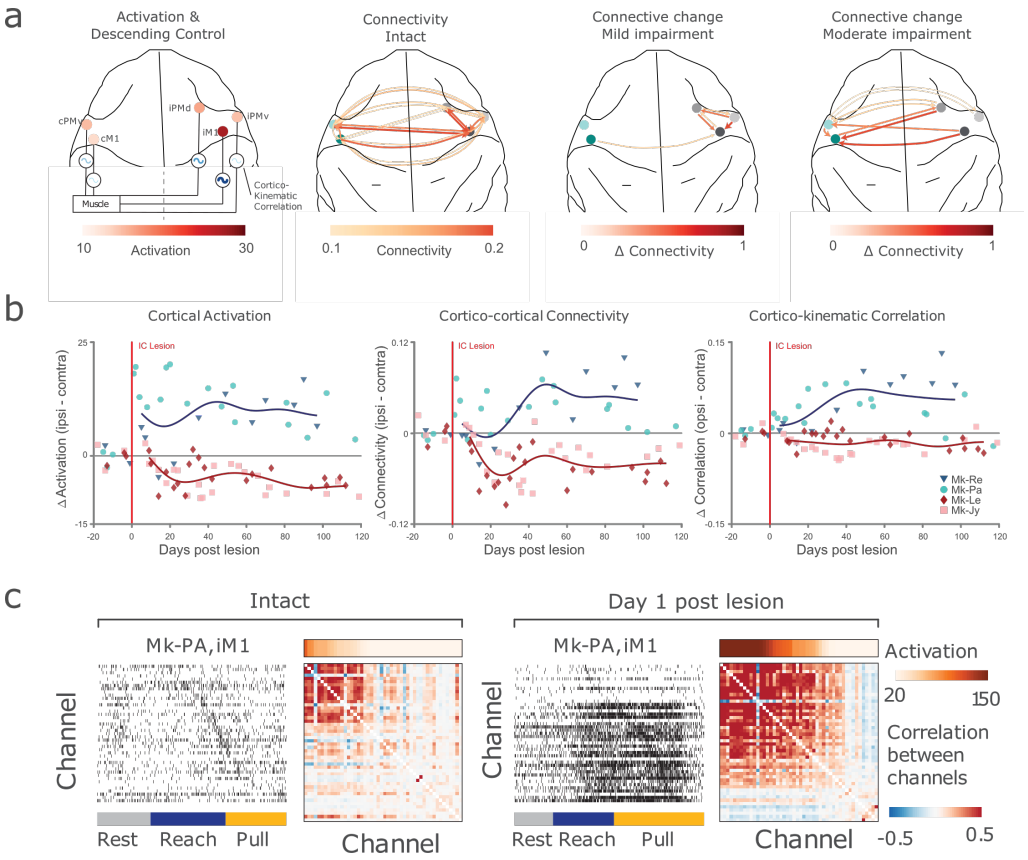

Figure 5.1: Neural correlates after subcortical stroke A summary of the observed changes in activation and connectivity after subcortical stroke. (a) Depiction of the healthy cortical control and activation contrasted with the connective changes observed in mildly and moderately impaired animals. The amplitude of connective change is depicted by the increase in saturation and size of the connective arrows. (b) Depiction of the time-resolved cortical changes, displayed as the difference between ipsi- and contra-lateral activity. (c) Depiction of the tuning curves and neuronal spiking correlations in Mk-Pa. Figures adapted from cortical analysis by Dr. Shiqi Sun.

5.2 Mechanistic approaches to elucidate primary brain regions driving recovery

The pre-motor areas in the recovery process after subcortical stroke have been suggested as primary candidates in aiding the recovery of motor function after stroke (Liu and Rouiller, 1999a; Riley et al., 2011; Schulz et al., 2015, 2017a; Boccuni et al., 2019). However, the degree of their functional involvement remains unknown. In the past, re-lesioning experiments have been used to assess exactly this question (Rouiller and Olivier, 2004). In a typical re-lesion experiment, the animals are lesioned and then left to recover until they reach a behavioral plateau. A second lesion is then introduced, where the researchers determine the likely origin for the observed recovery. Ultimately, quantifying whether the secondary lesion reverted the observed functional gain. There are, however, two major drawbacks to this approach: (1) irreversibility and (2) off-target effects. With the induction of a secondary lesion, only one area of interest can be targeted, as the resulting lesion will permanently alter the underlying anatomy. The second major concern with inducing a second lesion is that it might actually boost the recovery. Multiple studies have shown that the induction of a secondary lesion 're-opens' the window of plasticity, allowing the brain to adapt to both the second as well as the first induced lesion (Kapur, 1996; Zeiler et al., 2016).

A possible solution to both of these concerns is the introduction of transient inhibition methods, which are nor without their own inherent challenges, but which may be overall more beneficial than re-lesioning studies.

For cortical inhibition, one of the most prevalently used pharmacologic agents is Muscimol. The GABA receptor agonist (Eugster and Takemoto, 1967; Johnston, 2014) has the ability to transiently reduce the cortical output by activating the inhibitory GABA-ergic sub-population of neurons (Martin, 1991; Yamauchi et al., 2000). It has been used in various studies in NHPs to assess the effects of transient inhibition in both healthy (Mason et al., 1998; Brochier et al., 1999; Matsumura et al., 1991; Kurata and Hoffman, 1994) and in lesioned states (Liu and Rouiller, 1999a; Hoogewoud et al., 2013). Due to the transient nature, it allows the screening of multiple candidate areas over the course of subsequent days to allow for an adequate flush-out period. The fact that Muscimol is injected intra-cortically to achieve its effect is, on one hand, phenomenal for precise targeting of the target structures but, on the other hand, requires the cortex to be exposed. The prolonged exposure can be mitigated by implantation of an injection

chamber which in itself may pose a constant risk of infection.

As part of this project, a Muscimol inhibition pilot study targeting M1, PMv, and PMd before and after stroke was launched with the collaborating laboratory in Beijing. Unfortunately this was just as the pandemic shook the world, and was thus postponed until further notice.

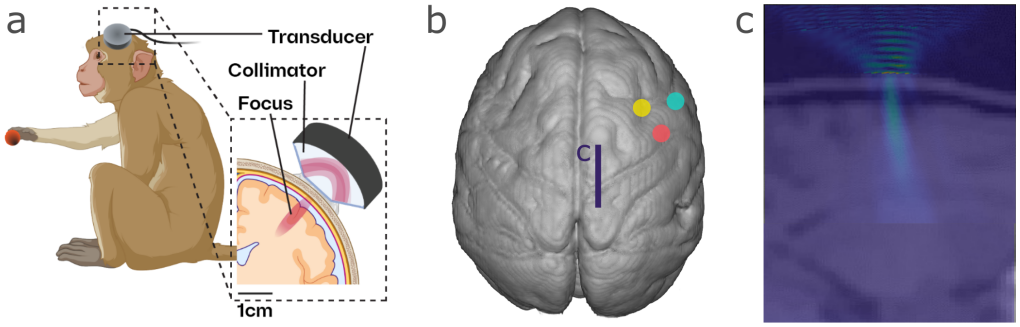

Figure 5.2: Mechanistic insight into subcortical stroke using inhibitory focused ultrasound stimulation A summary of the planned focused ultra-sound stimulation paradigm. (a) Schematic depiction of the focused ultra-sound stimulation setup during a robotic object presentation task. The stimulation area in the brain is indicated in red. (b) Depiction of the targeted inhibition sites: primary motor cortex (red), ventral pre-motor cortex (cyan), and dorsal pre-motor cortex (yellow). The blue line indicates the location of the sagittal secion shown in (c) A simulation of the predicted inhibition focal area, using CT and MRI data to estimate the corresponding skull and brain attenuation. The focal area is depicted in green. Figures adapted material provided by Dr. Charles Latchoumane and Ruijia Wang.

A major drawback of many interventions used to inhibit cortical activity is their need for invasive procures. Over recent years a new technology for non-invasive cortical inhibition has been evolving (Fishman and Frenkel, 2017). Focused ultrasound stimulation (FUS) has been shown, on the one hand, to have the ability to transiently activate or inhibit neuronal tissue depending on the chosen frequency and power (King et al., 2013), and on the other, to produce lesions in deep structures without the need for invasive access. The technology has thus found applications in the clinical environment ranging from thermo-coagulation for thalamotomy (Elias et al., 2018) and treatment of essential tremor in Parkinson's disease (Magara et al., 2014), to transiently opening the blood brain barrier in Alzheimer's disease patients (Lipsman et al., 2018).

As it's effect size can be tuned to achieve a relatively small effect size this method has been proposed as a promising candidate for mechanistic studies in NHP models (Zhang et al., 2021). Indeed, as the method does not require

invasive procedures to transiently inhibit or activate the cortical regions, this would make an optimal candidate for a longitudinal mechanistic study (Verhagen et al., 2019; Yang et al., 2021).

As a follow up to the current project, such a study has been launched. With the goal of transiently inhibiting the core cortical regions investigated during the presented stroke study. As in the presented project, the animals will be trained in multiple reach and grasp tasks, before a moderate impairment subcortical stroke is applied (Figure 5.2a). When the animals reach their recovery plateau, the actual mechanistic investigation will commence. M1, PMv and PMd will be transiently inhibited using the appropriate inhibitory stimulation sequence (Figure 5.2b). With the preliminary data collection, the simulations of the inhibition effects (Figure 5.2c), and the animal training well on their way, the prospects of quantifying the contribution of pre-motor areas to the observed recovery are promising.

5.3 Neuro-prosthetics to restore movement

As possible targets for rehabilitative targets are uncovered, the question arises how these now findings should be addressed in a therapeutic manner. In recent years, a diverse array of therapeutic interventions have been proposed and tested, ranging from rehabilitative interventions such as constraint induced movement therapy (Taub and Uswatte, 2003; Taub et al., 2013), and robot-assisted movement therapies (Lo et al., 2010; Bertani et al., 2017), to pharmacological (Chollet et al., 2011; Cramer, 2015) and stem cell based treatments (Kalladka et al., 2016; Steinberg et al., 2016). In addition to these interventions, multiple promising approaches using neuroprosthetic interventions might play a key role in finding efficient therapy models able to restore upper limb function after stroke. A few of these prospective avenues will be briefly discussed.

Guiding the plasticity phase through cortical modulation is an enticing prospect for stroke treatment. The concept is based on the hypothesis that stimulation of appropriate spared motor areas, in combination with the activation of their target muscles or brain areas, would lead to an enhancement of their connectivity through Hebbian learning, ultimately enhancing the synaptic density (Adkins-Muir and Jones, 2003; Plautz et al., 2003; Kleim et al., 2004). Various animal studies have reported an increased functional recovery, resulting from the combination of rehabilitative training with cortical stimulation in the peri-infarct zone (Adkins-Muir and Jones, 2003; Plautz et al., 2003; Cheng et al., 2014) as well as the contra-lesional hemi-

sphere (Teskey et al., 2003; Wahl et al., 2017). The direct translation of these findings into a therapeutic approach for stroke patients, however, yielded disappointing results, as clinical trials showed no differences in recovery between the treatment and control group four weeks after stroke (Levy et al., 2016). Despite the supportive stimulation before and during rehabilitative trains seeming only to have a minor effect on the functional outcomes in patients, there has recently been evidence for a possible alternate path of intervention by Jackson et al. (2006) and Nishimura et al. (2013). Instead of activating the termination target by voluntary movement production, these studies demonstrate plasticity increases by concurrent stimulation of both origin and endpoint, forming a bi-directional neural interface (Edwardson et al., 2013; Fetz, 2015). There is potential for these technologies to improve recovery after stroke in both cortico-cortical as well as corticospinal stimulation paradigms. As the integrity of cortico-cortical connections have been shown to have a positive correlation with the expected functional outcome after stroke (Bosnell et al., 2011; Schulz et al., 2012; Koch et al., 2016), the additional strengthening of these circuits via bidirectional stimulation might enhance the brain's innate recovery mechanisms. Likewise, the integrity of the corticospinal connections is pivotal to recovery. Additionally, a strengthening of connectivity at the location could be beneficial (Nishimura et al., 2013; Urbin et al., 2017; Liu et al., 2020; Urbin et al., 2021).

While subcortical strokes affecting the CST have been shown to cause a non-negligible amount of dieback in the interrupted neurons (Wei et al., 2019), the cortical regions remain functional (Grefkes et al., 2008; Grefkes and Fink, 2014). This leaves the potential for decoding neuronal activation in the disconnected brain regions to inform targeted and time-resolved stimulation of the spinal cord, peripheral nerves, or muscles, directly. Indeed, brain actuated functional electrical stimulation has been shown to improve the restoration of arm function in stroke patients (Biasiucci et al., 2018). Similar improvements could be seen with spinal cord stimulation, after spinal cord injury in rats (Bonizzato et al., 2018), and in paraplegic patients (Shokur et al., 2018). The stimulation of the cervical spinal cord has further been shown to be able to induce arm movement after spinal cord injury both in rodents (Sunshine et al., 2013) and primates (Barra et al., 2021). While cervical stimulation has only been shown to be feasible in producing coordinated arm movement, Badi et al. (2021) presented an intrafascicular peripheral nerve simulation paradigm, with the ability to evoke dexterous finger movements in non-human primates.

In combining the neuronal decoding at the disconnected cortical areas and

the movement restoring stimulation paradigms, a real opportunity to bypass the lost corticospinal tracts and restore functional control via brain-spine or brain-peripheral nerve interfaces is created.

Bibliography

Adkins-Muir, D. L. and Jones, T. A. (2003). Cortical electrical stimulation combined with rehabilitative training: Enhanced functional recovery and dendritic plasticity following focal cortical ischemia in rats. *Neurological Research*, 25(8):780–788.

Alaverdashvili, M. and Whishaw, I. Q. (2013). A behavioral method for identifying recovery and compensation: Hand use in a preclinical stroke model using the single pellet reaching task. *Neuroscience & Biobehavioral Reviews*, 37(5):950–967.

Amarenco, P. and Labreuche, J. (2009). Lipid management in the prevention of stroke: Review and updated meta-analysis of statins for stroke prevention. *The Lancet. Neurology*, 8(5):453–463.

Andersen, K. K., Olsen, T. S., Dehlendorff, C., and Kammersgaard, L. P. (2009). Hemorrhagic and Ischemic Strokes Compared: Stroke Severity, Mortality, and Risk Factors. *Stroke*, 40(6):2068–2072.

Appelros, P., Karlsson, G. M., Seiger, A., and Nydevik, I. (2002). Neglect and anosognosia after first-ever stroke: Incidence and relationship to disability. *Journal of Rehabilitation Medicine*, 34(5):215–220.

Ariñez-Barahona, E., Navarro-Olvera, J., Vega-Sosa, A., Esqueda-Liquidano, M., Muñoz-Cobos, A., Laredo-Gómez, J., Rivera-Arroyo, A., and Méndez-Viveros, A. (2017). Radiofrequency thermocoagulation in

chronic low back pain from the facet joints: Literature review. *Revista Médica del Hospital General de México*, 80(3):185–190.

Badi, M., Borgognon, S., O'Doherty, J. E., and Shokur, S. (2021). Chapter 13 - Cortical stimulation for somatosensory feedback: Translation from nonhuman primates to clinical applications. In Güçlü, B., editor, *Somatosensory Feedback for Neuroprosthetics*, pages 413–441. Academic Press.

Bailey, E. L., McCulloch, J., Sudlow, C., and Wardlaw, J. M. (2009). Potential Animal Models of Lacunar Stroke: A Systematic Review. *Stroke*, 40(6).

Baker, M. (2016). 1,500 scientists lift the lid on reproducibility. *Nature*, 533(7604):452–454.

Bala, P. C., Eisenreich, B. R., Yoo, S. B. M., Hayden, B. Y., Park, H. S., and Zimmermann, J. (2020). Automated markerless pose estimation in freely moving macaques with OpenMonkeyStudio. *Nature Communications*, 11(1):4560.

Baldwin, M. K. L., Cooke, D. F., Goldring, A. B., and Krubitzer, L. (2018). Representations of Fine Digit Movements in Posterior and Anterior Parietal Cortex Revealed Using Long-Train Intracortical Microstimulation in Macaque Monkeys. *Cerebral Cortex (New York, N.Y.: 1991)*, 28(12):4244–4263.

Bankhead, P., Loughrey, M. B., Fernández, J. A., Dombrowski, Y., McArt, D. G., Dunne, P. D., McQuaid, S., Gray, R. T., Murray, L. J., Coleman, H. G., James, J. A., Salto-Tellez, M., and Hamilton, P. W. (2017). QuPath: Open source software for digital pathology image analysis. *Scientific Reports*, 7(1):16878.

Barra, B., Badi, M., Perich, M. G., Conti, S., Salehian, S. S. M., Moreillon, F., Bogaard, A., Wurth, S., Kaeser, M., Passeraub, P., Milekovic, T., Billard, A., Micera, S., and Capogrosso, M. (2019). A versatile robotic platform for the design of natural, three-dimensional reaching and grasping tasks in monkeys. *Journal of Neural Engineering*, 17(1):016004.

Barra, B., Conti, S., Perich, M. G., Zhuang, K., Schiavone, G., Fallegger, F., Galan, K., James, N. D., Barraud, Q., Delacombaz, M., Kaeser, M., Rouiller, E. M., Milekovic, T., Lacour, S., Bloch, J., Courtine, G., and Capogrosso, M. (2021). Epidural Electrical Stimulation of the Cervical Dorsal Roots Restores Voluntary Upper Limb Control in Paralyzed Monkeys. Technical report, bioRxiv.

Bennett, M. R. and Hacker, P. M. S. (2002). The motor system in neuroscience: A history and analysis of conceptual developments. *Progress in Neurobiology*, 67(1):1–52.

Berger, M., Agha, N. S., and Gail, A. (2020). Wireless recording from unrestrained monkeys reveals motor goal encoding beyond immediate reach in frontoparietal cortex. *eLife*, 9:e51322.

Bertani, R., Melegari, C., De Cola, M. C., Bramanti, A., Bramanti, P., and Calabrò, R. S. (2017). Effects of robot-assisted upper limb rehabilitation in stroke patients: A systematic review with meta-analysis. *Neurological Sciences*, 38(9):1561–1569.

Biasiucci, A., Leeb, R., Iturrate, I., Perdikis, S., Al-Khodairy, A., Corbet, T., Schnider, A., Schmidlin, T., Zhang, H., Bassolino, M., Viceic, D., Vuadens, P., Guggisberg, A. G., and Millán, J. d. R. (2018). Brain-actuated functional electrical stimulation elicits lasting arm motor recovery after stroke. *Nature Communications*, 9(1):2421.

Biernaskie, J. (2004). Efficacy of Rehabilitative Experience Declines with Time after Focal Ischemic Brain Injury. *Journal of Neuroscience*, 24(5):1245–1254.

Binkofski, F., Seitz, R. J., Arnold, S., Classen, J., Benecke, R., and Freund, H.-J. (1996). Thalamic metabolism and corticospinal tract integrity determine motor recovery in stroke. *Annals of Neurology*, 39(4):460–470.

Blackwell, L., Emberson, J., Godwin, J., Peto, R., Buring, J., Hennekens, C., Kearney, P., Meade, T., Patrono, C., Roncaglioni, M. C., Zanchetti, A., and Collaboration, A. T. A. (2009). Aspirin in the primary and secondary prevention of vascular disease: Collaborative meta-analysis of individual participant data from randomised trials. *Lancet (London, England)*, 373(9678):1849–1860.

Boccuni, L., Meyer, S., D'cruz, N., Kessner, S. S., Marinelli, L., Trompetto, C., Peeters, A., Van Pesch, V., Duprez, T., Sunaert, S., Feys, H., Thijs, V., Nieuwboer, A., and Verheyden, G. (2019). Premotor dorsal white matter integrity for the prediction of upper limb motor impairment after stroke. *Scientific Reports*, 9(1):19712.

Boehme, A. K., Esenwa, C., and Elkind, M. S. (2017). Stroke Risk Factors, Genetics, and Prevention. *Circulation Research*, 120(3):472–495.

Bohannon, R. W. (2004). Adequacy of Simple Measures for Characterizing Impairment in Upper Limb Strength following Stroke. *Perceptual and Motor Skills*, 99(3):813–817.

Bonizzato, M., Pidpruzhnykova, G., DiGiovanna, J., Shkorbatova, P., Pavlova, N., Micera, S., and Courtine, G. (2018). Brain-controlled modulation of spinal circuits improves recovery from spinal cord injury. *Nature Communications*, 9(1):3015.

Bootin, M. L. (2006). Deep Brain Stimulation: Overview And Update. *Journal of Clinical Monitoring and Computing*, 20(5):341–346.

Borgognon, S. (2020). *Neural Population Dynamics in Premotor, Motor and Somatosensory Cortices during Locomotion in Primates*. PhD thesis, University of Fribourg.

Bosnell, R. A., Kincses, T., Stagg, C. J., Tomassini, V., Kischka, U., Jbabdi, S., Woolrich, M. W., Andersson, J., Matthews, P. M., and Johansen-Berg, H. (2011). Motor Practice Promotes Increased Activity in Brain Regions Structurally Disconnected After Subcortical Stroke. *Neurorehabilitation and Neural Repair*, 25(7):607–616.

Brinkman, C. (1981). Lesions in supplementary motor area interfere with a monkey's performance of a bimanual coordination task. *Neuroscience Letters*, 27(3):267–270.

Brinkman, J. and Kuypers, H. G. J. M. (1973). CEREBRAL CONTROL OF CONTRALATERAL AND IPSILATERAL ARM, HAND AND FINGER MOVEMENTS IN THE SPLIT-BRAIN RHESUS MONKEY. *Brain*, 96(4):653–674.

Brochier, T., Boudreau, M.-J., Paré, M., and Smith, A. M. (1999). The effects of muscimol inactivation of small regions of motor and somatosensory cortex on independent finger movements and force control in the precision grip. *Experimental Brain Research*, 128(1-2):31–40.

Brochier, T., Spinks, R. L., Umilta, M. A., and Lemon, R. N. (2004). Patterns of Muscle Activity Underlying Object-Specific Grasp by the Macaque Monkey. *Journal of Neurophysiology*, 92(3):1770–1782.

Brunnstrom, S. (1970). Movement therapy in hemiplegia. *A Neurophysiological Approach*, pages 113–122.

Buma, F., Kwakkel, G., and Ramsey, N. (2013). Understanding upper limb recovery after stroke. *Restorative Neurology and Neuroscience*, 31(6):707–722.

Burton, C. R. (2000). Living with stroke: A phenomenological study. *Journal of Advanced Nursing*, 32(2):301–309.

Buxbaum, L. J., Ferraro, M. K., Veramonti, T., Farne, A., Whyte, J., Ladavas, E., Frassinetti, F., and Coslett, H. B. (2004). Hemispatial neglect: Subtypes, neuroanatomy, and disability. *Neurology*, 62(5):749–756.

Byblow, W. D., Stinear, C. M., Barber, P. A., Petoe, M. A., and Ackerley, S. J. (2015). Proportional recovery after stroke depends on corticomotor integrity: Proportional Recovery After Stroke. *Annals of Neurology*, 78(6):848–859.

Caminiti, R., Borra, E., Visco-Comandini, F., Battaglia-Mayer, A., Averbeck, B. B., and Luppino, G. (2017). Computational Architecture of the Parieto-Frontal Network Underlying Cognitive-Motor Control in Monkeys. *eNeuro*, 4(1):ENEURO.0306–16.2017.

Carmel, J. B., Kimura, H., and Martin, J. H. (2014). Electrical Stimulation of Motor Cortex in the Uninjured Hemisphere after Chronic Unilateral Injury Promotes Recovery of Skilled Locomotion through Ipsilateral Control. *Journal of Neuroscience*, 34(2):462–466.

Chen, G. J. and Yang, M. S. (2013). The effects of calcium channel blockers in the prevention of stroke in adults with hypertension: A meta-analysis of data from 273,543 participants in 31 randomized controlled trials. *PloS One*, 8(3):e57854.

Cheng, M. Y., Wang, E. H., Woodson, W. J., Wang, S., Sun, G., Lee, A. G., Arac, A., Fenno, L. E., Deisseroth, K., and Steinberg, G. K. (2014). Optogenetic neuronal stimulation promotes functional recovery after stroke. *Proceedings of the National Academy of Sciences*, 111(35):12913–12918.

Cheung, D. K., Climans, S. A., Black, S. E., Gao, F., Szilagyi, G. M., and Mochizuki, G. (2016). Lesion Characteristics of Individuals With Upper Limb Spasticity After Stroke. *Neurorehabilitation and Neural Repair*, 30(1):63–70.

Chollet, F., Tardy, J., Albucher, J.-F., Thalamas, C., Berard, E., Lamy, C., Bejot, Y., Deltour, S., Jaillard, A., Niclot, P., Guillon, B., Moulin, T., Marque, P., Pariente, J., Arnaud, C., and Loubinoux, I. (2011). Fluoxetine for motor recovery after acute ischaemic stroke (FLAME): A randomised placebo-controlled trial. *The Lancet. Neurology*, 10(2):123–130.

Chua, N. H. L., Vissers, K. C., and Sluijter, M. E. (2011). Pulsed radiofrequency treatment in interventional pain management: Mechanisms and potential indications—a review. *Acta Neurochirurgica*, 153(4):763–771.

Cook, D. J. and Tymianski, M. (2012). Nonhuman Primate Models of

Stroke for Translational Neuroprotection Research. *Neurotherapeutics*, 9(2):371–379.

Cortes, J. C., Goldsmith, J., Harran, M. D., Xu, J., Kim, N., Schambra, H. M., Luft, A. R., Celnik, P., Krakauer, J. W., and Kitago, T. (2017). A Short and Distinct Time Window for Recovery of Arm Motor Control Early After Stroke Revealed With a Global Measure of Trajectory Kinematics. *Neurorehabilitation and Neural Repair*, 31(6):552–560.

Coupar, F., Pollock, A., Rowe, P., Weir, C., and Langhorne, P. (2012). Predictors of upper limb recovery after stroke: A systematic review and meta-analysis. *Clinical Rehabilitation*, 26(4):291–313.

Courtine, G., Bunge, M. B., Fawcett, J. W., Grossman, R. G., Kaas, J. H., Lemon, R., Maier, I., Martin, J., Nudo, R. J., Ramon-Cueto, A., Rouiller, E. M., Schnell, L., Wannier, T., Schwab, M. E., and Edgerton, V. R. (2007). Can experiments in nonhuman primates expedite the translation of treatments for spinal cord injury in humans? *Nature medicine*, 13(5):561–566.

Courtine, G., Gerasimenko, Y., van den Brand, R., Yew, A., Musienko, P., Zhong, H., Song, B., Ao, Y., Ichiyama, R. M., Lavrov, I., Roy, R. R., Sofroniew, M. V., and Edgerton, V. R. (2009). Transformation of nonfunctional spinal circuits into functional states after the loss of brain input. *Nature Neuroscience*, 12(10):1333–1342.

Cramer, S. C. (2015). Drugs to Enhance Motor Recovery After Stroke. *Stroke*, 46(10):2998–3005.

Dancause, N., Barbay, S., Frost, S. B., Zoubina, E. V., Plautz, E. J., Mahnken, J. D., and Nudo, R. J. (2006). Effects of small ischemic lesions in the primary motor cortex on neurophysiological organization in ventral premotor cortex. *Journal of Neurophysiology*, 96(6):3506–3511.

Dancause, N. and Nudo, R. J. (2011). Shaping plasticity to enhance recovery after injury. In *Progress in Brain Research*, volume 192, pages 273–295. Elsevier.

Darling, W. G., Pizzimenti, M. A., and Morecraft, R. J. (2011). Functional recovery following motor cortex lesions in non-human primates: Experimental implications for human stroke patients. *Journal of Integrative Neuroscience*, 10(03):353–384.

de Haan, M. J., Brochier, T., Grün, S., Riehle, A., and Barthélemy, F. V. (2018). Real-time visuomotor behavior and electrophysiology recording

setup for use with humans and monkeys. *Journal of Neurophysiology*, 120(2):539–552.

Dewald, J. P. A., Pope, P. S., Given, J. D., Buchanan, T. S., and Rymer, W. Z. (1995). Abnormal muscle coactivation patterns during isometric torque generation at the elbow and shoulder in hemiparetic subjects. *Brain*, 118(2):495–510.

Dewald, J. P. A., Sheshadri, V., Dawson, M. L., and Beer, R. F. (2001). Upper-Limb Discoordination in Hemiparetic Stroke: Implications for Neurorehabilitation. *Topics in Stroke Rehabilitation*, 8(1):1–12.

Di Pino, G., Pellegrino, G., Assenza, G., Capone, F., Ferreri, F., Formica, D., Ranieri, F., Tombini, M., Ziemann, U., Rothwell, J. C., and Di Lazzaro, V. (2014). Modulation of brain plasticity in stroke: A novel model for neurorehabilitation. *Nature Reviews Neurology*, 10(10):597–608.

Donnan, G. A., Fisher, M., Macleod, M., and Davis, S. M. (2008). Stroke. *The Lancet*, 371(9624):1612–1623.

Dum, R. P. and Strick, P. L. (1991). The origin of corticospinal projections from the premotor areas in the frontal lobe. *Journal of Neuroscience*, 11(3):667–689.

Dum, R. P. and Strick, P. L. (1996). Spinal Cord Terminations of the Medial Wall Motor Areas in Macaque Monkeys. *Journal of Neuroscience*, 16(20):6513–6525.

Dum, R. P. and Strick, P. L. (2002). Motor areas in the frontal lobe of the primate. *Physiology & Behavior*, 77(4):677–682.

Edwardson, M. A., Lucas, T. H., Carey, J. R., and Fetz, E. E. (2013). New modalities of brain stimulation for stroke rehabilitation. *Experimental Brain Research*, 224(3):335–358.

Eisner-Janowicz, I., Barbay, S., Hoover, E., Stowe, A. M., Frost, S. B., Plautz, E. J., and Nudo, R. J. (2008). Early and late changes in the distal forelimb representation of the supplementary motor area after injury to frontal motor areas in the squirrel monkey. *Journal of Neurophysiology*, 100(3):1498–1512.

Elias, G. J., Namasivayam, A. A., and Lozano, A. M. (2018). Deep brain stimulation for stroke: Current uses and future directions. *Brain Stimulation*, 11(1):3–28.

Emborg, M. E., Joers, V., Fisher, R., Brunner, K., Carter, V., Ross, C., Raghavan, R., Brady, M., Raschke, J., Kubota, K., and Alexander, A.

(2010). Intraoperative intracerebral MRI-guided navigation for accurate targeting in nonhuman primates. *Cell Transplantation*, 19(12):1587–1597.

Ethier, C., Oby, E. R., Bauman, M. J., and Miller, L. E. (2012). Restoration of grasp following paralysis through brain-controlled stimulation of muscles. *Nature*, 485(7398):368–371.

Eugster, C. H. and Takemoto, T. (1967). Zur Nomenklatur der neuen Verbindungen aus Amanita-Arten. *Helvetica Chimica Acta*, 50(1):126–127.

Favre, I., Zeffiro, T. A., Detante, O., Krainik, A., Hommel, M., and Jaillard, A. (2014). Upper Limb Recovery After Stroke Is Associated With Ipsilesional Primary Motor Cortical Activity: A Meta-Analysis. *Stroke*, 45(4):1077–1083.

Fedorov, A., Beichel, R., Kalpathy-Cramer, J., Finet, J., Fillion-Robin, J.-C., Pujol, S., Bauer, C., Jennings, D., Fennessy, F., Sonka, M., Buatti, J., Aylward, S., Miller, J. V., Pieper, S., and Kikinis, R. (2012). 3D Slicer as an Image Computing Platform for the Quantitative Imaging Network. *Magnetic resonance imaging*, 30(9):1323–1341.

Feigin, V. L., Nguyen, G., Cercy, K., Johnson, C. O., Alam, T., Parmar, P. G., Abajobir, A. A., Abate, K. H., Abd-Allah, F., Abejie, A. N., Abyu, G. Y., Ademi, Z., Agarwal, G., Ahmed, M. B., Akinyemi, R. O., Al-Raddadi, R., Aminde, L. N., Amlie-Lefond, C., Ansari, H., Asayesh, H., Asgedom, S. W., Atey, T. M., Ayele, H. T., Banach, M., Banerjee, A., Barac, A., Barker-Collo, S. L., Bärnighausen, T., Barregard, L., Basu, S., Bedi, N., Behzadifar, M., Béjot, Y., Bennett, D. A., Bensenor, I. M., Berhe, D. F., Boneya, D. J., Brainin, M., Campos-Nonato, I. R., Caso, V., Castañeda-Orjuela, C. A., Rivas, J. C., Catalá-López, F., Christensen, H., Criqui, M. H., Damasceno, A., Dandona, L., Dandona, R., Davletov, K., de Courten, B., deVeber, G., Dokova, K., Edessa, D., Endres, M., Faraon, E. J. A., Farvid, M. S., Fischer, F., Foreman, K., Forouzanfar, M. H., Gall, S. L., Gebrehiwot, T. T., Geleijnse, J. M., Gillum, R. F., Giroud, M., Goulart, A. C., Gupta, R., Gupta, R., Hachinski, V., Hamadeh, R. R., Hankey, G. J., Hareri, H. A., Havmoeller, R., Hay, S. I., Hegazy, M. I., Hibstu, D. T., James, S. L., Jeemon, P., John, D., Jonas, J. B., Jóźwiak, J., Kalani, R., Kandel, A., Kasaeian, A., Kengne, A. P., Khader, Y. S., Khan, A. R., Khang, Y.-H., Khubchandani, J., Kim, D., Kim, Y. J., Kivimaki, M., Kokubo, Y., Kolte, D., Kopec, J. A., Kosen, S., Kravchenko, M., Krishnamurthi, R., Kumar, G. A., Lafranconi, A., Lavados, P. M., Legesse, Y., Li, Y., Liang, X., Lo, W. D., Lorkowski,

S., Lotufo, P. A., Loy, C. T., Mackay, M. T., Abd El Razek, H. M., Mahdavi, M., Majeed, A., Malekzadeh, R., Malta, D. C., Mamun, A. A., Mantovani, L. G., Martins, S. C. O., Mate, K. K., Mazidi, M., Mehata, S., Meier, T., Melaku, Y. A., Mendoza, W., Mensah, G. A., Meretoja, A., Mezgebe, H. B., Miazgowski, T., Miller, T. R., Ibrahim, N. M., Mohammed, S., Mokdad, A. H., Moosazadeh, M., Moran, A. E., Musa, K. I., Negoi, R. I., Nguyen, M., Nguyen, Q. L., Nguyen, T. H., Tran, T. T., Nguyen, T. T., Anggraini Ningrum, D. N., Norrving, B., Noubiap, J. J., O'Donnell, M. J., Olagunju, A. T., Onuma, O. K., Owolabi, M. O., Parsaeian, M., Patton, G. C., Piradov, M., Pletcher, M. A., Pourmalek, F., Prakash, V., Qorbani, M., Rahman, M., Rahman, M. A., Rai, R. K., Ranta, A., Rawaf, D., Rawaf, S., Renzaho, A. M., Robinson, S. R., Sahathevan, R., Sahebkar, A., Salomon, J. A., Santalucia, P., Santos, I. S., Sartorius, B., Schutte, A. E., Sepanlou, S. G., Shafieesabet, A., Shaikh, M. A., Shamsizadeh, M., Sheth, K. N., Sisay, M., Shin, M.-J., Shiue, I., Silva, D. A. S., Sobngwi, E., Soljak, M., Sorensen, R. J. D., Sposato, L. A., Stranges, S., Suliankatchi, R. A., Tabarés-Seisdedos, R., Tanne, D., Nguyen, C. T., Thakur, J. S., Thrift, A. G., Tirschwell, D. L., Topor-Madry, R., Tran, B. X., Nguyen, L. T., Truelsen, T., Tsilimparis, N., Tyrovolas, S., Ukwaja, K. N., Uthman, O. A., Varakin, Y., Vasankari, T., Venketasubramanian, N., Vlassov, V. V., Wang, W., Werdecker, A., Wolfe, C. D. A., Xu, G., Yano, Y., Yonemoto, N., Yu, C., Zaidi, Z., El Sayed Zaki, M., Zhou, M., Ziaeian, B., Zipkin, B., Vos, T., Naghavi, M., Murray, C. J. L., and Roth, G. A. (2018). Global, Regional, and Country-Specific Lifetime Risks of Stroke, 1990 and 2016. *The New England Journal of Medicine*, 379(25):2429–2437.

Feng, W., Wang, J., Chhatbar, P. Y., Doughty, C., Landsittel, D., Lioutas, V.-A., Kautz, S., and Schlaug, G. (2015). Corticospinal Tract Lesion Load - A Potential Imaging Biomarker for Stroke Motor Outcomes. *Annals of neurology*, 78(6):860–870.

Ferrier, D. and Burdon-Sanderson, J. S. (1874). The localization of function in the brain. *Proceedings of the Royal Society of London*, 22(148-155):228–232.

Fetz, E. E. (2015). Restoring motor function with bidirectional neural interfaces. In *Progress in Brain Research*, volume 218, pages 241–252. Elsevier.

Fishman, P. S. and Frenkel, V. (2017). Focused Ultrasound: An Emerging Therapeutic Modality for Neurologic Disease. *Neurotherapeutics*, 14(2):393–404.

Frey, S., Pandya, D. N., Chakravarty, M. M., Bailey, L., Petrides, M., and Collins, D. L. (2011). An MRI based average macaque monkey stereotaxic atlas and space (MNI monkey space). *NeuroImage*, 55(4):1435–1442.

Fritsch, G. and Hitzig, E. (2009). Electric excitability of the cerebrum (Über die elektrische Erregbarkeit des Grosshirns). *Epilepsy & Behavior*, 15(2):123–130.

Fritsch, G. E. H. and Hitzig, E. (1870). Ueber die elektrische Erregbarkeit des Grosshirns. *-, Fritsch, Gustav Eduard Hitzig: Ueber die elektrische Erregbarkeit des Grosshirns, -: - -.*

Frost, S. B., Barbay, S., Friel, K. M., Plautz, E. J., and Nudo, R. J. (2003). Reorganization of Remote Cortical Regions After Ischemic Brain Injury: A Potential Substrate for Stroke Recovery. *Journal of Neurophysiology*, 89(6):3205–3214.

Frost, S. B., Barbay, S., Mumert, M. L., Stowe, A. M., and Nudo, R. J. (2006). An animal model of capsular infarct: Endothelin-1 injections in the rat. *Behavioural Brain Research*, 169(2):206–211.

Fugl-Meyer, A. R., Jääskö, L., and Norlin, V. (1975). The post-stroke hemiplegic patient. II. Incidence, mortality, and vocational return in Göteborg, Sweden with a review of the literature. *Scandinavian journal of rehabilitation medicine*, 7(2):73–83.

Furlan, M., Marchal, G., Derlon, J.-M., Baron, J.-C., and Viader, F. (1996). Spontaneous neurological recovery after stroke and the fate of the ischemic penumbra. *Annals of Neurology*, 40(2):216–226.

Gamberini, M., Passarelli, L., Fattori, P., and Galletti, C. (2020). Structural connectivity and functional properties of the macaque superior parietal lobule. *Brain Structure and Function*, 225(4):1349–1367.

Grefkes, C. and Fink, G. R. (2011). Reorganization of cerebral networks after stroke: New insights from neuroimaging with connectivity approaches. *Brain*, 134(5):1264–1276.

Grefkes, C. and Fink, G. R. (2014). Connectivity-based approaches in stroke and recovery of function. *The Lancet Neurology*, 13(2):206–216.

Grefkes, C., Nowak, D. A., and Eickhoff, S. B. (2008). Cortical connectivity after subcortical stroke assessed with functional magnetic resonance imaging. *Ann. Neurol*, pages 236–246.

Grefkes, C. and Ward, N. S. (2014). Cortical Reorganization After Stroke: How Much and How Functional? *The Neuroscientist*, 20(1):56–70.

Gresham, G. E., Alexander, D., Bishop, D. S., Giuliani, C., Goldberg, G., Holland, A., Kelly-Hayes, M., Linn, R. T., Roth, E. J., Stason, W. B., and Trombly, C. A. (1997). Rehabilitation. *Stroke*, 28(7):1522–1526.

Grünbaum, A. S. F. and Sherrington, C. S. (1904). Observations on the physiology of the cerebral cortex of the anthropoid apes. *Proceedings of the Royal Society of London*, 72(477-486):152–155.

Gu, Z., Kalambogias, J., Yoshioka, S., Han, W., Li, Z., Kawasawa, Y. I., Pochareddy, S., Li, Z., Liu, F., Xu, X., Wijeratne, H. R. S., Ueno, M., Blatz, E., Salomone, J., Kumanogoh, A., Rasin, M.-R., Gebelein, B., Weirauch, M. T., Sestan, N., Martin, J. H., and Yoshida, Y. (2017). Control of species-dependent cortico-motoneuronal connections underlying manual dexterity. *Science (New York, N.Y.)*, 357(6349):400–404.

Guénot, M., Isnard, J., Catenoix, H., Mauguière, F., and Sindou, M. (2011). SEEG-guided RF-thermocoagulation of epileptic foci: A therapeutic alternative for drug-resistant non-operable partial epilepsies. *Advances and Technical Standards in Neurosurgery*, 36:61–78.

Hankey, G. J., Spiesser, J., Hakimi, Z., Bego, G., Carita, P., and Gabriel, S. (2007). Rate, degree, and predictors of recovery from disability following ischemic stroke. *Neurology*, 68(19):1583–1587.

Hauska, T. L., Lanmüller, H., Kainz, W., and Alesch, F. (2010). Predictability of thermo-lesions using electrodes for deep brain stimulation - an in vitro study. *BMC Research Notes*, 3:84.

Hayward, K. S., Schmidt, J., Lohse, K. R., Peters, S., Bernhardt, J., Lannin, N. A., and Boyd, L. A. (2016). Are we armed with the right data? Pooled individual data review of biomarkers in people with severe upper limb impairment after stroke. *NeuroImage : Clinical*, 13:310–319.

He, S., Dum, R., and Strick, P. (1993). Topographic organization of corticospinal projections from the frontal lobe: Motor areas on the lateral surface of the hemisphere. *The Journal of Neuroscience*, 13(3):952–980.

Hebert, J. S. and Lewicke, J. (2012). Case report of modified Box and Blocks test with motion capture to measure prosthetic function. *The Journal of Rehabilitation Research and Development*, 49(8):1163.

Hebert, J. S., Lewicke, J., Williams, T. R., and Vette, A. H. (2014). Normative data for modified Box and Blocks test measuring upper-limb function via motion capture. *Journal of Rehabilitation Research and Development*, 51(6):918–932.

Hemphill, J. C., Greenberg, S. M., Anderson, C. S., Becker, K., Bendok, B. R., Cushman, M., Fung, G. L., Goldstein, J. N., Macdonald, R. L., Mitchell, P. H., Scott, P. A., Selim, M. H., and Woo, D. (2015). Guidelines for the Management of Spontaneous Intracerebral Hemorrhage. *Stroke*, 46(7):2032–2060.

Herbert, W. J., Powell, K., and Buford, J. A. (2015). Evidence for a role of the reticulospinal system in recovery of skilled reaching after cortical stroke: Initial results from a model of ischemic cortical injury. *Experimental Brain Research*, 233(11):3231–3251.

Higo, N. (2021). Non-human Primate Models to Explore the Adaptive Mechanisms After Stroke. *Frontiers in Systems Neuroscience*, 15.

Hoogewoud, F., Hamadjida, A., Wyss, A., Mir, A., Schwab, M., Belhaj-Saif, A., and Rouiller, E. (2013). Comparison of Functional Recovery of Manual Dexterity after Unilateral Spinal Cord Lesion or Motor Cortex Lesion in Adult Macaque Monkeys. *Frontiers in Neurology*, 4.

Jackson, A., Mavoori, J., and Fetz, E. E. (2006). Long-term motor cortex plasticity induced by an electronic neural implant. *Nature*, 444(7115):56–60.

Jackson, J. H. (1873). On the Anatomical Investigation of Epilepsy and Epileptiform Convulsions. *BMJ*, 1(645):531–533.

Johnson, C. O., Nguyen, M., Roth, G. A., Nichols, E., Alam, T., Abate, D., Abd-Allah, F., Abdelalim, A., Abraha, H. N., Abu-Rmeileh, N. M., Adebayo, O. M., Adeoye, A. M., Agarwal, G., Agrawal, S., Aichour, A. N., Aichour, I., Aichour, M. T. E., Alahdab, F., Ali, R., Alvis-Guzman, N., Anber, N. H., Anjomshoa, M., Arabloo, J., Arauz, A., Ärnlöv, J., Arora, A., Awasthi, A., Banach, M., Barboza, M. A., Barker-Collo, S. L., Bärnighausen, T. W., Basu, S., Belachew, A. B., Belayneh, Y. M., Bennett, D. A., Bensenor, I. M., Bhattacharyya, K., Biadgo, B., Bijani, A., Bikbov, B., Sayeed, M. S. B., Butt, Z. A., Cahuana-Hurtado, L., Carrero, J. J., Carvalho, F., Castañeda-Orjuela, C. A., Castro, F., Catalá-López, F., Chaiah, Y., Chiang, P. P.-C., Choi, J.-Y. J., Christensen, H., Chu, D.-T., Cortinovis, M., Damasceno, A. A. M., Dandona, L., Dandona, R., Daryani, A., Davletov, K., de Courten, B., la Cruz-Góngora, V. D., Degefa, M. G., Dharmaratne, S. D., Diaz, D., Dubey, M., Duken, E. E., Edessa, D., Endres, M., Faraon, E. J. A., Farzadfar, F., Fernandes, E., Fischer, F., Flor, L. S., Ganji, M., Gebre, A. K., Gebremichael, T. G., Geta, B., Gezae, K. E., Gill, P. S., Gnedovskaya, E. V., Gómez-Dantés, H., Goulart, A. C., Grosso, G., Guo, Y., Gupta, R., Haj-Mirzaian, A.,

Haj-Mirzaian, A., Hamidi, S., Hankey, G. J., Hassen, H. Y., Hay, S. I., Hegazy, M. I., Heidari, B., Herial, N. A., Hosseini, M. A., Hostiuc, S., Irvani, S. S. N., Islam, S. M. S., Jahanmehr, N., Javanbakht, M., Jha, R. P., Jonas, J. B., Jozwiak, J. J., Jürisson, M., Kahsay, A., Kalani, R., Kalkonde, Y., Kamil, T. A., Kanchan, T., Karch, A., Karimi, N., Karimi-Sari, H., Kasaeian, A., Kassa, T. D., Kazemeini, H., Kefale, A. T., Khader, Y. S., Khalil, I. A., Khan, E. A., Khang, Y.-H., Khubchandani, J., Kim, D., Kim, Y. J., Kisa, A., Kivimäki, M., Koyanagi, A., Krishnamurthi, R. K., Kumar, G. A., Lafranconi, A., Lewington, S., Li, S., Lo, W. D., Lopez, A. D., Lorkowski, S., Lotufo, P. A., Mackay, M. T., Majdan, M., Majdzadeh, R., Majeed, A., Malekzadeh, R., Manafi, N., Mansournia, M. A., Mehndiratta, M. M., Mehta, V., Mengistu, G., Meretoja, A., Meretoja, T. J., Miazgowski, B., Miazgowski, T., Miller, T. R., Mirrakhimov, E. M., Mohajer, B., Mohammad, Y., Mohammadoo-khorasani, M., Mohammed, S., Mohebi, F., Mokdad, A. H., Mokhayeri, Y., Moradi, G., Morawska, L., Velásquez, I. M., Mousavi, S. M., Muhammed, O. S. S., Muruet, W., Naderi, M., Naghavi, M., Naik, G., Nascimento, B. R., Negoi, R. I., Nguyen, C. T., Nguyen, L. H., Nirayo, Y. L., Norrving, B., Noubiap, J. J., Ofori-Asenso, R., Ogbo, F. A., Olagunju, A. T., Olagunju, T. O., Owolabi, M. O., Pandian, J. D., Patel, S., Perico, N., Piradov, M. A., Polinder, S., Postma, M. J., Poustchi, H., Prakash, V., Qorbani, M., Rafiei, A., Rahim, F., Rahimi, K., Rahimi-Movaghar, V., Rahman, M., Rahman, M. A., Reis, C., Remuzzi, G., Renzaho, A. M. N., Ricci, S., Roberts, N. L. S., Robinson, S. R., Roever, L., Roshandel, G., Sabbagh, P., Safari, H., Safari, S., Safiri, S., Sahebkar, A., Zahabi, S. S., Samy, A. M., Santalucia, P., Santos, I. S., Santos, J. V., Milicevic, M. M. S., Sartorius, B., Sawant, A. R., Schutte, A. E., Sepanlou, S. G., Shafieesabet, A., Shaikh, M. A., Shams-Beyranvand, M., Sheikh, A., Sheth, K. N., Shibuya, K., Shigematsu, M., Shin, M.-J., Shiue, I., Siabani, S., Sobaih, B. H., Sposato, L. A., Sutradhar, I., Sylaja, P. N., Szoeke, C. E. I., Ao, B. J. T., Temsah, M.-H., Temsah, O., Thrift, A. G., Tonelli, M., Topor-Madry, R., Tran, B. X., Tran, K. B., Truelsen, T. C., Tsadik, A. G., Ullah, I., Uthman, O. A., Vaduganathan, M., Valdez, P. R., Vasankari, T. J., Vasanthan, R., Venketasubramanian, N., Vosoughi, K., Vu, G. T., Waheed, Y., Weiderpass, E., Weldegwergs, K. G., Westerman, R., Wolfe, C. D. A., Wondafrash, D. Z., Xu, G., Yadollahpour, A., Yamada, T., Yatsuya, H., Yimer, E. M., Yonemoto, N., Yousefifard, M., Yu, C., Zaidi, Z., Zamani, M., Zarghi, A., Zhang, Y., Zodpey, S., Feigin, V. L., Vos, T., and Murray, C. J. L. (2019). Global, regional, and national burden of stroke, 1990–2016: A systematic analysis for the Global Burden of Disease Study 2016. *The Lancet Neurology*, 18(5):439–458.

Johnston, G. A. R. (2014). Muscimol as an Ionotropic GABA Receptor Agonist. *Neurochemical Research*, 39(10):1942–1947.

Kaeser, M., Brunet, J.-F., Wyss, A., Belhaj-Saif, A., Liu, Y., Hamadjida, A., Rouiller, E. M., and Bloch, J. (2011). Autologous Adult Cortical Cell Transplantation Enhances Functional Recovery Following Unilateral Lesion of Motor Cortex in Primates: A Pilot Study:. *Neurosurgery*, 68(5):1405–1417.

Kalladka, D., Sinden, J., Pollock, K., Haig, C., McLean, J., Smith, W., McConnachie, A., Santosh, C., Bath, P. M., Dunn, L., and Muir, K. W. (2016). Human neural stem cells in patients with chronic ischaemic stroke (PISCES): A phase 1, first-in-man study. *The Lancet*, 388(10046):787–796.

Kapur, N. (1996). Paradoxical functional facilitation in brain-behaviour research: A critical review. *Brain*, 119(5):1775–1790.

Karashchuk, P., Rupp, K. L., Dickinson, E. S., Walling-Bell, S., Sanders, E., Azim, E., Brunton, B. W., and Tuthill, J. C. (2021). Anipose: A toolkit for robust markerless 3D pose estimation. *Cell Reports*, 36(13):109730.

Kim, H.-S., Hwang, J. H., Han, S.-C., Kang, G.-H., Park, J.-Y., and Kim, H.-I. (2021). Precision Capsular Infarct Modeling to Produce Hand Motor Deficits in Cynomolgus Macaques. *Experimental Neurobiology*, 30(5):356–364.

King, R. L., Brown, J. R., Newsome, W. T., and Pauly, K. B. (2013). Effective parameters for ultrasound-induced in vivo neurostimulation. *Ultrasound in Medicine & Biology*, 39(2):312–331.

Kleim, J. A., Hogg, T. M., VandenBerg, P. M., Cooper, N. R., Bruneau, R., and Remple, M. (2004). Cortical Synaptogenesis and Motor Map Reorganization Occur during Late, But Not Early, Phase of Motor Skill Learning. *Journal of Neuroscience*, 24(3):628–633.

Koch, P., Schulz, R., and Hummel, F. C. (2016). Structural connectivity analyses in motor recovery research after stroke. *Annals of Clinical and Translational Neurology*, 3(3):233–244.

Kolominsky-Rabas, P. L., Weber, M., Gefeller, O., Neundoerfer, B., and Heuschmann, P. U. (2001). Epidemiology of Ischemic Stroke Subtypes According to TOAST Criteria: Incidence, Recurrence, and Long-Term Survival in Ischemic Stroke Subtypes: A Population-Based Study. *Stroke*, 32(12):2735–2740.

Kontson, K., Marcus, I., Myklebust, B., and Civillico, E. (2017). Targeted box and blocks test: Normative data and comparison to standard tests. *PLOS ONE*, 12(5):e0177965.

Krakauer, J. W. and Carmichael, S. T. (2017). Broken Movement: The Neurobiology of Motor Recovery after Stroke.

Krubitzer, L., Huffman, K. J., Disbrow, E., and Recanzone, G. (2004). Organization of area 3a in macaque monkeys: Contributions to the cortical phenotype. *Journal of Comparative Neurology*, 471(1):97–111.

Kurata, K. and Hoffman, D. S. (1994). Differential effects of muscimol microinjection into dorsal and ventral aspects of the premotor cortex of monkeys. *Journal of Neurophysiology*, 71(3):1151–1164.

Kuypers, H. G. J. M. (2011). Anatomy of the Descending Pathways. In *Comprehensive Physiology*, pages 597–666. John Wiley & Sons, Ltd.

Kwakkel, G., Kollen, B., and Twisk, J. (2006). Impact of Time on Improvement of Outcome After Stroke. *Stroke*, 37(9):2348–2353.

Kwakkel, G., van Peppen, R., Wagenaar, R. C., Wood Dauphinee, S., Richards, C., Ashburn, A., Miller, K., Lincoln, N., Partridge, C., Wellwood, I., and Langhorne, P. (2004). Effects of Augmented Exercise Therapy Time After Stroke: A Meta-Analysis. *Stroke*, 35(11):2529–2539.

Lacquaniti, F., Bianchetti, M., Hummelsheim, H., and Wiesendanger, M. (1987). Transient responses to load perturbations of the forearm in a monkey with a chronic lesion in the internal capsule. *Electroencephalography and Clinical Neurophysiology*, 67(5):485–494.

Langhorne, P., Coupar, F., and Pollock, A. (2009). Motor recovery after stroke: A systematic review. *The Lancet Neurology*, 8(8):741–754.

Lawrence, D. G. and Kuypers, H. G. (1968). THE FUNCTIONAL ORGANIZATION OF THE MOTOR SYSTEM IN THE MONKEY1: II. THE EFFECTS OF LESIONS OF THE DESCENDING BRAIN-STEM PATHWAYS. *Brain*, 91(1):15–36.

Lemon, R. (2019). Recent advances in our understanding of the primate corticospinal system. *F1000Research*, 8:F1000 Faculty Rev–274.

Lemon, R. N. (2008). Descending pathways in motor control. *Annual Review of Neuroscience*, 31:195–218.

Levin, M. F., Kleim, J. A., and Wolf, S. L. (2009). What Do Motor "Recovery" and "Compensation" Mean in Patients Following Stroke? *Neurorehabilitation and Neural Repair*, 23(4):313–319.

Levy, R. M., Harvey, R. L., Kissela, B. M., Winstein, C. J., Lutsep, H. L., Parrish, T. B., Cramer, S. C., and Venkatesan, L. (2016). Epidural Electrical Stimulation for Stroke Rehabilitation: Results of the Prospective, Multicenter, Randomized, Single-Blinded Everest Trial. *Neurorehabilitation and Neural Repair*, 30(2):107–119.

Li, S., Nie, E., Yin, Y., Benowitz, L., Tung, S., Vinters, H., Bahjat, F., Stenzel-Poore, M., Kawaguchi, R., Coppola, G., and Carmichael, S. (2015). GDF10 Is a Signal for Axonal Sprouting and Functional Recovery after Stroke. *Nature neuroscience*, 18(12):1737–1745.

Linkovski, O., Katzin, N., and Salti, M. (2017). Mirror Neurons and Mirror-Touch Synesthesia. *The Neuroscientist*, 23(2):103–108.

Lipsman, N., Meng, Y., Bethune, A. J., Huang, Y., Lam, B., Masellis, M., Herrmann, N., Heyn, C., Aubert, I., Boutet, A., Smith, G. S., Hynynen, K., and Black, S. E. (2018). Blood–brain barrier opening in Alzheimer's disease using MR-guided focused ultrasound. *Nature Communications*, 9(1):2336.

Liu, J., Wang, C., Qin, W., Ding, H., Guo, J., Han, T., Cheng, J., and Yu, C. (2020). Corticospinal Fibers With Different Origins Impact Motor Outcome and Brain After Subcortical Stroke. *Stroke*, 51(7):2170–2178.

Liu, Y. and Rouiller, E. M. (1999a). Mechanisms of recovery of dexterity following unilateral lesion of the sensorimotor cortex in adult monkeys. *Experimental Brain Research*, 128(1-2):149–159.

Liu, Y. and Rouiller, E. M. (1999b). Mechanisms of recovery of dexterity following unilateral lesion of the sensorimotor cortex in adult monkeys. *Experimental Brain Research*, 128(1-2):149–159.

Lo, A. C., Guarino, P. D., Richards, L. G., Haselkorn, J. K., Wittenberg, G. F., Federman, D. G., Ringer, R. J., Wagner, T. H., Krebs, H. I., Volpe, B. T., Bever, C. T., Bravata, D. M., Duncan, P. W., Corn, B. H., Maffucci, A. D., Nadeau, S. E., Conroy, S. S., Powell, J. M., Huang, G. D., and Peduzzi, P. (2010). Robot-Assisted Therapy for Long-Term Upper-Limb Impairment after Stroke. *New England Journal of Medicine*, 362(19):1772–1783.

Lowekamp, B. C., Chen, D. T., Ibáñez, L., and Blezek, D. (2013). The Design of SimpleITK. *Frontiers in Neuroinformatics*, 7:45.

Luengo-Fernandez, R., Violato, M., Candio, P., and Leal, J. (2020). Economic burden of stroke across Europe: A population-based cost analysis. *European Stroke Journal*, 5(1):17–25.

Luppino, G., Matelli, M., Camarda, R., and Rizzolatti, G. (1993). Corticocortical connections of area F3 (SMA-proper) and area F6 (pre-SMA) in the macaque monkey. *The Journal of Comparative Neurology*, 338(1):114–140.

Magara, A., Bühler, R., Moser, D., Kowalski, M., Pourtehrani, P., and Jeanmonod, D. (2014). First experience with MR-guided focused ultrasound in the treatment of Parkinson's disease. *Journal of Therapeutic Ultrasound*, 2(1):11.

Mardia, K. V. and Jupp, P. E. (2000). *Directional Statistics*. Wiley Series in Probability and Statistics. J. Wiley, Chichester ; New York.

Martin, J. H. (1991). Autoradiographic estimation of the extent of reversible inactivation produced by microinjection of lidocaine and muscimol in the rat. *Neuroscience Letters*, 127(2):160–164.

Mason, C. R., Miller, L. E., Baker, J. F., and Houk, J. C. (1998). Organization of Reaching and Grasping Movements in the Primate Cerebellar Nuclei as Revealed by Focal Muscimol Inactivations. *Journal of Neurophysiology*, 79(2):537–554.

Matelli, M., Luppino, G., and Rizzolatti, G. (1985). Patterns of cytochrome oxidase activity in the frontal agranular cortex of the macaque monkey. *Behavioural Brain Research*, 18(2):125–136.

Mathiowetz, V., Volland, G., Kashman, N., and Weber, K. (1985). Adult norms for the Box and Block Test of manual dexterity. *The American Journal of Occupational Therapy: Official Publication of the American Occupational Therapy Association*, 39(6):386–391.

Matsumura, M., Sawaguchi, T., Oishi, T., Ueki, K., and Kubota, K. (1991). Behavioral deficits induced by local injection of bicuculline and muscimol into the primate motor and premotor cortex. *Journal of Neurophysiology*, 65(6):1542–1553.

Merdler, T., Liebermann, D. G., Levin, M. F., and Berman, S. (2013). Arm-plane representation of shoulder compensation during pointing movements in patients with stroke. *Journal of Electromyography and Kinesiology*, 23(4):938–947.

Meyer, C. R., Moffat, B. A., Kuszpit, K., Bland, P. L., Chenevert, T. L., Rehemtulla, A., and Ross, B. D. (2006). A Methodology for Registration of a Histological Slide and in vivo MRI Volume based on Optimizing Mutual Information. *Molecular imaging*, 5(1):16–23.

Meyer, K., Simmet, A., Arnold, M., Mattle, H., and Nedeltchev, K. (2009). Stroke events, and case fatalities in Switzerland based on hospital statistics and cause of death statistics. *Swiss Medical Weekly*, 139(5-6):65–69.

Miocinovic, S., Zhang, J., Xu, W., Russo, G. S., Vitek, J. L., and McIntyre, C. C. (2007). Stereotactic neurosurgical planning, recording, and visualization for deep brain stimulation in non-human primates. *Journal of neuroscience methods*, 162(1-2):32–41.

Miyakawa, T. (2020). No raw data, no science: Another possible source of the reproducibility crisis. *Molecular Brain*, 13(1):24.

Morecraft, R. J., Ge, J., Stilwell-Morecraft, K. S., McNeal, D. W., Pizzimenti, M. A., and Darling, W. G. (2013). Terminal Distribution of the Corticospinal Projection from the Hand/Arm Region of the Primary Motor Cortex to the Cervical Enlargement in Rhesus Monkey. *The Journal of comparative neurology*, 521(18):4205–4235.

Morecraft, R. J., Herrick, J. L., Stilwell-Morecraft, K. S., Louie, J. L., Schroeder, C. M., Ottenbacher, J. G., and Schoolfield, M. W. (2002). Localization of arm representation in the corona radiata and internal capsule in the non-human primate. *Brain*, 125(1):176–198.

Morecraft, R. J., McNeal, D. W., Stilwell-Morecraft, K. S., Dvanajscak, Z., Ge, J., and Schneider, P. (2007). Localization of arm representation in the cerebral peduncle of the non-human primate. *Journal of Comparative Neurology*, 504(2):149–167.

Moringlane, J. R., Koch, R., Schäfer, H., and Ostertag, C. B. (1989). Experimental radiofrequency (RF) coagulation with computer-based on line monitoring of temperature and power. *Acta Neurochirurgica*, 96(3-4):126–131.

Murata, Y. and Higo, N. (2016). Development and Characterization of a Macaque Model of Focal Internal Capsular Infarcts. *PLOS ONE*, 11(5):e0154752.

Murata, Y., Higo, N., Oishi, T., Yamashita, A., Matsuda, K., Hayashi, M., and Yamane, S. (2008). Effects of Motor Training on the Recovery of Manual Dexterity After Primary Motor Cortex Lesion in Macaque Monkeys. *Journal of Neurophysiology*, 99(2):773–786.

Murphy, T. H. and Corbett, D. (2009). Plasticity during stroke recovery: From synapse to behaviour. *Nature Reviews Neuroscience*, 10(12):861–872.

Nakayma, H., Jørgensen, H. S., Raaschou, H. O., and Olsen, T. S. (1994). Compensation in recovery of upper extremity function after stroke: The Copenhagen Stroke Study. *Archives of Physical Medicine and Rehabilitation*, 75(8):852–857.

Nam, M.-H., Cho, J., Kwon, D.-H., Park, J.-Y., Woo, J., Lee, J. M., Lee, S., Ko, H. Y., Won, W., Kim, R. G., Song, H., Oh, S.-J., Choi, J. W., Park, K. D., Park, E. K., Jung, H., Kim, H.-S., Lee, M.-C., Yun, M., Lee, C. J., and Kim, H.-I. (2020). Excessive Astrocytic GABA Causes Cortical Hypometabolism and Impedes Functional Recovery after Subcortical Stroke. *Cell Reports*, 32(1):107861.

Narabayashi, H. and Ohye, C. (1980). Importance of Microstereoencephalotomy for Tremor Alleviation. *Stereotactic and Functional Neurosurgery*, 43(3-5):222–227.

Nath, T., Mathis, A., Chen, A. C., Patel, A., Bethge, M., and Mathis, M. W. (2019). Using DeepLabCut for 3D markerless pose estimation across species and behaviors. *Nature Protocols*, 14(7):2152–2176.

Nelson, R. J., Sur, M., Felleman, D. J., and Kaas, J. H. (1980). Representations of the body surface in postcentral parietal cortex ofMacaca fascicularis. *The Journal of Comparative Neurology*, 192(4):611–643.

Nijland, R. H., van Wegen, E. E., Harmeling-van der Wel, B. C., and Kwakkel, G. (2010). Presence of Finger Extension and Shoulder Abduction Within 72 Hours After Stroke Predicts Functional Recovery. *Stroke*, 41(4):745–750.

Nikolov, P., Heil, V., Hartmann, C. J., Ivanov, N., Slotty, P. J., Vesper, J., Schnitzler, A., and Groiss, S. J. (2022). Motor Evoked Potentials Improve Targeting in Deep Brain Stimulation Surgery. *Neuromodulation: Technology at the Neural Interface*.

Nishimura, Y., Perlmutter, S. I., Eaton, R. W., and Fetz, E. E. (2013). Spike-Timing-Dependent Plasticity in Primate Corticospinal Connections Induced during Free Behavior. *Neuron*, 80(5):1301–1309.

Nudo, R. J. and Milliken, G. W. (1996). Reorganization of movement representations in primary motor cortex following focal ischemic infarcts in adult squirrel monkeys. *Journal of Neurophysiology*, 75(5):2144–2149.

Nys, G. M. S., van Zandvoort, M. J. E., de Kort, P. L. M., Jansen, B. P. W., de Haan, E. H. F., and Kappelle, L. J. (2007). Cognitive disorders in acute stroke: Prevalence and clinical determinants. *Cerebrovascular Diseases (Basel, Switzerland)*, 23(5-6):408–416.

Ojaghihaghighi, S., Vahdati, S. S., Mikaeilpour, A., and Ramouz, A. (2017). Comparison of neurological clinical manifestation in patients with hemorrhagic and ischemic stroke. *World Journal of Emergency Medicine*, 8(1):34–38.

Olesen, J., Gustavsson, A., Svensson, M., Wittchen, H.-U., Jönsson, B., study Group, o. b. o. t. C., and Council, t. E. B. (2012). The economic cost of brain disorders in Europe. *European Journal of Neurology*, 19(1):155–162.

Omrani, M., Murnaghan, C. D., Pruszynski, J. A., and Scott, S. H. (2016). Distributed task-specific processing of somatosensory feedback for voluntary motor control. *eLife*, 5:e13141.

Ose, T., Autio, J. A., Ohno, M., Frey, S., Uematsu, A., Kawasaki, A., Takeda, C., Hori, Y., Nishigori, K., Nakako, T., Yokoyama, C., Nagata, H., Yamamori, T., Van Essen, D. C., Glasser, M. F., Watabe, H., and Hayashi, T. (2022). Anatomical variability, multi-modal coordinate systems, and precision targeting in the marmoset brain. *NeuroImage*, 250:118965.

Otero-Ortega, L., Laso-García, F., Gómez-de Frutos, M. d. C., Rodríguez-Frutos, B., Pascual-Guerra, J., Fuentes, B., Díez-Tejedor, E., and Gutiérrez-Fernández, M. (2017). White Matter Repair After Extracellular Vesicles Administration in an Experimental Animal Model of Subcortical Stroke. *Scientific Reports*, 7(1):44433.

Park, C.-h., Kou, N., and Ward, N. S. (2016). The contribution of lesion location to upper limb deficit after stroke. *Journal of Neurology, Neurosurgery & Psychiatry*, 87(12):1283–1286.

Petrosyan, H. A., Alessi, V., Singh, V., Hunanyan, A. S., Levine, J. M., and Arvanian, V. L. (2014). Transduction efficiency of neurons and glial cells by AAV-1, -5, -9, -rh10 and -hu11 serotypes in rat spinal cord following contusion injury. *Gene Therapy*, 21(12):991–1000.

Petty, G. W., Brown, R. D., Whisnant, J. P., Sicks, J. D., O'Fallon, W. M., and Wiebers, D. O. (1999). Ischemic Stroke Subtypes: A Population-Based Study of Incidence and Risk Factors. *Stroke*, 30(12):2513–2516.

Petty, G. W., Brown, R. D., Whisnant, J. P., Sicks, J. D., O'Fallon, W. M., and Wiebers, D. O. (2000). Ischemic Stroke Subtypes: A Population-Based Study of Functional Outcome, Survival, and Recurrence. *Stroke*, 31(5):1062–1068.

Piatkevich, K. D. and Verkhusha, V. V. (2011). Guide to Red Fluorescent Proteins and Biosensors for Flow Cytometry. *Methods in cell biology*, 102:431–461.

Plautz, E. J., Barbay, S., Frost, S. B., Friel, K. M., Dancause, N., Zoubina, E. V., Stowe, A. M., Quaney, B. M., and Nudo, R. J. (2003). Post-infarct cortical plasticity and behavioral recovery using concurrent cortical stimulation and rehabilitative training: A feasibility study in primates. *Neurological Research*, 25(8):801–810.

Plautz, E. J., Milliken, G. W., and Nudo, R. J. (2000). Effects of Repetitive Motor Training on Movement Representations in Adult Squirrel Monkeys: Role of Use versus Learning. *Neurobiology of Learning and Memory*, 74(1):27–55.

Pons, T. P., Garraghty, P. E., Cusick, C. G., and Kaas, J. H. (1985). The somatotopic organization of area 2 in macaque monkeys. *Journal of Comparative Neurology*, 241(4):445–466.

Powers, W. J., Rabinstein Alejandro A., Ackerson Teri, Adeoye Opeolu M., Bambakidis Nicholas C., Becker Kyra, Biller José, Brown Michael, Demaerschalk Bart M., Hoh Brian, Jauch Edward C., Kidwell Chelsea S., Leslie-Mazwi Thabele M., Ovbiagele Bruce, Scott Phillip A., Sheth Kevin N., Southerland Andrew M., Summers Deborah V., Tirschwell David L., and null null (2019). Guidelines for the Early Management of Patients With Acute Ischemic Stroke: 2019 Update to the 2018 Guidelines for the Early Management of Acute Ischemic Stroke: A Guideline for Healthcare Professionals From the American Heart Association/American Stroke Association. *Stroke*, 50(12):e344–e418.

Prabhakaran, S., Zarahn, E., Riley, C., Speizer, A., Chong, J. Y., Lazar, R. M., Marshall, R. S., and Krakauer, J. W. (2008). Inter-individual Variability in the Capacity for Motor Recovery After Ischemic Stroke. *Neurorehabilitation and Neural Repair*, 22(1):64–71.

Puentes, S., Kaido, T., Hanakawa, T., Ichinohe, N., Otsuki, T., and Seki, K. (2015). Internal capsule stroke in the common marmoset. *Neuroscience*, 284:400–411.

Püspöki, Z., Storath, M., Sage, D., and Unser, M. (2016). Transforms and Operators for Directional Bioimage Analysis: A Survey. *Advances in Anatomy, Embryology, and Cell Biology*, 219:69–93.

Raghavan, P. (2015). Upper Limb Motor Impairment Post Stroke. *Physical medicine and rehabilitation clinics of North America*, 26(4):599–610.

Ramanathan, D. S., Guo, L., Gulati, T., Davidson, G., Hishinuma, A. K., Won, S.-J., Knight, R. T., Chang, E. F., Swanson, R. A., and Ganguly, K. (2018). Low-frequency cortical activity is a neuromodulatory target that tracks recovery after stroke. *Nature Medicine*, 24(8):1257–1267.

Ramsey, L. E., Siegel, J. S., Lang, C. E., Strube, M., Shulman, G. L., and Corbetta, M. (2017). Behavioural clusters and predictors of performance during recovery from stroke. *Nature Human Behaviour*, 1(3):0038.

Rathelot, J.-A. and Strick, P. L. (2006). Muscle representation in the macaque motor cortex: An anatomical perspective. *Proceedings of the National Academy of Sciences of the United States of America*, 103(21):8257–8262.

Rathelot, J.-A. and Strick, P. L. (2009). Subdivisions of primary motor cortex based on cortico-motoneuronal cells. *Proceedings of the National Academy of Sciences of the United States of America*, 106(3):918–923.

Rathore, S. S., Hinn, A. R., Cooper, L. S., Tyroler, H. A., and Rosamond, W. D. (2002). Characterization of incident stroke signs and symptoms: Findings from the atherosclerosis risk in communities study. *Stroke*, 33(11):2718–2721.

Rehme, A. K., Fink, G. R., von Cramon, D. Y., and Grefkes, C. (2011). The Role of the Contralesional Motor Cortex for Motor Recovery in the Early Days after Stroke Assessed with Longitudinal fMRI. *Cerebral Cortex*, 21(4):756–768.

Réthi, A. (1913). Die elektrolytische Behandlung der Trigeminusneuralgien. *Munch Med Wochenschr*, 60:295–296.

Rezakhaniha, R., Agianniotis, A., Schrauwen, J. T. C., Griffa, A., Sage, D., Bouten, C. V. C., van de Vosse, F. N., Unser, M., and Stergiopulos, N. (2012). Experimental investigation of collagen waviness and orientation in the arterial adventitia using confocal laser scanning microscopy. *Biomechanics and Modeling in Mechanobiology*, 11(3-4):461–473.

Riley, J. D., Le, V., Der-Yeghiaian, L., See, J., Newton, J. M., Ward, N. S., and Cramer, S. C. (2011). Anatomy of Stroke Injury Predicts Gains From Therapy. *Stroke*, 42(2):421–426.

Ringman, J. M., Saver, J. L., Woolson, R. F., Clarke, W. R., and Adams, H. P. (2004). Frequency, risk factors, anatomy, and course of unilateral neglect in an acute stroke cohort. *Neurology*, 63(3):468–474.

Rizzolatti, G. and Luppino, G. (2001a). The Cortical Motor System. *Neuron*, 31(6):889–901.

Rizzolatti, G. and Luppino, G. (2001b). Pre-motor Cortex. In Smelser, N. J. and Baltes, P. B., editors, *International Encyclopedia of the Social & Behavioral Sciences*, pages 11989–11994. Pergamon, Oxford.

Rizzolatti, G., Luppino, G., and Matelli, M. (1998). The organization of the cortical motor system: New concepts. *Electroencephalography and Clinical Neurophysiology*, 106(4):283–296.

Roby-Brami, A., Feydy, A., Combeaud, M., Biryukova, E. V., Bussel, B., and Levin, M. F. (2003). Motor compensation and recovery for reaching in stroke patients. *Acta Neurologica Scandinavica*, 107(5):369–381.

Rossini, P. M., Calautti, C., Pauri, F., and Baron, J.-C. (2003). Post-stroke plastic reorganisation in the adult brain. *The Lancet Neurology*, 2(8):493–502.

Rouiller, E., Yu, X., Moret, V., Tempini, A., Wiesendanger, M., and Liang, F. (1998). Dexterity in adult monkeys following early lesion of the motor cortical hand area: The role of cortex adjacent to the lesion. *European Journal of Neuroscience*, 10(2):729–740.

Rouiller, E. M. and Olivier, E. (2004). Functional recovery after lesions of the primary motor cortex. In *Progress in Brain Research*, volume 143, pages 467–475. Elsevier.

Salegio, E. A., Bresnahan, J. C., Sparrey, C. J., Camisa, W., Fischer, J., Leasure, J., Buckley, J., Nout-Lomas, Y. S., Rosenzweig, E. S., Moseanko, R., Strand, S., Hawbecker, S., Lemoy, M.-J., Haefeli, J., Ma, X., Nielson, J. L., Edgerton, V., Ferguson, A. R., Tuszynski, M. H., and Beattie, M. S. (2016). A Unilateral Cervical Spinal Cord Contusion Injury Model in Non-Human Primates (Macaca mulatta). *Journal of Neurotrauma*, 33(5):439–459.

Santisteban, L., Térémetz, M., Bleton, J.-P., Baron, J.-C., Maier, M. A., and Lindberg, P. G. (2016). Upper Limb Outcome Measures Used in Stroke Rehabilitation Studies: A Systematic Literature Review. *PLoS ONE*, 11(5):e0154792.

Sawada, M., Kato, K., Kunieda, T., Mikuni, N., Miyamoto, S., Onoe, H., Isa, T., and Nishimura, Y. (2015). Function of the nucleus accumbens in motor control during recovery after spinal cord injury. *Science*, 350(6256):98–101.

Schaefer, S. Y., Patterson, C. B., and Lang, C. E. (2013). Transfer of training between distinct motor tasks after stroke: Implications for task-

specific approaches to upper extremity neurorehabilitation. *Neurorehabilitation and neural repair*, 27(7):602–612.

Schaffelhofer, S. and Scherberger, H. (2016). Object vision to hand action in macaque parietal, premotor, and motor cortices. *eLife*, 5:e15278.

Schilling, K. G., Gao, Y., Christian, M., Janve, V., Stepniewska, I., Landman, B. A., and Anderson, A. W. (2019). A Web-Based Atlas Combining MRI and Histology of the Squirrel Monkey Brain. *Neuroinformatics*, 17(1):131–145.

Schindelin, J., Arganda-Carreras, I., Frise, E., Kaynig, V., Longair, M., Pietzsch, T., Preibisch, S., Rueden, C., Saalfeld, S., Schmid, B., Tinevez, J.-Y., White, D. J., Hartenstein, V., Eliceiri, K., Tomancak, P., and Cardona, A. (2012). Fiji: An open-source platform for biological-image analysis. *Nature Methods*, 9(7):676–682.

Schulz, R., Braass, H., Liuzzi, G., Hoerniss, V., Lechner, P., Gerloff, C., and Hummel, F. C. (2015). White matter integrity of premotor–motor connections is associated with motor output in chronic stroke patients. *NeuroImage: Clinical*, 7:82–86.

Schulz, R., Park, C.-H., Boudrias, M.-H., Gerloff, C., Hummel, F. C., and Ward, N. S. (2012). Assessing the integrity of corticospinal pathways from primary and secondary cortical motor areas after stroke. *Stroke*, 43(8):2248–2251.

Schulz, R., Park, E., Lee, J., Chang, W. H., Lee, A., Kim, Y.-H., and Hummel, F. C. (2017a). Interactions Between the Corticospinal Tract and Premotor–Motor Pathways for Residual Motor Output After Stroke. *Stroke*, 48(10):2805–2811.

Schulz, R., Park, E., Lee, J., Chang, W. H., Lee, A., Kim, Y.-H., and Hummel, F. C. (2017b). Synergistic but independent: The role of corticospinal and alternate motor fibers for residual motor output after stroke. *NeuroImage: Clinical*, 15:118–124.

Sengul, G. (2012). *Atlas of the Spinal Cord of the Mouse, Rat, Rhesus, Marmoset, and Human*. Academic, Oxford.

Shokur, S., Donati, A. R. C., Campos, D. S. F., Gitti, C., Bao, G., Fischer, D., Almeida, S., Braga, V. A. S., Augusto, P., Petty, C., Alho, E. J. L., Lebedev, M., Song, A. W., and Nicolelis, M. A. L. (2018). Training with brain-machine interfaces, visuo-tactile feedback and assisted locomotion improves sensorimotor, visceral, and psychological signs in chronic paraplegic patients. *PLOS ONE*, 13(11):e0206464.

Steinberg, G. K., Kondziolka, D., Wechsler, L. R., Lunsford, L. D., Coburn, M. L., Billigen, J. B., Kim, A. S., Johnson, J. N., Bates, D., King, B., Case, C., McGrogan, M., Yankee, E. W., and Schwartz, N. E. (2016). Clinical Outcomes of Transplanted Modified Bone Marrow-Derived Mesenchymal Stem Cells in Stroke: A Phase 1/2a Study. *Stroke*, 47(7):1817–1824.

Stinear, C. M., Barber, P. A., Petoe, M., Anwar, S., and Byblow, W. D. (2012). The PREP algorithm predicts potential for upper limb recovery after stroke. *Brain*, 135(8):2527–2535.

Strick, P. L., Dum, R. P., and Rathelot, J.-A. (2021). The Cortical Motor Areas and the Emergence of Motor Skills: A Neuroanatomical Perspective. *Annual Review of Neuroscience*, 44(1):425–447.

Sudlow, C. and Warlow, C. (1997). Comparable Studies of the Incidence of Stroke and its Pathological Types: Results From an International Collaboration. *Stroke*, 28(3):491–499.

Sun, T. and Hevner, R. F. (2014). Growth and folding of the mammalian cerebral cortex: From molecules to malformations. *Nature reviews. Neuroscience*, 15(4):217–232.

Sunshine, M. D., Cho, F. S., Lockwood, D. R., Fechko, A. S., Kasten, M. R., and Moritz, C. T. (2013). Cervical intraspinal microstimulation evokes robust forelimb movements before and after injury. *Journal of neural engineering*, 10(3):036001.

Taub, E. and Uswatte, G. (2003). Constraint-induced movement therapy: Bridging from the primate laboratory to the stroke rehabilitation laboratory. *Journal of Rehabilitation Medicine*, 35(0):34–40.

Taub, E., Uswatte, G., Bowman, M. H., Mark, V. W., Delgado, A., Bryson, C., Morris, D., and Bishop-McKay, S. (2013). Constraint-Induced Movement Therapy Combined With Conventional Neurorehabilitation Techniques in Chronic Stroke Patients With Plegic Hands: A Case Series. *Archives of Physical Medicine and Rehabilitation*, 94(1):86–94.

Terashima, T. (1981). Okajimas Folia Anat. Jpn., 58 (2): 115-136, June 1981 Quantitative Study on Degenerated Myelinated Fibers in the Pyramid and Spinal Cord Following Lesion in the Internal Capsule of the Rhesus Monkey, with Special Reference to Collateral Branching in the Cervical Cord. *Okajimas Folia Anatomica Japonica*, 58(2):115–135.

Teskey, G. C., Flynn, C., Goertzen, C. D., Monfils, M. H., and Young,

N. A. (2003). Cortical stimulation improves skilled forelimb use following a focal ischemic infarct in the rat. *Neurological Research*, 25(8):794–800.

Tombari, D., Loubinoux, I., Pariente, J., Gerdelat, A., Albucher, J.-F., Tardy, J., Cassol, E., and Chollet, F. (2004). A longitudinal fMRI study: In recovering and then in clinically stable sub-cortical stroke patients. *NeuroImage*, 23(3):827–839.

Traversa, R., Cicinelli, P., Bassi, A., Rossini, P. M., and Bernardi, G. (1997). Mapping of Motor Cortical Reorganization After Stroke. *Stroke*, 28(1):110–117.

Twitchell, T. E. (1951). THE RESTORATION OF MOTOR FUNCTION FOLLOWING HEMIPLEGIA IN MAN. *Brain*, 74(4):443–480.

Urbin, M. A., Collinger, J. L., and Wittenberg, G. F. (2021). Corticospinal recruitment of spinal motor neurons in human stroke survivors. *The Journal of Physiology*, 599(18):4357–4373.

Urbin, M. A., Ozdemir, R. A., Tazoe, T., and Perez, M. A. (2017). Spike-timing-dependent plasticity in lower-limb motoneurons after human spinal cord injury. *Journal of Neurophysiology*, 118(4):2171–2180.

Verhagen, L., Gallea, C., Folloni, D., Constans, C., Jensen, D. E., Ahnine, H., Roumazeilles, L., Santin, M., Ahmed, B., Lehericy, S., Klein-Flügge, M. C., Krug, K., Mars, R. B., Rushworth, M. F., Pouget, P., Aubry, J.-F., and Sallet, J. (2019). Offline impact of transcranial focused ultrasound on cortical activation in primates. *eLife*, 8:e40541.

VideoLan (2006). VLC media player. https://www.videolan.org/vlc/index.html.

Virani, S. S., Alonso, A., Aparicio, H. J., Benjamin, E. J., Bittencourt, M. S., Callaway, C. W., Carson, A. P., Chamberlain, A. M., Cheng, S., Delling, F. N., Elkind, M. S., Evenson, K. R., Ferguson, J. F., Gupta, D. K., Khan, S. S., Kissela, B. M., Knutson, K. L., Lee, C. D., Lewis, T. T., Liu, J., Loop, M. S., Lutsey, P. L., Ma, J., Mackey, J., Martin, S. S., Matchar, D. B., Mussolino, M. E., Navaneethan, S. D., Perak, A. M., Roth, G. A., Samad, Z., Satou, G. M., Schroeder, E. B., Shah, S. H., Shay, C. M., Stokes, A., VanWagner, L. B., Wang, N.-Y., Tsao, C. W., and On behalf of the American Heart Association Council on Epidemiology and Prevention Statistics Committee and Stroke Statistics Subcommittee (2021). Heart Disease and Stroke Statistics—2021 Update: A Report From the American Heart Association. *Circulation*, 143(8).

Wafa, H. A., Wolfe, C. D. A., Emmett, E., Roth, G. A., Johnson, C. O., and Wang, Y. (2020). Burden of Stroke in Europe: Thirty-Year Projections of Incidence, Prevalence, Deaths, and Disability-Adjusted Life Years. *Stroke*, 51(8):2418–2427.

Wahl, A. S., Büchler, U., Brändli, A., Brattoli, B., Musall, S., Kasper, H., Ineichen, B. V., Helmchen, F., Ommer, B., and Schwab, M. E. (2017). Optogenetically stimulating intact rat corticospinal tract post-stroke restores motor control through regionalized functional circuit formation. *Nature Communications*, 8(1):1187.

Wahl, A. S., Omlor, W., Rubio, J. C., Chen, J. L., Zheng, H., Schroter, A., Gullo, M., Weinmann, O., Kobayashi, K., Helmchen, F., Ommer, B., and Schwab, M. E. (2014). Asynchronous therapy restores motor control by rewiring of the rat corticospinal tract after stroke. *Science*, 344(6189):1250–1255.

Wahl, A.-S. and Schwab, M. E. (2014). Finding an optimal rehabilitation paradigm after stroke: Enhancing fiber growth and training of the brain at the right moment. *Frontiers in Human Neuroscience*, 8.

Wang, G.-P., Guo, J.-Y., Peng, Z., Liu, Y.-Y., Xie, J., and Gong, S.-S. (2014). Adeno-associated virus-mediated gene transfer targeting normal and traumatized mouse utricle. *Gene Therapy*, 21(11):958–966.

Wang, Y. L., Wu, D., Liao, X., Zhang, W., Zhao, X., and Wang, Y. J. (2007). Burden of Stroke in China. *International Journal of Stroke*, 2(3):211–213.

Ward, N. S. (2017). Restoring brain function after stroke — bridging the gap between animals and humans. *Nature Reviews Neurology*, 13(4):244–255.

Ward, N. S., Brown, M. M., Thompson, A. J., and Frackowiak, R. S. J. (2003). Neural correlates of outcome after stroke: A cross-sectional fMRI study. *Brain*, 126(6):1430–1448.

Ward, N. S., Kelly, K., and Brander, F. (2015). The future of stroke rehabilitation: Upper limb recovery. *ACNR*, 15(4):6–8.

Watakabe, A., Ohtsuka, M., Kinoshita, M., Takaji, M., Isa, K., Mizukami, H., Ozawa, K., Isa, T., and Yamamori, T. (2015). Comparative analyses of adeno-associated viral vector serotypes 1, 2, 5, 8 and 9 in marmoset, mouse and macaque cerebral cortex. *Neuroscience Research*, 93:144–157.

Wei, X.-E., Shang, K., Zhou, J., Zhou, Y.-J., and Li, Y.-H. (2019). Acute Subcortical Infarcts Cause Secondary Degeneration in the Remote Non-

involved Cortex and Connecting Fiber Tracts. *Frontiers in Neurology*, 10.

Whitsel, B. L., Petrucelli, L. M., and Werner, G. (1969). Symmetry and connectivity in the map of the body surface in somatosensory area II of primates. *Journal of Neurophysiology*, 32(2):170–183.

Wiesendanger, M., Hummelsheim, H., Bianchetti, M., Chen, D. F., Hyland, B., Maier, V., and Wiesendanger, R. (1987). Input and output organization of the supplementary motor area. *Ciba Foundation Symposium*, 132:40–62.

Williams, L. S., Ghose, S. S., and Swindle, R. W. (2004). Depression and Other Mental Health Diagnoses Increase Mortality Risk After Ischemic Stroke. *American Journal of Psychiatry*, 161(6):1090–1095.

Williams, L. S., Yilmaz, E. Y., and Lopez-Yunez, A. M. (2000). Retrospective Assessment of Initial Stroke Severity With the NIH Stroke Scale. *Stroke*, 31(4):858–862.

Winstein, C. J. and Kay, D. B. (2015). Chapter 16 - Translating the science into practice: Shaping rehabilitation practice to enhance recovery after brain damage. In Dancause, N., Nadeau, S., and Rossignol, S., editors, *Progress in Brain Research*, volume 218 of *Sensorimotor Rehabilitation*, pages 331–360. Elsevier.

Winstein, C. J., Stein, Joel, Arena Ross, Bates Barbara, Cherney Leora R., Cramer Steven C., Deruyter Frank, Eng Janice J., Fisher Beth, Harvey Richard L., Lang Catherine E., MacKay-Lyons Marilyn, Ottenbacher Kenneth J., Pugh Sue, Reeves Mathew J., Richards Lorie G., Stiers William, and Zorowitz Richard D. (2016). Guidelines for Adult Stroke Rehabilitation and Recovery. *Stroke*, 47(6):e98–e169.

Winters, C., van Wegen, E. E. H., Daffertshofer, A., and Kwakkel, G. (2015). Generalizability of the Proportional Recovery Model for the Upper Extremity After an Ischemic Stroke. *Neurorehabilitation and Neural Repair*, 29(7):614–622.

Witham, C. L., Fisher, K. M., Edgley, S. A., and Baker, S. N. (2016). Corticospinal Inputs to Primate Motoneurons Innervating the Forelimb from Two Divisions of Primary Motor Cortex and Area 3a. *The Journal of Neuroscience*, 36(9):2605–2616.

Woeppel, K., Hughes, C., Herrera, A. J., Eles, J. R., Tyler-Kabara, E. C., Gaunt, R. A., Collinger, J. L., and Cui, X. T. (2021). Explant Analysis of

Utah Electrode Arrays Implanted in Human Cortex for Brain-Computer-Interfaces. *Frontiers in Bioengineering and Biotechnology*, 9.

Woolrich, M. W., Jbabdi, S., Patenaude, B., Chappell, M., Makni, S., Behrens, T., Beckmann, C., Jenkinson, M., and Smith, S. M. (2009). Bayesian analysis of neuroimaging data in FSL. *NeuroImage*, 45(1, Supplement 1):S173–S186.

Xerri, C., Zennou-Azogui, Y., Sadlaoud, K., and Sauvajon, D. (2014). Interplay between intra- and interhemispheric remodeling of neural networks as a substrate of functional recovery after stroke: Adaptive versus maladaptive reorganization. *Neuroscience*, 283:178–201.

Xiong, J., Ren, J., Luo, L., and Horowitz, M. (2018). Mapping Histological Slice Sequences to the Allen Mouse Brain Atlas Without 3D Reconstruction. *Frontiers in Neuroinformatics*, 12.

Yamauchi, T., Hori, T., and Takahashi, T. (2000). Presynaptic inhibition by muscimol through GABA $_{B}$ receptors: Presynaptic inhibition by muscimol. *European Journal of Neuroscience*, 12(9):3433–3436.

Yang, P.-F., Phipps, M. A., Jonathan, S., Newton, A. T., Byun, N., Gore, J. C., Grissom, W. A., Caskey, C. F., and Chen, L. M. (2021). Bidirectional and state-dependent modulation of brain activity by transcranial focused ultrasound in non-human primates. *Brain Stimulation*, 14(2):261–272.

Yew, K. S. and Cheng, E. M. (2015). Diagnosis of Acute Stroke. *American Family Physician*, 91(8):528–536.

Zeiler, S. R., Hubbard, R., Gibson, E. M., Zheng, T., Ng, K., O'Brien, R., and Krakauer, J. W. (2016). Paradoxical motor recovery from a first stroke after induction of a second stroke: Re-opening a post-ischemic sensitive period. *Neurorehabilitation and neural repair*, 30(8):794–800.

Zeiler, S. R. and Krakauer, J. W. (2013). The interaction between training and plasticity in the post-stroke brain. *Current opinion in neurology*, 26(6):609–616.

Zhang, T., Pan, N., Wang, Y., Liu, C., and Hu, S. (2021). Transcranial Focused Ultrasound Neuromodulation: A Review of the Excitatory and Inhibitory Effects on Brain Activity in Human and Animals. *Frontiers in Human Neuroscience*, 15.

Zhu, L. L., Lindenberg, R., Alexander, M. P., and Schlaug, G. (2010). Lesion Load of the Corticospinal Tract Predicts Motor Impairment in Chronic Stroke. *Stroke*, 41(5):910–915.

Appendix

Kinematic analysis

The calculation key for the utilized angles (Table 1) as well as the loading factors for both the BBT (Table 4) and the spherical ROP (Table 5) tasks are presented on the next pages. Further, the grasping rate for the modified Brinkman board is shown.

Kinematic feature	Computed from 3D kinematic
MCP thumb angle	$\overrightarrow{v_1}$: vector from right wrist to MCP thumb joint $\overrightarrow{v_2}$: vector between MCP and IP joints of the thumb Θ MCP_{thumb}: angle between $\overrightarrow{v_1}$ and $\overrightarrow{v_2}$
MCP index angle	$\overrightarrow{v_3}$: vector from right wrist to MCP index joint $\overrightarrow{v_4}$: vector from MCP index joint to the PIP index joint $\overrightarrow{v_{h1}}$: vector between MCP index and MCP pinkie joint $\overrightarrow{v_{n1}}$: vector normal to the plan of the $\overrightarrow{v_3}$ and $\overrightarrow{v_{h1}}$ vectors Θ MCP_{index}: angle between $\overrightarrow{v_{h1}}$ and $\overrightarrow{v_4}$
MCP pinkie angle	$\overrightarrow{v_5}$: vector from left wrist to MCP pinkie joint $\overrightarrow{v_6}$: vector from MCP pinkie joint to the PIP pinkie joint $\overrightarrow{v_{h2}}$: vector between MCP pinkie and MCP index joint $\overrightarrow{v_{n2}}$: vector normal to the plan of the $\overrightarrow{v_5}$ and $\overrightarrow{v_{h2}}$ vectors Θ MCP_{pinkie}: angle between $\overrightarrow{v_{h2}}$ and $\overrightarrow{v_6}$
Abduction index angle	$\overrightarrow{v_{h2}}$: vector between MCP pinkie and MCP index joint $\overrightarrow{v_4}$: vector from MCP index joint to the PIP index joint Θ AA_{index}: angle between $\overrightarrow{v_{h2}}$ and $\overrightarrow{v_4}$
Abduction pinkie angle	$\overrightarrow{v_{h1}}$: vector between MCP index and MCP pinkie joint $\overrightarrow{v_6}$: vector from MCP pinkie joint to the PIP pinkie joint Θ AA_{pinkie}: angle between $\overrightarrow{v_{h1}}$ and $\overrightarrow{v_6}$
Palmar abduction thumb angle	$\overrightarrow{v_{h3}}$: vector from right wrist to left wrist $\overrightarrow{v_1}$: vector from right wrist to MCP thumb joint $\overrightarrow{v_5}$: vector from left wrist to MCP pinkie joint $\overrightarrow{v_{n3}}$: vector normal to the plan of the $\overrightarrow{v_3}$ and $\overrightarrow{v_{h3}}$ vectors $\overrightarrow{v_{n4}}$: vector normal to the plan of the $\overrightarrow{v_5}$ and $\overrightarrow{v_{h3}}$ vectors Θ $AA_{planarthumb}$: angle between $\overrightarrow{v_{n3}}$ and $\overrightarrow{v_{n4}}$
Radial abduction thumb angle	$\overrightarrow{v_1}$: vector from right wrist to MCP thumb joint $\overrightarrow{v_3}$: vector from right wrist to MCP index joint $\overrightarrow{v_{h3}}$: vector from right wrist to left wrist $\overrightarrow{v_{n3}}$: vector normal to the plan of the $\overrightarrow{v_3}$ and $\overrightarrow{v_{h3}}$ vectors $\overrightarrow{v_{n31}}$: vector normal to the plan of the $\overrightarrow{v_{n3}}$ and $\overrightarrow{v_3}$ vectors $\overrightarrow{v_{n32}}$: vector normal to the plan of the $\overrightarrow{v_{n3}}$ and $\overrightarrow{v_1}$ vectors Θ $AA_{radialthumb}$: angle between $\overrightarrow{v_{n31}}$ and $\overrightarrow{v_{n32}}$
Wrist flexion angle	$\overrightarrow{v_7}$: vector from elbow to the wrist $\overrightarrow{v_{h3}}$: vector from right wrist to left wrist $\overrightarrow{v_3}$: vector from right wrist to MCP index joint $\overrightarrow{v_{n5}}$: vector normal to the plan of the $\overrightarrow{v_7}$ and $\overrightarrow{v_{h3}}$ vectors Θ $Flexion_{Wrist}$: angle between $\overrightarrow{v_{n5}}$ and $\overrightarrow{v_3}$
Wrist suppination angle	$\overrightarrow{v_8}$: vector from shoulder to the elbow $\overrightarrow{v_9}$: vector from elbow to the middle point of the wrist $\overrightarrow{v_{h3}}$: vector from right wrist to left wrist $\overrightarrow{v_{n6}}$: vector normal to the plan of the $\overrightarrow{v_8}$ and $\overrightarrow{v_9}$ vectors Θ $Suppination_{Wrist}$: angle between $\overrightarrow{v_{n6}}$ and $\overrightarrow{v_{h3}}$

Table 1: Angle calculations The list of angle calculation vectors utilized for the kinematic analysis. Continued on the next page.

Kinematic feature	Computed from 3D kinematic
Wrist deviation angle	$\overrightarrow{v_7}$: vector from elbow to the wrist $\overrightarrow{v_{h3}}$: vector from right wrist to left wrist $\overrightarrow{v_5}$: vector from left wrist to MCP pinkie joint $\overrightarrow{v_{n5}}$: vector normal to the plan of the $\overrightarrow{v_7}$ and $\overrightarrow{v_{h3}}$ vectors $\overrightarrow{v_{n51}}$: vector normal to the plan of the $\overrightarrow{v_3}$ and $\overrightarrow{v_{n5}}$ vectors $\overrightarrow{v_{n52}}$: vector normal to the plan of the $\overrightarrow{v_5}$ and $\overrightarrow{v_{n5}}$ vectors Θ $\text{Deviation}_{\text{Wrist}}$: angle between $\overrightarrow{v_{n51}}$ and $\overrightarrow{v_{h52}}$
Elbow flexion angle	$\overrightarrow{v_7}$: vector from elbow to the wrist $\overrightarrow{v_8}$: vector from shoulder to the elbow Θ $\text{Flexion}_{\text{elbow}}$: angle between $\overrightarrow{v_7}$ and $\overrightarrow{v_8}$
Abduction sholder angle	$\overrightarrow{v_8}$: vector from shoulder to the elbow $\overrightarrow{h_4}$: $\begin{pmatrix} 0 \\ 0 \\ 1 \end{pmatrix}$ Θ $\text{AA}_{\text{shoulder}}$: : angle between $\overrightarrow{v_8}$ and $\overrightarrow{v_{h4}}$
Angular velocity (for each angle)	derivative from each angle value over time
Velocity of the wrist	wrist position over time (dp/dt)
Acceleration of the wrist	derivative of the velocity (d^2p/d^2t)
Jerk of the wrist	derivative of the acceleration (d^3p/d^3t)
Wrist trajectory in x-axis direction	Euclidean distance between wrist position over time along the x-axis
Wrist trajectory in y-axis direction	Euclidean distance between wrist position over time along the y-axis
Wrist trajectory in z-axis direction	Euclidean distance between wrist position over time along the z-axis
Distance from thumb tip to index tip	Euclidean distance between the tip of the thumb and the tip of the index in 3D
Distance from thumb tip to pinkie tip	Euclidean distance between the tip of the thumb and the tip of the pinkie in 3D
Distance from right wrist to thumb tip	Euclidean distance between wrist joint and the tip of the thumb in 3D
Distance from right wrist to index tip	Euclidean distance between wrist joint and the tip of the index in 3D
Distance from left wrist to pinkie tip	Euclidean distance between wrist joint and the tip of the pinkie in 3D
Distance from shoulder to left wrist	Euclidean distance between shoulder complex and the wrist joint in 3D

Grouped features	Startic features for the Robot Task
Trial related features	Trial duration
	Reaching phase duration
	Grasp-Passing phase duration
	Grasp-Droping phase duration
	Maximum trial velocity
	Maximum reaching phase velocity
	Maximumn Grasp-Passing phase velocity
	Maximum Grasp-Droping phase velocity
	Area covered by the wrist in the xy-plane
	Area covered by the wrist in the yz-plane
	Area covered by the wrist in the xz-plane
	Mean wrist trajectory in x-axis direction
	Mean wrist trajectory in y-axis direction
	Mean wrist trajectory in z-axis direction
	Mean wrist trajectory in xyz-axis direction
Range of Motion (ROM) of the angles	ROM Wrist suppination angle during reaching phase
	ROM Wrist suppination angle during grasping phase
	ROM Elbow flexion angle during reaching phase
	ROM Elbow flexion angle during grasping phase
	ROM Abduction sholder angle during reaching phase
	ROM Abduction sholder angle during grasping phase
Mean angle value	Mean Wrist suppination angle during reaching phase
	Mean Wrist suppination angle during grasping phase
	Mean Elbow flexion angle during reaching phase
	Mean Elbow flexion angle during grasping phase
	Mean Abduction sholder angle during reaching phase
	Mean Abduction sholder angle during grasping phase

Table 2: Static feature list: BBT A list of the static features used in the kinematic analysis for the BBT.

Grouped features	Startic features for the Robot Task
Trial related features	Trial duration
	Maximum velocity during the reaching phase
	Maximum velocity during the pulling phase
	Maximum acceleration during the reaching phase
	Maximum acceleration during the pulling phase
	Maximum jerk during the reaching phase
	Maximum jerk during the pulling phase
	Area covered by the wrist in the xy-plane
	Area covered by the wrist in the xz-plane
	Area covered by the wrist in the yz-plane
Range of Motion (ROM) of the angles during the reaching phase	ROM MCP thumb angle during reaching phase
	ROM MCP index angle during reaching phase
	ROM MCP pinky angle during reaching phase
	ROM Abduction index angle during reaching phase
	ROM Abduction pinkie angle during reaching phase
	ROM Palmar abduction thumb angle during reaching phase
	ROM Radial abduction thumb angle during reaching phase
	ROM Wrist suppination angle during reaching phase
	ROM Wrist flexion angle during reaching phase
	ROM Wrist deviation angle during reaching phase
	ROM Elbow flexion angle during reaching phase
	ROM Abduction sholder angle during reaching phase
	ROM Abduction sholder angle during reaching phase
Range of Motion (ROM) of the angles during the pulling phase	ROM MCP thumb angle during pulling phase
	ROM MCP index angle during pulling phase
	ROM MCP pinky angle during pulling phase
	ROM Abduction index angle during pulling phase
	ROM Abduction pinkie angle during pulling phase
	ROM Palmar abduction thumb angle during pulling phase
	ROM Radial abduction thumb angle during pulling phase
	ROM Wrist suppination angle during pulling phase
	ROM Wrist flexion angle during pulling phase
	ROM Wrist deviation angle during pulling phase
	ROM Elbow flexion angle during pulling phase
	ROM Abduction sholder angle during pulling phase
	ROM Abduction sholder angle during pulling phase
Maximum angular velocity	Maximum angular velocity for the MCP thumb angle
	Maximum angular velocity for the MCP index angle
	Maximum angular velocity for the MCP pinky angle
	Maximum angular velocity for the abduction index angle
	Maximum angular velocity for the abduction pinkie angle
	Maximum angular velocity for the palmar abduction thumb angle
	Maximum angular velocity for the radial abduction thumb angle
	Maximum angular velocity for the wrist suppination angle
	Maximum angular velocity for the wrist flexion angle
	Maximum angular velocity for the wrist deviation angle
	Maximum angular velocity for the elbow flexion angle
	Maximum angular velocity for the abduction sholder angle
Area under the curve (AUC) for the distances between the joints	AUC of the distance from thumb tip to index tip over time
	AUC of the distance from thumb tip to pinky tip over time
	AUC of the distance from right wrist to thumb tip over time
	AUC of the distance from right wrist to index tip over time
	AUC of the distance from left wrist to pinky tip over time
	AUC of the distance from shoulder to left wrist over time
Mean distance between joints	Mean distance from thumb tip to index tip
	Mean distance from thumb tip to pinky tip
	Mean distance from right wrist to thumb tip
	Mean distance from right wrist to index tip
	Mean distance from left wrist to pinky tip
	Mean distance from shoulder to left wrist

Table 3: Static feature list: ROP A list of the static features used in the kinematic analysis for the spherical ROP.

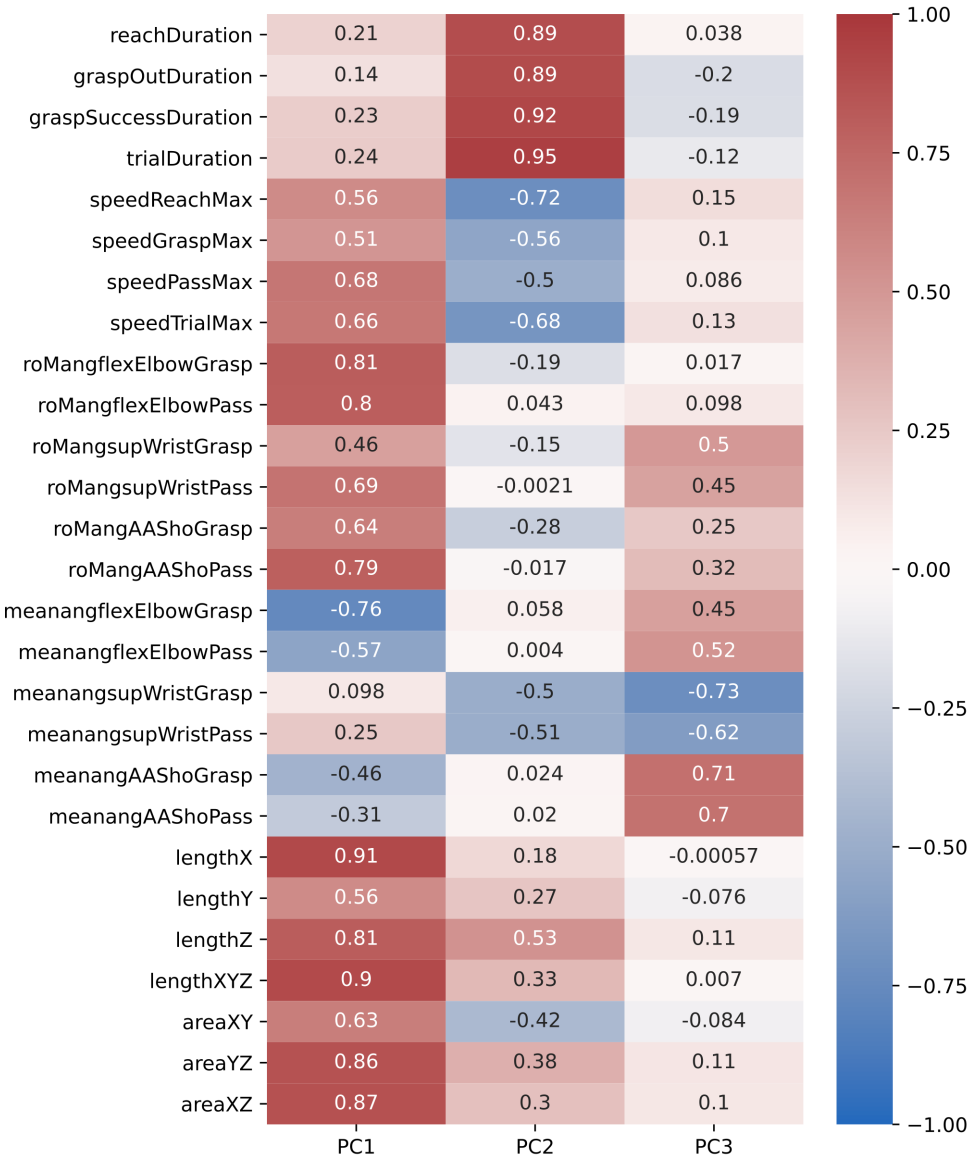

Table 4: Loading factors for principal component analysis: BBT The list of the loading factors and their individual contributions to the 1st to the 3rd principal component in the BBT analysis.

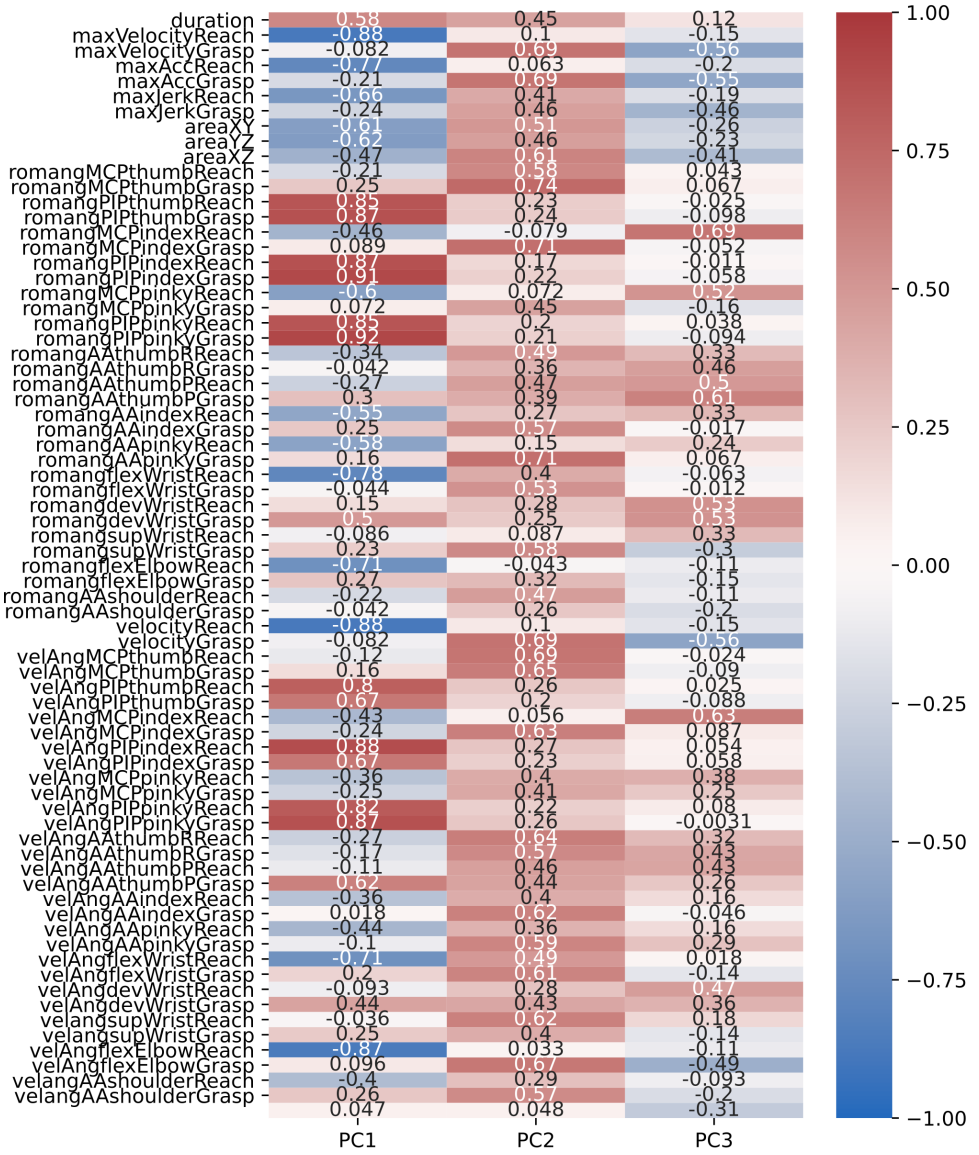

Table 5: Loading factors for principal component analysis: ROP The list of the loading factors and their individual contributions to the 1st to the 3rd principal component in the spherical ROP analysis.

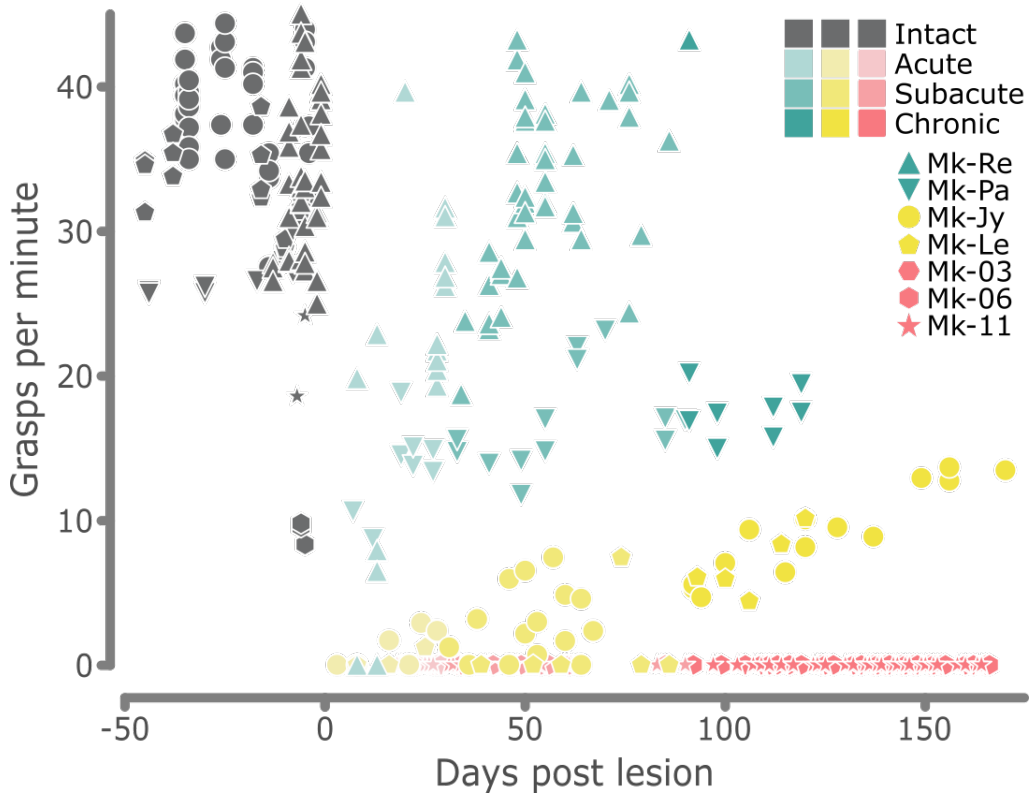

Figure 1: Grasping rate modified Brinkman Board The grasping rate in the modified Brinkman board task is shown. The intact performance is shown in gray, with acute (light), subacute (medium) and chronic (saturated) time points shown.

Surgeries

Utah array implantation

Implantation planning

Each monkey was implanted with multiple micro-electrode arrays (UTAH array, Blackrock microsystems, USA) in the motor, pre-motor, and sensory cortices. Mk-RE was implanted with five arrays, and the three other monkeys (Mk-PA, Mk-LE and Mk-JY) received six arrays each (Figure 2). The array signals were read out over an interface pedestal (Cereport, Blackrock microsystems, USA) implanted on the skull of the animal. Whereas Mk-RE and Mk-LE were implanted with two pedestals, Mk-PA and Mk-JY received only one. Depending on the pedestal technology employed, a titanium mesh (TiMesh, Medtronic, USA), in combination with a foot-plate (Buri SA, La Chaux-de-Fonds, Switzerland), was used to aid in anchoring and force distribution along the skull. The foot-plate was custom designed to fit the dimensions of the Blackrock Cereport pedestals, and form a quick and reliable link using M1.6 titanium screws (Buri SA, La Chaux-de-Fonds, Switzerland) during the surgical intervention. Individual 3D models of the brain and skull were used to plan the optimal placement of the UTAH arrays and the minimal craniotomy size needed for access. The pedestals were arranged on the remaining skull surface, ensuring optimal stability and spacing between the arrays. For pedestals requiring a titanium mesh, we shaped the mesh around the skull model. The mesh was then cut into the smallest possible shape to still able to provide stable anchoring while allowing access to the planned craniotomies. Sharp edges were sanded down to lessen tissue irritation after implantation. The mesh of Mk-RE was then coated with hydroxyapatite (Medicoat AG, Zürich, Switzerland), to promote ossointegration. Hydroxyapatite coating was avoided in subsequent animals, as the ossointegration precludes possible explantation procedures. After shaping, the mesh and foot-plates were assembled and sterilized with low temperature (55°C) vaporized H_2O_2 (PlazMax Line P50, Tuttnauer, Switzerland).

Implantation surgery

The animals were prepared for surgery and sedated as described in chapters 2.2.2 and 2.2.2.

The skin was incised in either a straight line or in a Y-shape along the mid-line, depending on whether one or two pedestals were to be implanted.

The skin was bluntly dissected and pulled aside. The connective tissue was then removed from the exposed skull. The location of the craniotomies and pedestals was drawn onto the skull according to the implantation plan (Chapter 5.3). The craniotomies were conducted and the two extracted bone flaps were stored in ringer-lactate solution until re-implantation. The assembled and sterilized mesh and base-plates were then placed on the skull and secured using self-drilling screws (1.6x3.5mm, TiMesh, Medtronic, Ireland). The pedestals and the corresponding arrays were then implanted in sequence. The pedestal was fastened to the base-plate using 8 M1.6 titanium screws (Buri SA, La Chaux-de-Fonds, Switzerland). The dura mater of the hemispheres to be implanted was incised and folded back onto the skull, where it was kept moisturized using saline solution. The Utah arrays were then correctly positioned and inserted using a pneumatic inserter system (Blackrock Microsystems, USA). The wires were further sutured to the dura mater adjacent to the implantation site. After all Utah arrays were successfully implanted, the dura mater was put back in place and sutured. The craniotomies were closed using their respective bone-flap fastened in place with 4x1 titanium mesh pieces (TiMesh, Medtronic, Ireland) and self-drilling screws (1.6x3.5mm,TiMesh, Medtronic, Ireland). Gaps between the bone were filled using artificial extracellular matrix (Spongostan™, Johnson&Johnson Medical, Belgium). The skin was then sutured and antiseptically treated.

Post-operative care was administered as described in chapter 2.2.2.

EMG implantation

For EMG recordings we used the fully implantable Grapevine EMG system (Ripple Neuro, USA). To account for the decreased body size of our subjects, we used custom wiring (38 AWG Cooner wires, Omnetics Corporation, USA) to connect to the implantable EMG signal transceiver (16 channels, 24-bit, 7.5kHz). The signal transceiver was then sealed using silicone (Dowsil, 734 flowable sealant), minimizing the risk of infection and signal deterioration. The 32 wires were then paired up and sorted into the corresponding channels and labeled according to the muscles to be implanted.

The animals were prepared for surgery and sedated as described in chapters 2.2.2 and 2.2.2. In addition to the customary head shaving, the animals' upper torsos and arms were shaved as well.

Incisions were made above the abdomen, lateral to the side of the implanta-

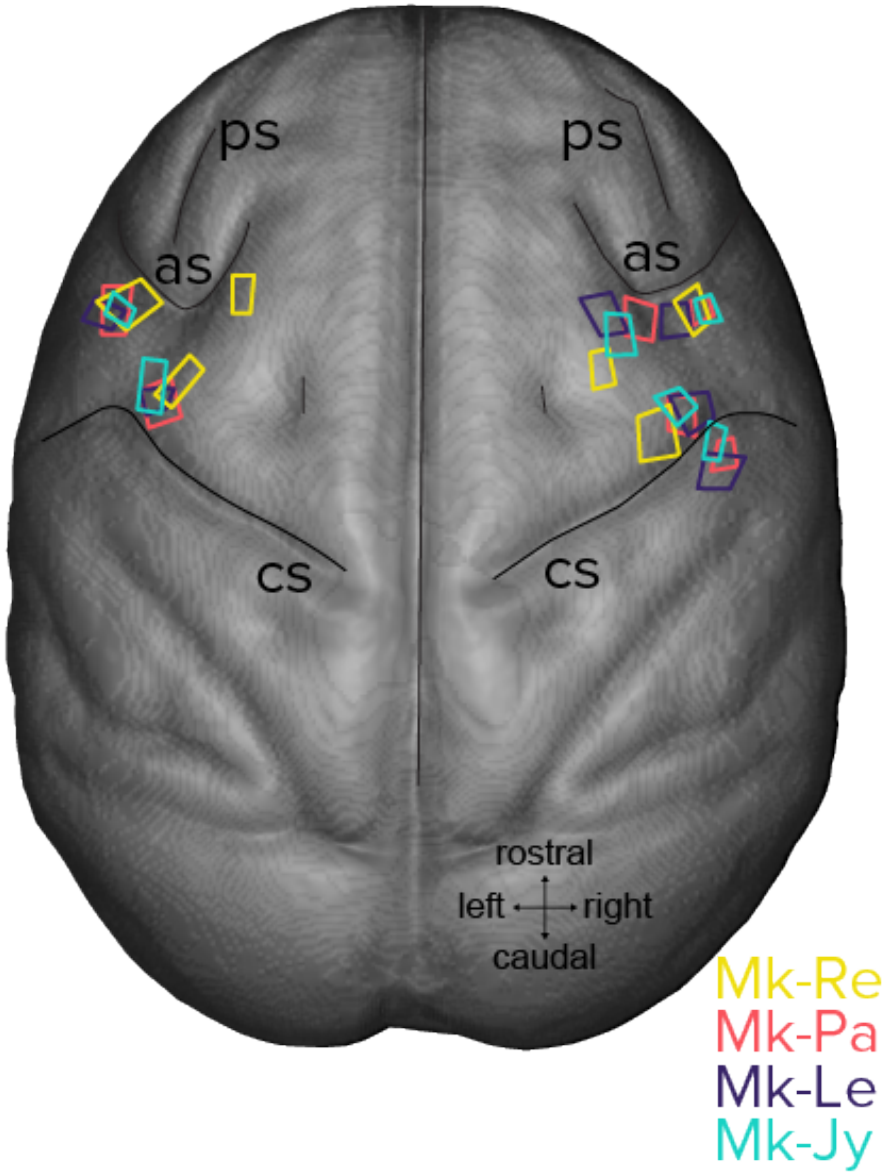

Figure 2: Utah array implantation sites Schematic depiction of the Utah array implantation sites in Mks Re, Pa, Le, and Jy. The approximate implantation sites are indicated by the colored outlines.

tion. Secondary incisions were placed above the left shoulder blade, above the deltoid, in the middle of the upper arm, as well as on the medial and distal side of the lower arm. Sub-dermal channels were laid, connecting the incisions. The signal transceiver was then placed onto the abdomen and sutured into place, before the EMG-wires were tunneled through the sub-dermal channels up to the shoulder blade incision. The skin above the signal transceiver was then cleaned and sutured. According to the implantation plan, wires were then pulled to their implantation site (Table 6). The correct muscles and optimal EMG placement therein were determined by electronically evoked muscle potentials. Where needed, the muscles were exposed by blunt dissection. We used bent 23G syringe tips for channeling and wire insertion. Before insertion, the wires were locally stripped using a scalpel blade. The wires were then inserted, and the needles retracted. To keep the wires secured, a suture-knot or a surgical staple was placed. The surrounding tissue was then antiseptically treated with Betadine solution (Mundipharma, Switzerland) before suturing.

Post-operative care was administered as described in chapter 2.2.2.

Muscle	Mk-LE	Mk-PA
Flexor digitorum superficialis	x	x
Flexor digitorum profundus	x	
Flexor caripi ulnaris	x	x
Flexor carpi radialis	x	x
Abductor policis longus	x	
Extensor digitorum comunis	x	x
Extensor carpi ulnar	x	x
Extensor carpi radialis	x	x
Palmaris longus		x
Biceps	x	x
Triceps	x	x
Deltoid	x	

Table 6: List of EMG implanted muscles The list of implanted muscles in Mk-Pa and Mk-Le